The COMET-L1 Experiment on Long-Term MCCI and Late Melt Surface Flooding

**G. Doubleva, H. Alsmeyer, T. Cron,
B. Fluhrer, J. Foit, G. Messemer,
A. Miassoedov, S. Schmidt-Stiefel,
T. Wenz, I. Ivanov, M. Cranga**

**Institut für Kern- und Energietechnik
Programm Nukleare Sicherheitsforschung**

Juni 2006

The COMET-L1 Experiment on Long-Term MCCI and Late Melt Surface Flooding

G. Doubleva[1], H. Alsmeyer, T. Cron, B. Fluhrer, J. Foit,

G. Messemer, A. Miassoedov, S. Schmidt-Stiefel, T. Wenz,

I. Ivanov[2], M. Cranga[3]

Institut für Kern- und Energietechnik

Programm Nukleare Sicherheitsforschung

[1]FH Offenburg, Germany

[2]Technical University of Sofia, Bulgaria

[3]Institut de Protection et de Sûreté Nucléaire, France

ABSTRACT

The experiment COMET-L1 investigates the situation of basement attack by a simulated corium melt. Sponsored by the European Commission as part of the LACOMERA programme, this experiment brings together partners from Germany, Bulgaria, and France. The open questions which are addressed in the actual experiment are (1) the long-term erosion of a cylindrical concrete cavity during the absence of water, and (2) the consequence of top flooding when water is added to the surface of the hot melt.

The experiment is performed in a cavity of siliceous concrete, initial inner diameter 60 cm. The mass of the steel melt is 460 kg, overlaid by 470 kg oxide melt, resulting in a total melt height of 780 mm. Decay heat was simulated by induction heating of the steel phase with a typical power of 150 kW, representing accident conditions in the late ex-vessel phase. Erosion of the concrete, temperatures of the melt, and rates and composition of the released gases are measured. Unfortunately, decay heating ended after 960 s only because of an electrical failure. In the first phase of the interaction, initial overheat of the melt is quickly reduced, while erosion rates into the axial and lateral directions are similar. When stationary conditions are achieved, periods of slow erosion and slow gas release are interrupted by phases of more intense eruptions, during which crusts are re-melted. In this phase, the axial erosion seems more pronounced, which to some extent may be due to partial solidification of the metal melt. After end of heating, the melt cools down only very slowly. Crust growth at the upper surface and related temperatures are reported. Late surface flooding has minor effect to improve heat removal.

Details of the experiment are reported to be used for validation of models and computer codes for safety assessment.

ZUSAMMENFASSUNG

Das COMET-L1 Experiment zur Langzeiterosion von Beton mit einer späten Flutung der Schmelzeoberfläche

Das Experiment COMET-L1 untersucht die Vorgänge beim Angriff des Betonfundaments durch eine simulierte Kernschmelze. Dieses Experiment, gefördert von der Europäischen Union als Bestandteil des LACOMERA Programms, bringt Partner aus Deutschland, Bulgarien und Frankreich zusammen. Die wesentlichen offenen Fragen, die in diesem Experiment untersucht werden, sind 1. die langzeitige Erosion einer zylindrischen Betonkaverne ohne Anwesenheit von Wasser und 2. die Auswirkungen der Kühlung von oben durch Flutung der heißen Schmelzen-Oberfläche mit Wasser.

Das Experiment wird in einer Kaverne mit einem Anfangsdurchmesser von 60 cm durchgeführt, gefertigt aus Beton mit silikatischen Zuschlägen. Die Schmelze besteht aus 460 kg Stahl, überschichtet von 470 kg Oxidschmelze, mit einer Gesamthöhe von 780 mm. Die nukleare Nachwärme wird durch induktive Beheizung der Stahlphase simuliert, mit einer typischen Leistung von 150 kW. Dies stellt die Unfallbedingungen in der späten Phase der Fundamenterosion dar. Es werden die Erosion des Betons, die Temperaturen der Schmelze und die Menge und Zusammensetzung der freigesetzten Gase gemessen. Leider wurde jedoch die elektrische Beheizung der Schmelze durch den Ausfall der elektrischen Leistungsteuerung nach nur 960 s beendet. In der ersten Phase der Wechselwirkung mit dem Beton beobachtet man eine schnelle Abnahme der Temperatur der Schmelze, bei etwa gleichen Erosionsraten nach unten und zur Seite. Nach Erreichen von nahezu stationären Bedingungen beobachtet man Perioden langsamer Erosion und schwacher Gasfreisetzung, die durch Phasen heftiger Eruptionen unterbrochen werden, während derer die Krusten aufgeschmolzen werden. Unter diesen Bedingungen scheint die Erosion nach unten vorzuherrschen, was zu einem gewissen Ausmaß durch die teilweise Erstarrung der Metallschmelze verursacht sein kann. Nach Ende der Beheizung kühlt die Schmelze nur sehr langsam ab. Die Krustenbildung an der Oberfläche der Schmelze und die damit verbundenen Temperaturen werden angegeben. Die Flutung der Oberfläche der Schmelze zu einem späten Zeitpunkt verbessert den Wärmeentzug aus der Schmelze nur wenig.

Die Einzelheiten des Experiments werden berichtet. Sie können verwendet werden, um Modelle und Rechenprogramme zur Sicherheitsanalyse von Reaktoren zu validieren.

TABLE OF CONTENTS

LIST OF TABLES

LIST OF FIGURES

1 Introduction

1.1 COMET as Element of the LACOMERA Project

The LACOMERA project at the Forschungszentrum Karlsruhe, Germany is a 4 year action within the 5th Framework Programme of the EU which started in September 2002 [1]. Overall objective of the project is to offer research institutions from the EU member countries and associated states access to four large scale experimental facilities QUENCH, LIVE, DISCO, and COMET which can be used to investigate core melt scenarios from the beginning of core degradation to melt formation and relocation in the vessel, possible melt dispersion to the reactor cavity, and finally corium concrete interaction and corium coolability in the reactor cavity. In all experiments, simulant material is used to investigate the behaviour of the core material. These simulant materials were especially chosen to be as close to the real core material for the important properties as possible. On the other hand, the use of the simulant material allows covering a wide and broad range of scenarios with the experiments in a relatively small time schedule and for relatively low budget/funding. The experiments, as well as necessary post test investigations and special effect tests can be performed under well defined conditions and can be completely controlled.

The main thrust of this project is towards large scale tests under prototypical conditions. These help in the understanding of core degradation and quenching, melt formation and relocation as well as melt coolability in real reactors in two ways – firstly directly by scaling-up and secondly indirectly by providing data and models for the improvement and validation of computer codes. Although the facilities can only perform experiments with simulant materials, the tests can be considered as prototypic since the selected materials represent in important physical properties the real core materials. The large masses used allow extrapolation to the reactor case. Moreover, the flexibility and variability of the facilities is high due to the rather simple handling. Pre-tests, parallel separate-effects tests and post-test analysis can be performed in one hand. These tests can be seen as complementary to tests with UO_2 in other research centres.

Within the LACOMERA project, the COMET facility is being used to study ex-vessel accident phenomena with special attention towards corium-concrete interaction and the role of cooling processes. The first experiment under this sponsorship COMET-L1, which is described in this report, investigates the long-term situation of basement attack by the simulated corium melt and brings together partners from IRSN, France, Technical University of Sofia, Bulgaria, and Forschungszentrum Karlsruhe, Germany. The open questions which are addressed in this

experiment are (1) the long-term erosion of the concrete by a two component metal plus oxide melt during the absence of water, and (2) the consequence of top flooding when water is added to the surface of the hot melt during concrete erosion. This experiment is complementary to the present OECD-CCI tests that are carried out at ANL with pure oxidic corium [2], and to the large scale, transient ECOKATS-2 experiment [3].

1.2 Background and objectives of COMET-L1

The containment integrity is the last barrier against the release of radionuclides into the environment. For this reason the containment should withstand the challenges of severe accidents followed by reactor pressure vessel melt-through. The main focus is on basemat penetration and the possibilities to prevent strong basemat erosion.

The molten core concrete interaction (MCCI) occurs when in the absence of water a direct contact of the melt and concrete happens. The importance of the MCCI on the reactor safety has led to series of experiments realised at the Forschungszentrum Karlsruhe.

The present report describes one of these experiments. The COMET-L1 experiment is a part of the large scale experiments on core degradation, melt retention, and coolability (LACOMERA) project, which is funded by the 5th Framework Programme of the European Union, and was planned to fulfil the proposals of University of Sofia [4], Bulgaria, and IRSN, France [5]. The experiment is designed as a long term MCCI test with simulated oxidic and metallic corium in a cylindrical cavity of siliceous concrete, and is performed under dry conditions in the first phase of the test, with decay heat simulation of low power. The report provides test results during downward and lateral concrete erosion during the dry phase of the experiment. After substantial concrete erosion, melt cooling is initiated by supplying water to the top of the melt. The influence of the top flooding on melt cooling and ongoing cavity erosion after the flooding is the second objective of the experiment. This second test objective is complementary to the bottom flooding concept that has been investigated in the EU sponsored ECOSTAR Programme [6].

The test uses a heated steel melt that is covered by an oxide melt. Decay heat is simulated in the steel melt by electrical inductive heating during the course of the test.

The report gives a description of the COMET facility and the operating systems as well as a presentation and analysis of the test results. The experiment was conducted on July 10th, 2004. A short overview of the main test parameters is provided in Table 1.

Table 1: Specifications for COMET-L1

Parameter	Specification
Corium simulant	Metal (Fe + Ni) and oxide (Al_2O_3 + CaO)
Melt formation	Thermite reaction
Initial temperature of the melt	1750 to 1800°C
Initial melt mass	459 kg metal + 153 kg oxide
Radial erosion limit	250 mm
Axial erosion limit	250 mm
Concrete type	Standard siliceous concrete
Initial cavity dimension	D_i = 600 mm, H_i = 710 mm
Simulated decay heat	Induction heating at approx. 130 kW
Facility pressure	Atmospheric
Cover gas	Argon
Flow rate of the cover gas	50 m^3/h main flow and 2 x 8 m^3/h from windows
Criteria for onset of top water flooding	14 cm downward erosion during the dry phase
Inlet water flow rate for top flooding	0.375 l/s
Criteria for test termination	1) Contact of the melt with a light guide 2) 25 cm radial erosion 3) Porous concrete at the bottom reached

2 COMET L1 test design

2.1 Facility description

The COMET test facility consists of a test rig with the concrete crucible, an external melt generator, induction heating system with power supply and power control, off-gas system, water supply, a series of measurement and video systems, and the data acquisition systems. An overview picture of the facility is shown in Figure 1, and the schematic illustration with the main elements of the COMET test rig is shown in Figure 2. The COMET facility and the supporting systems are located in a dedicated building. Due to safety reasons the control room with the equipment for online measurements are in a bunker next to this building.

The outer crucible consists of a composite protection tube that includes the large test insert, and is designed to withstand higher pressure pulses if they would occur. The test rig is located on a transport car to allow installation and disassembly of the facility.

The simulated corium melt is generated externally by a thermite reaction (see chapter 2.2) with an initial temperature of about 1800°C and poured into the crucible through a lid in the upper hood. This moment defines the experimental time zero, when the first phase of dry erosion starts. The dry phase ends when 14 cm axial erosion is reached and top flooding is initiated. During the course of the test, continuous heating takes place through the induction coil that is located under the bottom concrete shell.

The outer crucible is gas tight so that all gases, that are generated during the experiment, are collected in the free volume of the crucible and feed through the off-gas system into the ambient atmosphere. A constant argon cover gas flow is injected into the crucible to prevent the accumulation of a burnable gas mixture. In the off-gas system, the main characteristics such as temperature, composition and flow rate of the released gases are measured online.

The induction coil, which supplies the electromagnetic 1000 cps heating power to the melt, is water-cooled. All other components located on the transport car are fabricated from non-metallic materials to exclude coupling to the induction field. The upper surface of the induction coil is covered by a 5 mm silicone foil, which protects the coil against any water that might be released from the concrete cavity. A 10 mm thin, refractory plate protects the induction coil, if hot melt would penetrate the concrete crucible. The distance between the induction coil and concrete crucible or melt respectively is defined in the plan of the COMET-L1 test [7] and is kept as small as possible to reduce the inductive losses.

The crucible is fabricated from standard siliceous concrete. The composition of the concrete in weight percentages is as follows: SiO_2 70.3%, $Ca(OH)_2$ 13.55%, Al_2O_3 6.58%, $CaCO_3$ 5.46%, free H_2O 4.11%. The cement is of the type blast furnace cement CEM III/B 32,5 NW/HS.

The cylindrical ring of MgO oxide, located above the crucible, is 90 mm thick and has an inner diameter of 920 mm. The ring is stable enough so that the melt may attack only the structures below it. The gap between the ring and the protection tube is filled with coarse silica gravels used as a thermal insulation.

Figure 1: COMET facility

crucible hood with
off-gas line

tie rod

⌀ 1143

MgO - liner

composite
protection tube

⌀ 920

⌀ 1100

porous insulation

⌀ 600

concrete crucible

coolant water
on demand

instrumentation
port

sealing foil

porous concrete

protect plate

induction coil

transport car
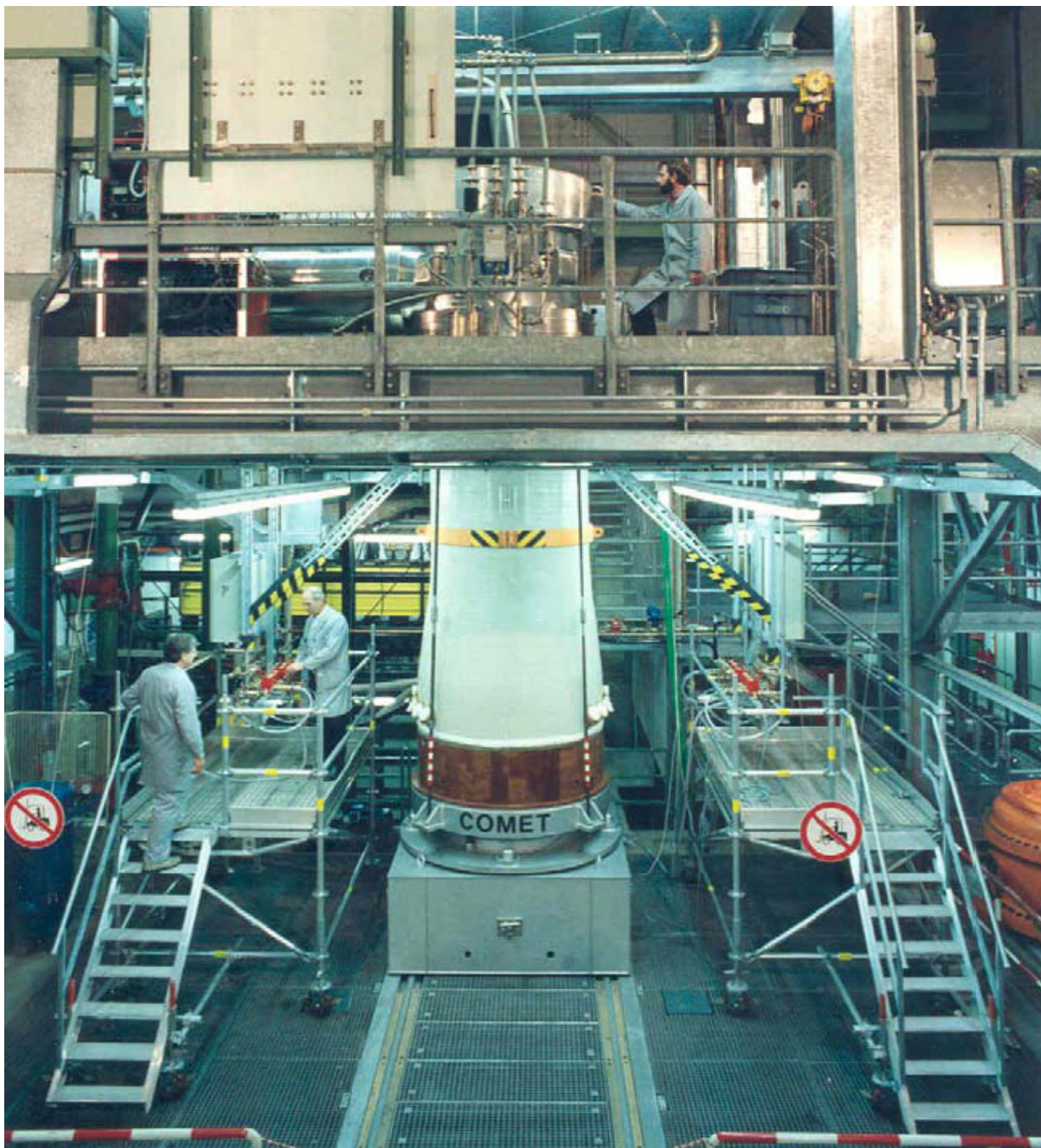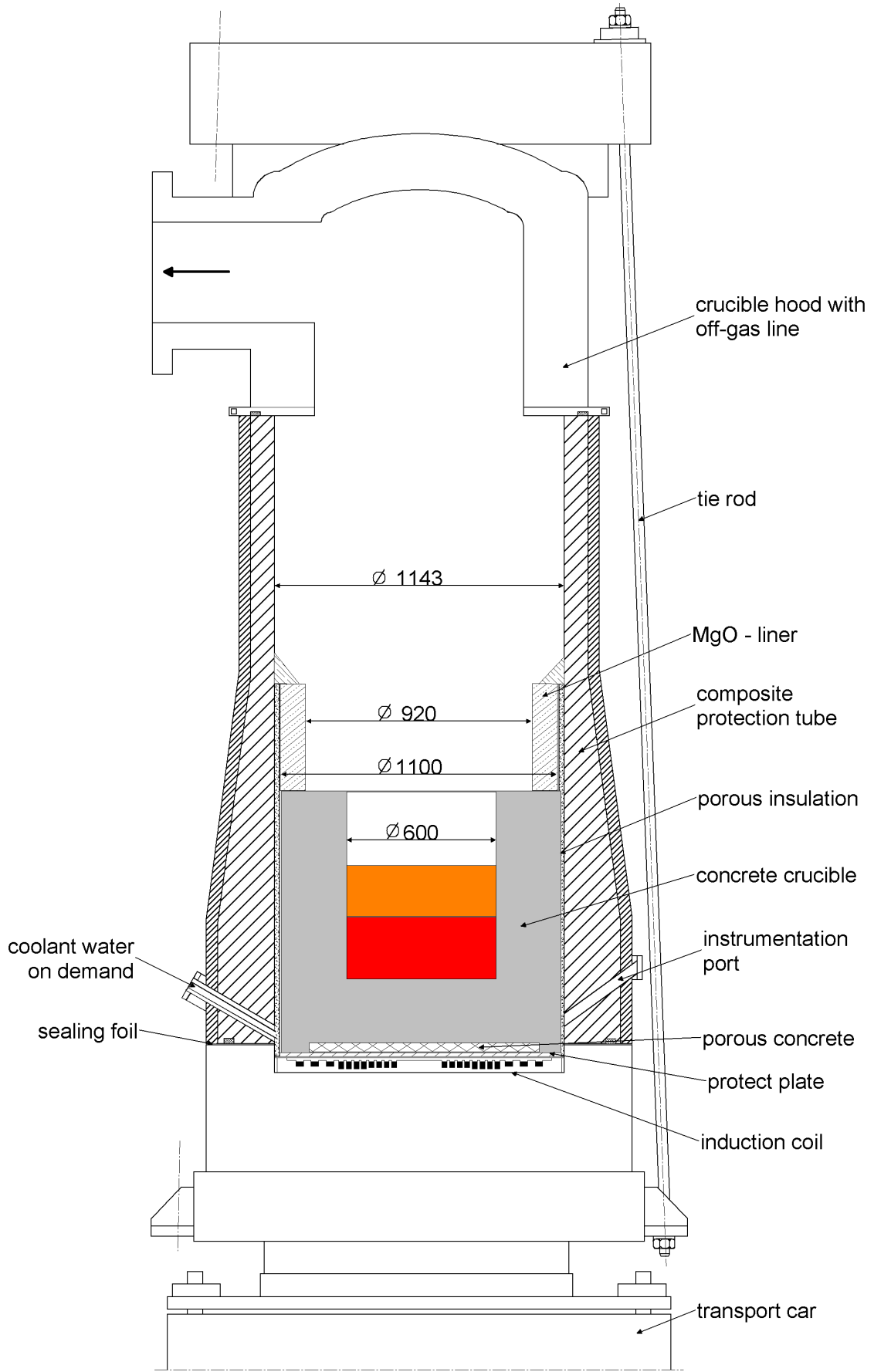
Figure 2: COMET test rig with its element

The inner structure of the composite protection tube is formed by refractory concrete and the outer shell of gas-tight, high temperature epoxy with glass fiber. The upper hood is a steel structure with inner ceramic liner and is connected to the off-gas tube. The role of the four tie rods is to tighten the upper and lower parts of the facility and maintain its integrity in case when inner mechanical loads act on the structure.

Two redundant water supply lines are connected to the porous concrete layer under the bottom of the crucible, to which water may be supplied on demand (Figure 3). This layer shall act as an efficient heat sink when late in the test the melt has propagated to the lower bottom of the inner concrete crucible, and the residual heat from concrete and melt must be removed to maintain the integrity of the induction heating system. Two instrumentation ports to the lower concrete cavity are used for thermocouple and light guides instrumentation of the crucible.

The dimensions of the crucible of COMET-L1, providing detailed geometry information to Figure 2, are presented in Figure 3. The crucible of the facility is made of standard siliceous concrete and has an inner diameter of 600 mm. The outer diameter is 1100 mm which is limited by the facility size. The height of the crucible is 1000 mm. The initial height of the metal and oxide phases together is 450 mm, without taking into account the porosity of the melt by gas release. The thickness of the concrete at the bottom and sidewalls is 250 mm each.
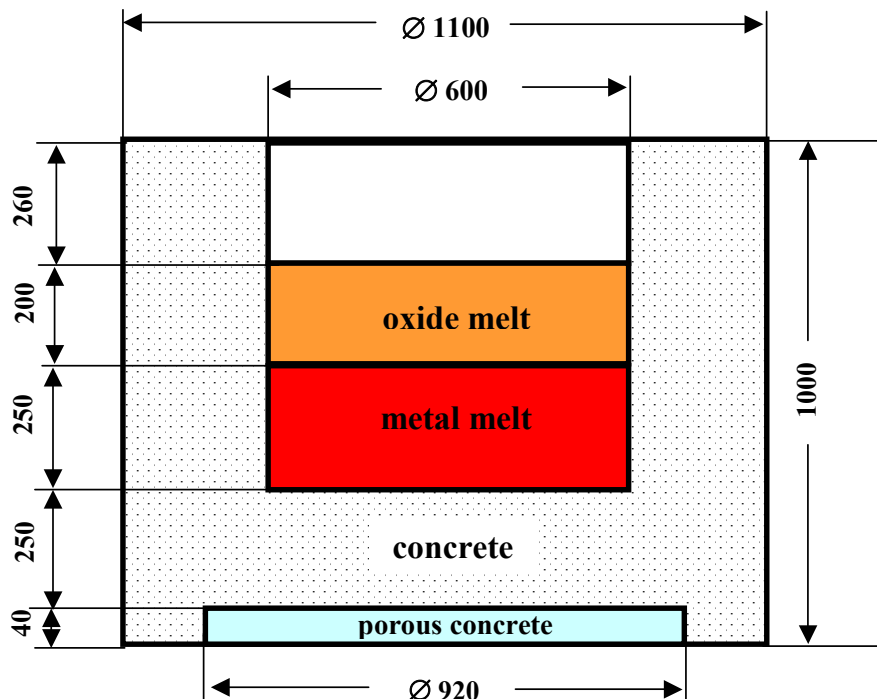
Figure 3: Dimensions of COMET-L1 crucible

2.2 Melt generation and melt composition

The simulated corium melt is generated by a thermite reaction in a separate reaction vessel located above the test facility [8]. The basis for this reaction is a thermite powder that provides liquid Al_2O_3 and iron by strongly exothermic reaction.

$$Al + Fe_2O_3 \rightarrow Al_2O_3 + Fe + h_{chem} \qquad (1)$$

To reduce the freezing temperature of the oxide melt about 30 % of burned lime CaO is added to the thermite powder. The resulting oxide is then a mixture of two oxide components (Al_2O_3 and CaO). In addition, nickel pellets are added to the thermite mix to produce a two component (Fe/Ni) metal melt. The nickel fraction has influence on the inductive coupling of the metal melt to the induction coil: For temperatures below the Curie temperature (774°C), pure iron would change from paramagnetic to ferromagnetic behaviour resulting in non-homogeneous heating due to concentration of the inductive heating mostly in the ferromagnetic portions of the iron. The addition of the nickel reduces the transition to ferromagnetism to < 400°C and thus allows more homogeneous induction heating of the solidifying metal melt.

The thermite powder for the experiment is composed of two types of commercial powders, namely R 70 HC and Al SSH. Furthermore, steel in form of nails and the nickel pellets are added, which supply 40 % of the total metal melt. The composition of the thermite powder and the resulting melt composition are presented in Table 2.

Table 2: Composition of the thermite powder and the resulting melts

Constituent	kg
Initial composition:	
Thermite powder R 70 HC	108.67
Thermite powder Al SSH	451.56
Nickel	45.59
Nails (Fe)	134.59
CaO	218.76
Total	959.53
Generated melt:	
Metal 90 % Fe + 10% Ni	459
Oxide to crucible 56 % Al_2O_3 + 44 % CaO	467 (153 planned)
Oxide to slag container	23 (347 planned)
Total	959

The thermite powder is preheated to about 200°C by electrical heater rods in the thermite reaction vessel before the ignition of the thermite so that the high masses of cold, solid nickel, nails and burned lime can be compensated. The resulting temperature of the melt after the thermite reaction is approx. 1800°C. The time between the ignition and pour is planned to be 90 seconds.

All metal melt and part of the oxide melt are poured through a lid in the hood of the test facility. The process is controlled by an online weighting system. The residual oxide melt is poured into a slag container.

The planned height of the metal melt in the crucible without void fraction is 250 mm. The height of the oxide melt was planned to be 200 mm. However, due to a disturbance of the weighting system during pour of the melt, a total of 467 kg oxide was delivered to the crucible, leading to an increased initial oxide height of 540 mm, which is slightly above the upper edge of the inner concrete crucible.

The calculated densities of the melt are 6500 kg/m^3 for the metal phase and 2700 kg/m^3 for the oxide [7]. The oxide is a mixture of 56 w-% Al_2O_3 and 44 w-% CaO, with a freezing range from 1500 to 1385°C. This oxide mixture simulates the oxidic fraction of the corium melt in a LWR, but at lower temperatures. The silica from the decomposing concrete will change the oxide properties during the course of the experiment, following the same tendency as would occur in the reactor case. - For the steel melt, 10 w-% Ni are added to the Fe melt, resulting in 460 kg Fe+Ni melt. Ni lowers the solidification range and represents components of the stainless steel of core structures. No further metals were added as they would no more exist in metallic form at that time of the accident for which this long-term MCCI experiment is representative (e.g. no Zr or Cr).

2.3   Decay heat simulation

The simulation of the decay heat in the melt is achieved by induction heating which couples to the metallic fraction of the melt. The horizontal induction coil, located under the crucible, forms the resonance circuit together with a set of 27 high voltage capacitors driven by a 1 kHz power supply. The maximum inductor voltage is 2600 V; the maximum current is 12000 A. The equivalent rated upper heating power for a non-magnetic melt is 400 kW. The heating power deposited in the melt is determined online by the actual measured total power from which the losses by ohmic resistance and by the electromagnetic stray field are subtracted. These

losses were determined in separate system tests, depending on voltage and currents of the induction circuit. In addition, a complete balance of all electric cooling circuits confirms the validity of this approach.

During the experiment, the inductive power is adjusted by control of the inductor voltage. This is performed manually by the operator, based on the displayed actual power history.

The net heating power may vary strongly with the coupling efficiency between induction coil and metal melt. All relevant data of induction heating are monitored for detailed evaluation. There are three processes influencing the electromagnetic coupling:

- Agitation and variation of the void in the melt: for higher void the efficiency of the coupling is reduced. Strong high frequency power oscillations are characteristic for the early MCCI processes. Solidification of the melt, in whatever structure, leads to more stable coupling.
- The reduced distance between melt and induction coil, which is a consequence of the concrete erosion, improves the coupling.
- The electrical properties of the metal melt change with temperature. The most important property for the actual melt is the magnetic permeability which increases strongly below Curie temperature (400°C). This will occur after solidification of the melt and further cooling of the melt, resulting in a higher efficiency of heating.

In the present test, the induction heating system was started already 2.5 minutes before melt pouring. It was planned to reach ~200 kW of the heating power and to keep it almost constant until the end of the experiment [7].

2.4 Water supply and off-gas systems

The water for the supply system, to be activated late in the test, is provided from a water tank, located 2 m above the inner bottom surface of the crucible. The water level in the tank is kept constant by automatic level control and refill of fresh water from the building supply system. The temperature of the water is 20 C. The water system is controlled by the operator and the flow of the water can be modified.

The off-gas system is connected to the crucible through the hood. The system consists of a horizontal 1 m long tube with a ceramic liner of 400 mm inner diameter, a vessel to retain any

melt which could be ejected from the test vessel, and a 11 m long horizontal steel tube with 500 mm inner diameter, exhausting the gas flow to the atmosphere outside of the building.

The large volume of the off-gas system excludes pressure build-up in the test vessel even for high gas rates. The off-gas system is preheated to 110°C before and during the experiment to exclude condensation of the steam. The end of the off-gas tube is closed in the beginning by a paper diaphragm, which allows argon inertisation before starting the test. This diaphragm is expelled by the first hot gases produced during pouring of the melt. Off-gas analyses are performed by instrumentation located along the off-gas tube, including a mass spectrometer for chemical analysis.

At the end of the off-gas tube, a heater plug ignites the off-gas if the concentration of the burnable gases is sufficient. A standing flame usually characterizes the first phase of dry concrete erosion when high amount of hydrogen is released [7].

2.5   Instrumentation and data acquisition

The COMET facility is equipped with a multitude of instrumentation to monitor and control the experiment and to collect data for subsequent evaluation. All data are stored and displayed on a PC data acquisition system as well as online registration on chart recorders and printers. Moreover, several video systems are used to observe the experiment, including two video installations, which are directed from the crucible hood onto the surface of the melt. These systems are especially useful to observe all processes, which are related to crust formation on the melt surface and during cooling. An infrared (IR) video camera was installed on top of the hood of the crucible, viewing through a sapphire window on the surface of the melt. This camera operates in the IR wavelength range from 3.4 to 5.0 μm and produces a video film and, every 15 s, up to 240 high quality digital pictures during 60 min. This allows determination of localized temperatures of the surface of the melt or of the upper crust throughout the experiment. As for any IR system, to derive the temperature or the emitted radiation from the surface, assumptions have to be made for the emissivity of the surface.

The measurements signals are collected to characterise the information written below:

- Electrical induction heating: Total power, net power, various voltages and currents, inductor frequency, control temperatures and coolant flows.

- Generation and pouring of the thermite melt: mass of the melt in the thermite reaction vessel, temperature of the melt during pouring, signals to control the pouring process.

- Coolant flow to the crucible: water flow rate, water pressure, height of water level during flooding.

- Upper crucible hood: temperature and pressure in the gas room, control and rate of the argon cover gas flow.

- Off-gas system: gas flow, temperature and pressure; gas composition by on-line quadrupole mass spectrometry.

- Control signals and conditions of the experimental hall.

- COMET crucible [9]: temperature and erosion profile of the concrete, temperature in the structures nearby. They are measured with the help of the thermocouples positioned at different levels in the crucible. The total number of thermocouples located in the crucible is 92. 88 thermocouples of type K (NiCr/Ni) are positioned in the two perpendicular planes separating the cylindrical crucible into four sections. Four W/Re thermocouples are embedded in the sidewalls of the crucible. The positions of the thermocouples are provided in Figure 4 and Figure 5.

The thermocouples Type K, which are embedded in the concrete crucible, fail at ~ 1350°C by melting of the concrete or, at lower temperatures, by thermo-chemical attack of the decomposing concrete. Their failure in most cases indicates arrival of the melt front, and thus provide information about the actual position of the melt. These thermocouples are, however, unable to measure the temperature of the melt because of the chemically aggressive melt.

To measure the temperature of the melts at the beginning of the test and further on, four W/Re thermocouples are embedded in the sidewalls of the crucible, protruding into the oxide and metal layers. Due to the chemically aggressive melts, any type of thermocouple will be destroyed during the test. For this reason the measurements with these thermocouples can give reliable data only in the first period of the experiment.

The instrumentation is arranged in two perpendicular planes, namely SW-NE (Figure 4) and SE –NW (Figure 5), the latter with a reduced number of 32 thermocouples. The number of the thermocouples is limited by the available high quality differential amplifiers which are required.
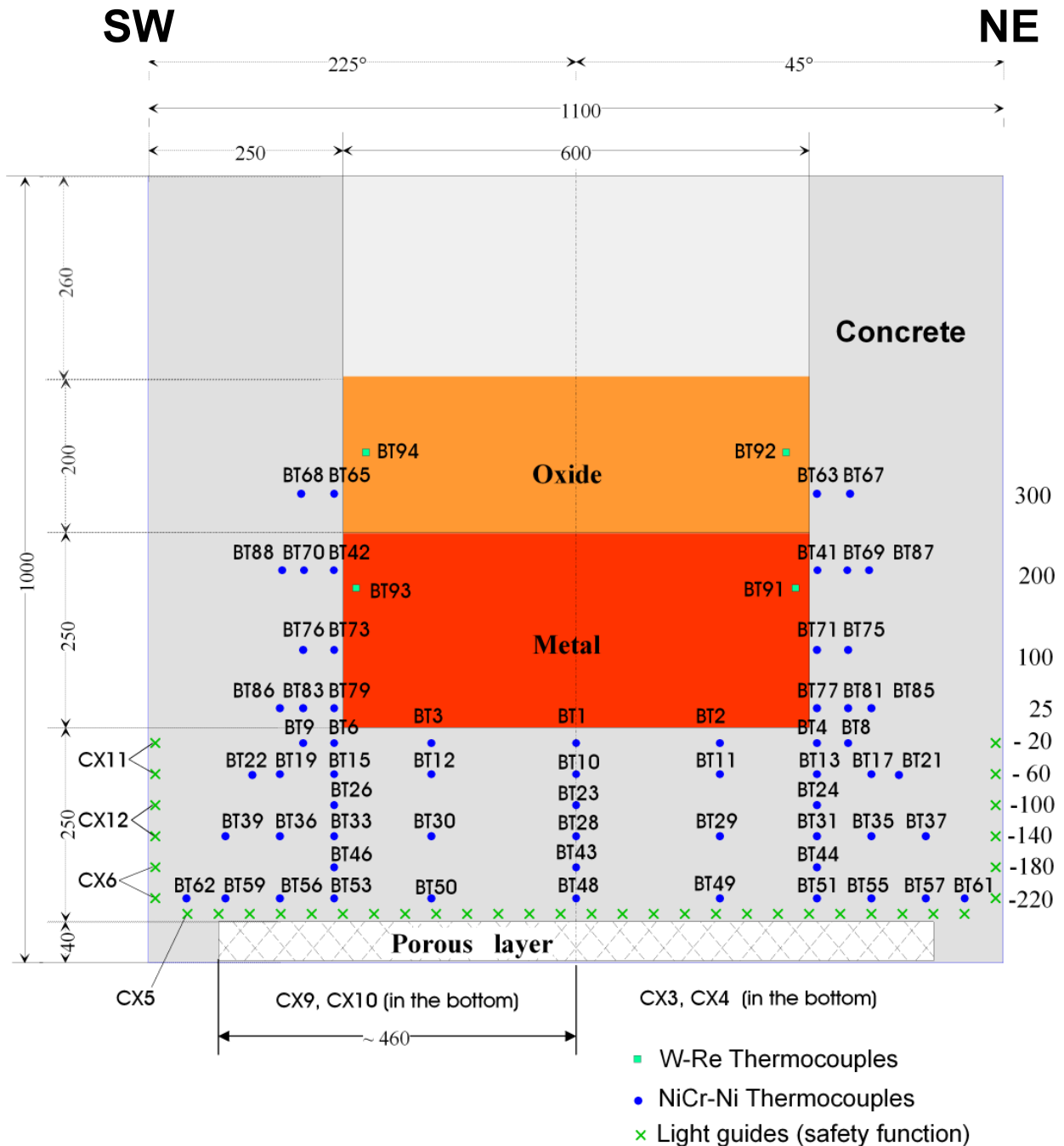
Figure 4: Positions of the thermocouples in the SW - NE plane

The positions of the thermocouples are symmetric to the rotation axis in each horizontal plane. Close to the bottom of the concrete the thermocouples are more densely positioned for better observation of the erosion process. The four W/Re thermocouples are situated in separate planes embedded in the sidewalls of the crucible and should give information about the temperatures of the metal and oxide melt before they failed.
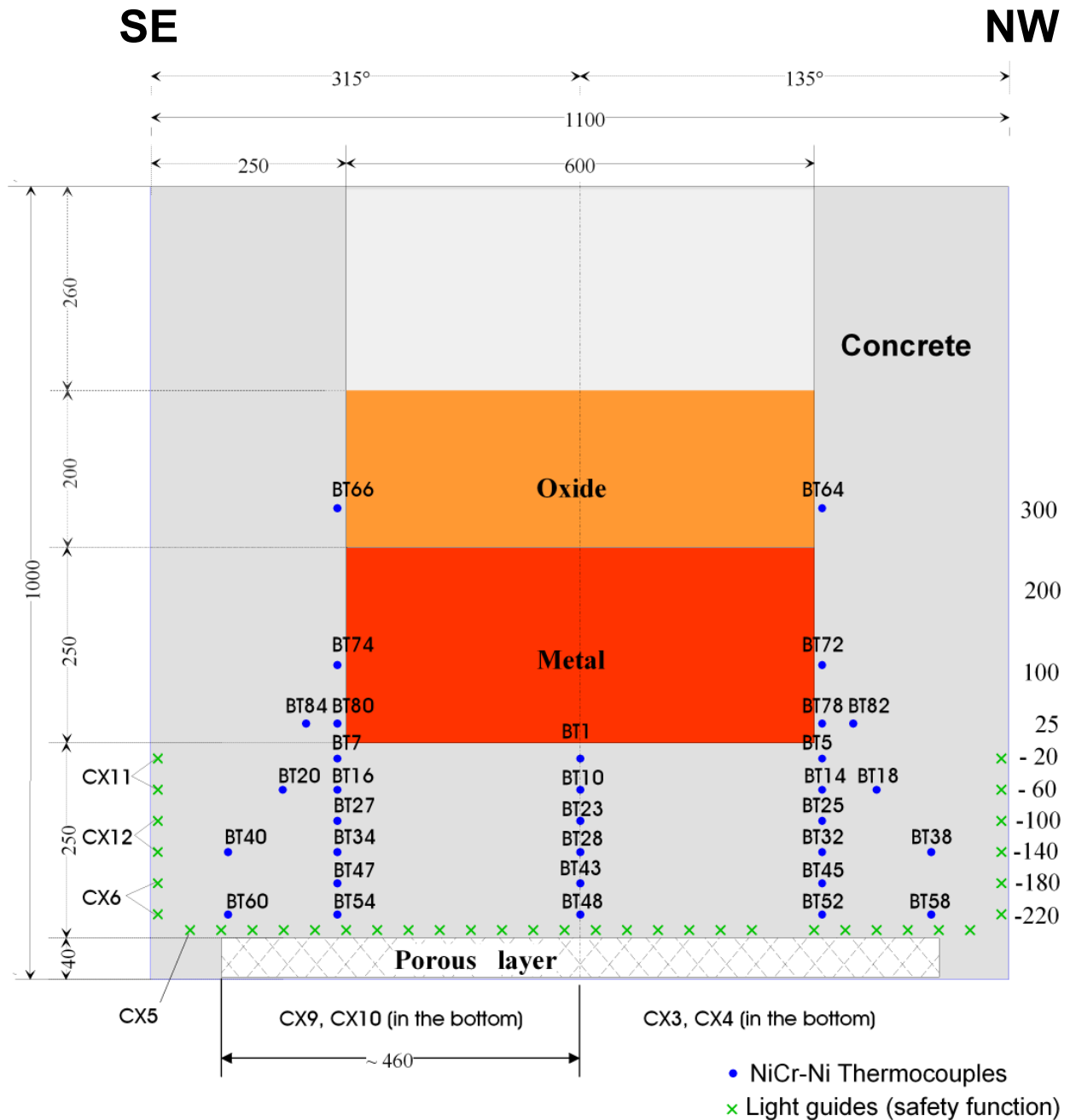
Figure 5: Positions of the thermocouples in the SE – NW plane

The light guides positioned in the outer sections of the crucible are a safety relevant instrumentation of the facility. The test will stop when the melt approaches the light guides. After their interruption the heating is switched off immediately and the melt starts to cool down. To prevent further erosion during the cooling process and to exclude a possible attack of the induction coil, the flooding of the outer surface of the crucible will start [4, 7].

3 Experiment preparation and experimental results

3.1 Preparation of the concrete crucible

A very laborious task to prepare the test was the fabrication of the concrete crucible with the embedded instrumentation. Figure 6 shows the light guides with their black plastic sheathing, located in the lower plane of the crucible, and the thermocouples that are fixed to rods of glass for exact positioning. Figures 7 to 9 show different steps to fill in the liquid concrete in the prepared mould. Figure 10 shows the final step in which the bottom porous concrete layer is prepared, during which the crucible is turned over. The curing time was more than 4 weeks so that the concrete complies with the technical specifications.

Figure 6: Instrumentation during crucible fabrication: Light guides (black sheeting) and thermocouples fixed to glass rods

Figure 7: Fabricating the bottom of the concrete crucible

Figure 8: Fabricating the concrete crucible

Figure 9: Fabrication of the cylinder wall of the concrete

Figure 10: The 4 cm thick porous concrete layer under the crucible (upside down)

3.2 Planned performance

Although substantial deviations from the planned experimental conduct did occur, a brief overview over the planned test is given here.

After preparation of the melt through thermite ignition in the external thermite vessel, the test shall start with pour of the melt into the crucible. Induction heating in the range 170 and 200 kW net power to the melt should be maintained until the declared end of the heating period. The first phase of dry concrete erosion is expected over a period of some 40 min (2400 s) until about 140 mm of concrete are eroded in the downward direction. Then, flooding should be activated by the showerhead from the top of the crucible, with a flooding rate of 0.375 l/s.

Further erosion of the concrete after flooding if it would occur, can be observed by response of the thermocouples in the concrete. Heating in the test should continue until the melt reaches the lowest layer of thermocouples at –220 mm, or until failure of the light guides, or until coolability of the melt is attained. This defines the end of the heating period.

After end of heating, the bottom and sidewall of the concrete crucible are planned to be flooded by water supplied to the bottom layer of porous concrete to exclude any attack of the heating coil by the hot (solidifying) melt. The addition of water from the bottom shall stabilize the residual crucible, without changing its geometrical structure. Careful disassembly of the test rig will start after complete cool-down of the melt.

The intended steps of the experiment are briefly summarized in Table 3

Table 3: Planned conduct of COMET-L1

Time, s	Event
- 1800	Start of argon cover gas flow
- 150	Start of induction heating system with U = 2, 2 kV, no melt in crucible
90	Ignition of thermite
0	Start of melt pour, 612 kg melt
~ 20	End of pouring.
60	The hood is closed.
> 120	Net heating power between 170 and 200 kW.
~ 2400	14 cm axial erosion reached, start of top flooding with water flow 0.375 l/s.
~ 3600	25 cm axial or radial erosion depth reached, induction heating stopped.
Post test	After end of heating: Cooling continues by further addition and drainage of water to/from the crucible. Cooling of the melt allowed over ~ 36 h.

3.3   Realised performance

The COMET-L1 test was performed July 10, 2004. Control of the experiment took place from the control room with all equipment for online measurements, as shown in Figure 11

Figure 11: The control room with operator panel and video installation

After careful preparation of the test and check of all measurement and control systems, inertisation of the test rig by argon cover gas flow started 30 min before pour of the melt. The induction heating system was started and operated under the nominated voltage. The mixed and pre-heated thermite powder was ignited in the external vessel 90 seconds before the pouring. The thermite reaction was completed after 40 seconds. After further 50 s to allow separation of the metal and the oxide phases, the major part of the melt was discharged into the concrete vessel. This defines time t = 0, corresponding to 11:00 local time depicted in some of the video registrations. Release of the melt to the concrete cavity took 60 s.

Because of a disturbance in the weighting system, the mass of the poured melt was 927 kg instead of the planned 612 kg. The actual masses determined after the test are therefore 460 kg steel plus 467 kg oxide, which increased the total height of the melt (without void) to 780 mm, with 240 mm steel and 540 mm oxide. The initial temperature of the melt as measured in the spout was 1640 °C. The densities of the melt were confirmed by its volume in the thermite crucible at this temperature and are 6940 kg/m^3 for the metal and 2850 kg/m^3 for the oxide melt. The most significant events during the test sequence are listed in Table 4.

Table 4: COMET-L1 Event Sequence

Time, s	Event
- 162	Induction system started, voltage 2.2 kV
- 90	Ignition of thermite powder to prepare high temperature metal plus oxide melt
0	Start of melt pour while induction coil is operating continuously
60	End of melt pour, 927 kg melt were released into concrete vessel
80	Hood closed; H2 flame at end of off-gas line. Strong agitation of melt surface by gases from decomposing concrete with minor aerosol release. Surface of agitated melt mostly close or slightly below upper edge of the MgO ring. Melt is occasionally ejected above the upper edge of the MgO ring.
90	Net decay heating power in the melt too low (80 kW instead of planned 200 kW). Voltage for induction coil increased by operator to maximum level of 2.6 kV, brings power to ~120 kW. Inductor voltage remains subsequently unchanged until end of heating.
115	Clear picture from the melt surface, melt strongly agitated. Oxide melt has low viscosity. Surface of melt ~ 8 cm below the upper edge of the MgO ring.
150	Intense agitation of melt surface continues. Surface ~10 cm below upper edge of the MgO ring.
175	Slow increase of net power as melt comes closer to induction coil by ongoing concrete erosion. End of H2 flame at off-gas line.
200	Oxide melt further on with low viscosity and strongly agitated by gas release, melt level about 15 cm below the upper edge of the MgO-ring.
260	In central part of the melt surface, dark material is transported from the bulk to the surface (splashed concrete or crust?)
330	Further increase of net power to ~140 kW by ongoing concrete erosion. Melt still strongly agitated with slightly increased viscosity, some mild melt eruptions. Melt level decreased, now slightly above the upper edge of the concrete crucible. Thermocouples indicate downward erosion front at –60 mm level.
400	Melt surface more viscous, dark (cold) material rises from the bulk near the west wall. Melt less agitated with some periods of more intense eruptions.
450	Thin floating surface crust has formed with many cracks. Bright bulk of the melt visible under the darker crust. No splash-out of melt during this period.
493	Preceding quiet period is interrupted by moderate eruptions with higher gas release.
520 - 600	Several periods of moderate eruptions and higher gas release. Crusted surface reduces, some 80 % of the surface covered by floating crumbly crust. Viscosity of oxide melt has increased
620	Floating crust reduces to some 30 % of the surface. Re-melting of crust occurs mainly by splashed melt that is ejected by gas bubbles, covers and submerges the existing floating crust. Gas release and agitation are increased. Induced power ~150 kW

Table 4: COMET-L1 Event Sequence (continued)

Time, s	Event
725-750	Melt surface mostly covered by darker viscous layer, only 10 - 20 % crumbly crust. Gas release equally distributed over the upper surface of the melt. Under the darker surface bright melt visible when gas bubbles are released.
800	Crust has formed on upper edge of the concrete crucible, protruding up to 5 cm over the inner 600 mm diameter of the concrete crucible. Level of melt reduced a few cm below upper edge of concrete crucible. Crust and melt separated. Melt covered by viscous skin and some thin, crumbly crust. Thermocouples indicate downward erosion > 60 mm, probably to 80–90 mm; maximal radial concrete erosion is some 50 mm near south. Induced power 153 kW, temperature at bottom of crucible 20°C only.
900	Induced power 150 kW. Again thin crumbly surface crust has developed covering 80 % of the bright melt. Gas bubbles eject some melt onto the surface of the crust. This process reduces the size of the floating crust during the next 30 s. Bottom of crucible at 20°C. Slow release of steam from end of off-gas line.
925	Period of higher gas release. Mayor melt ejection at 940 s. All surface crust disappears. Melt has medium viscosity
958	Induction heating off due to failure of frequency converter. Restart of heating not successful. Without decay heat, continuous cool-down of melt during the further test.
1100	In spite of missing decay heat, melt continuously agitated by ongoing gas release. Melt surface covered by thin viscous layer and partial crust.
1370	Melt covered by thin crumbly crust; bright melt underneath still at high temperature and continuously agitated by gases. Metal layer seems permeable for gases. Steam at end of off-gas tube. Temperature of bottom crucible is still low.
1500	Decision, that surface of the melt shall not be flooded by water, to observe ongoing dry concrete erosion and cool-down of melt
1800	Downward concrete erosion between 60 to 80 mm. Only slow cool-down of oxide melt.
2230	Surface of oxide melt dark with bright white cracks from melt below. Slow release of condensing steam from end of off-gas tube. Thermocouples in concrete crucible show only 30°C at lower bottom and outer sidewalls.
2500	Still bright melt under crumbly crust; condensing steam in off-gas flow. Temperature in lower crucible between 21 and 32°C, as recorded by TCs.
3300	Surface of crusted melt is crumbly with bright cracks from oxide melt below. As a precaution to protect the induction coil, the bottom layer of porous concrete was successfully flooded by water between 3030 and 3300 s. Flooding has no effect on the status of the melt. The presence of water would keep the bottom concrete cold.
3800	Additional flooding of the porous sideward gap performed via bottom flooding in the period 3715 – 3970 s with 0,85 l/s. IR-camera registers steam, as a small volume of water penetrated to the surface of the crusted melt
4440	Again flooding of the outer cylinder gap, until water enters the surface of the crusted melt. Water evaporates from the crusted surface, which is dry afterwards.

Table 4: COMET-L1 Event Sequence (continued)

Time, s	Event
4500	Lights on in crucible, gray surface crust visible, in central part bright oxide material still visible through cracks in upper crust
4770	Further flooding initiated through water addition via the porous bottom layer and overflow to the crusted surface through the outer cylinder gap. Increased steam flow in the off-gas tube. As surface of the melt is kept flooded, continuous steam flow through off-gas tube, remaining nearly at the same level until end of video recording after 2 hours.
4880	20 – 30 % of the crusted melt surface covered by water. Bright spots cool down, surface uniformly dark. Flooding of the surface is a mild process.
5250	Melt surface completely flooded by boiling water.
5520	Water level 20-30 cm above crust surface (a few cm below upper edge of MgO ring)
7900	Through repeated flooding from the cylinder gap, melt remains covered by 20 – 30 cm water. Boiling produces small steam flow through off-gas tube. Maximum temperature registered by Type K-TCs in concrete near the erosion front is 700 – 1000°C. Temperature of gases in off-gas tube is 100°C, so that no condensation of steam occurs. This allows a clear view to the boiling water layer.
9500	First activation of showerhead for further flooding. Iterative flooding and drain of coolant water to extract heat and to preserve the test status.
14400	Temperature near the erosion front nearly unchanged at 850°C, in spite of continued cooling of all sides of the crucible. Flooding and draining of the water are continued until 23000 s
20000	very slow cool-down of the melt continues, 750 to 800°C
27500	Long-term registration of measurements by Microlink data acquisition is continued by restart of phase 4 after copy of data between 15:00 and 16:38.

Important subjects concerning the conduct of the test are as follows:

- The net power that could be supplied to the melt was smaller than expected. This is due to the high distance between the electrical induction coil and the melt, which corresponds mainly to the erodable concrete layer. In spite of increase of the inductor voltage to its maximum level, only 150 to 160 kW typical could be supplied instead of the planned 170 - 200 kW. As expected, the power input increases during the test, when the melt approaches the induction coil.

- Induction heating ended after 958 s due to electrical failure of a power control board. In spite of different actions, the power could not be restarted. This strongly influenced the further course of the test. At that time, the melt had eroded some 60 mm concrete into the downward direction.

- Failure of further decay heating limited the process of ongoing concrete erosion. Consequently, top flooding of the melt during sustained heating was not possible. Instead of that, the following procedure was followed during the further course of the test:

- o The hot melt was allowed to continue MCCI under dry conditions until no further erosion was observed and the melt surface was covered by a massive crust.

- o 3000 s after pour of the melt, water was supplied to the porous layer under the crucible and to its sidewalls to keep the outside of the crucible cold and to exclude uncontrolled heat-up of the induction coil.

- o In the end, the surface of the melt was flooded by water through overflow from the sides and by top flooding from the showerhead to observe further cool-down of the partly solidified melt.

- To remove the energy, iterative flooding and draining of water was performed. Careful disassembly started two days after the test.

Figure 12 shows characteristic phases of the test as seen from the hood of the test assembly: (a) shows pour of the denser metal melt from top right, subsequently followed by the oxide melt (b). Figure 6 c shows the surface of the oxidic melt agitated by gases from the decomposing concrete. No crust exists on the surface, a situation that occurred in the early test phase until 450 s and also later on at 940 s when due to stronger melt eruption the crust was flooded and submerged. (d) shows a partially encrusted oxide surface at 730 s.
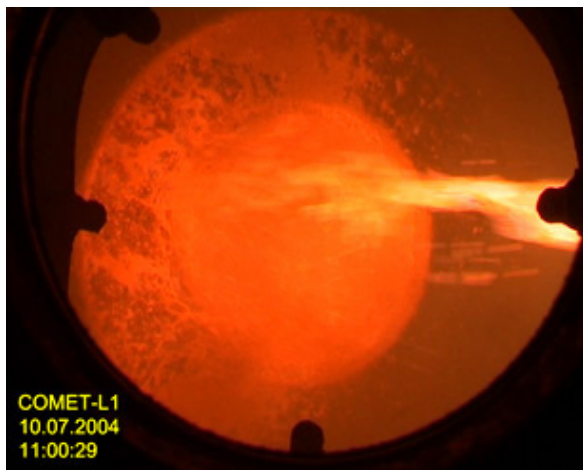
(a) Melt pour (metal) at 29 s	(b) Melt pour (oxide) at 46 s
(c) Agitated oxide melt surface at 175 s	(d) Partially encrusted melt surface at 731 s
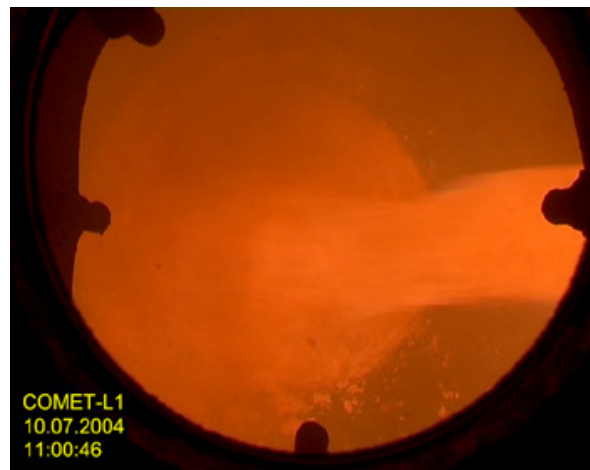
Figure 12: Video pictures: View onto the melt surface at different phases of the test

3.4 Test results

3.4.1 Mass and temperature of the melt

The mass that was planned to be poured to the concrete crucible - as described in chapter 2.3 - should be 612 kg (459 kg metal and 153 kg oxide). The total melt generated by the thermite reaction was 959 kg. The rest of the oxide melt should be poured into the slag container.

The control of the pouring process was, however, disturbed by a measurement error of the weighting system. The registered mass of the thermite reaction vessel is given in Figure 13. Ignition of thermite took place at –90 s. At the same time, the spout moved automatically under the thermite vessel and – as slightly higher than in previous experiments – contacted the bottom of the vessel. This resulted in a systematic error and a virtual loss of the weight of the vessel, that reduced from 850 to some 600 kg (Figure 13). The operator was not aware of the unexpected situation and started release of 612 kg melt between 0 and 60 s. Consequently, the total melt mass that was released to the concrete vessel, was **927 kg, with 460 kg steel and 467 kg oxide**. This higher mass was confirmed by careful post-test weighting of the thermite vessel, spout, and slag wagon, and also by the higher melt level in the concrete crucible, observed in the video.
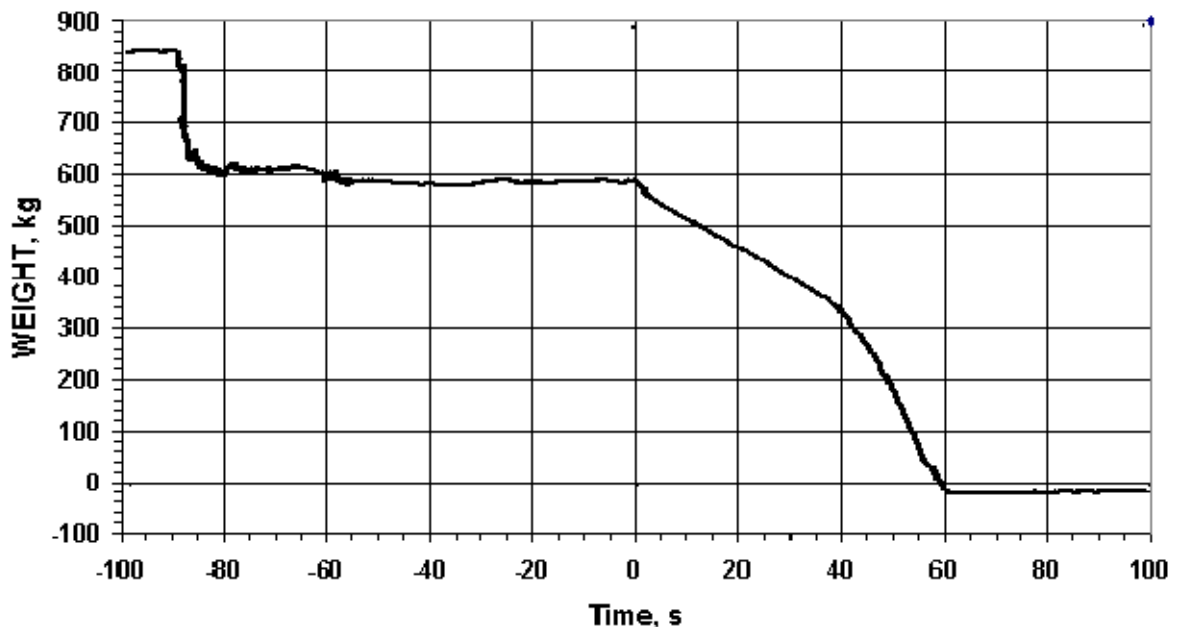
Figure 13: Weight of themite reaction tank during thermite burn and melt release

The weight plot in Figure 13 shows that the thermite burn is completed at -55 s, when the high frequency oscillations come to an end. The slope of the weight curve between 0 and 60 s characterizes the melt release, but is disturbed by the measurement error. Under normal conditions, a clear transition from metal to oxide melt is visible, with a steeper slop for the metal phase first and a more gentle slop for the later oxide phase. This information is not available for the present test.

The temperature of the melt after end of the thermite reaction was expected to reach 1800°C (2073 K). Actually, the initial temperature of the melt, measured by a W/Re thermocouple in the spout from 40 to 60 s during release of oxide melt, was 1640°C (1913 K) (Figure 14). Former experiments have shown that at end of the thermite reaction steel and oxide melt have the same initial temperature as expected. The lower temperature measured during the earlier melt release in Figure 14, is probably due to a crust that may have formed at the tip of the thermocouple.
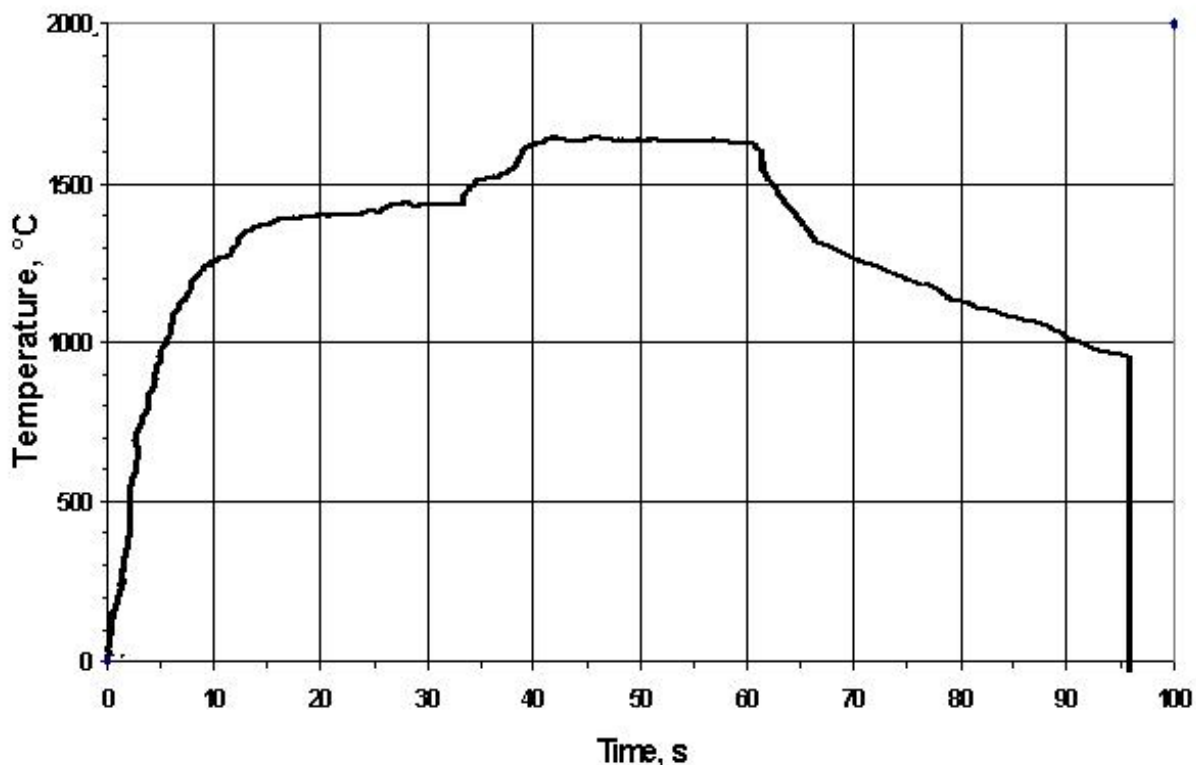
Figure 14: Temperature of the melt in the spout

The W-Re-thermocouples that that were located in the crucible (Figure 4) failed before they reached the steady temperature. Therefore, no direct thermocouple measurements exist for the temperature of the metal or oxide melt during erosion of the concrete crucible.

The pouring process has been recorded by video and infrared cameras. Figure 15 shows the view from the hood of the crucible during pour of the metallic and oxidic melts, respectively. The upper section is the video view, the middle is the same scene as registered by the infrared camera. By selection of the adequate emissivity of the melt surface, the lower section shows the histogram of the temperature distribution from the jet surface. The 1640 °C level is clearly recorded. The associated emissivities are 0.5 for steel and 0.92 for the oxide melt. With these emissivities, further temperatures of the melt surface were determined for later phases of the
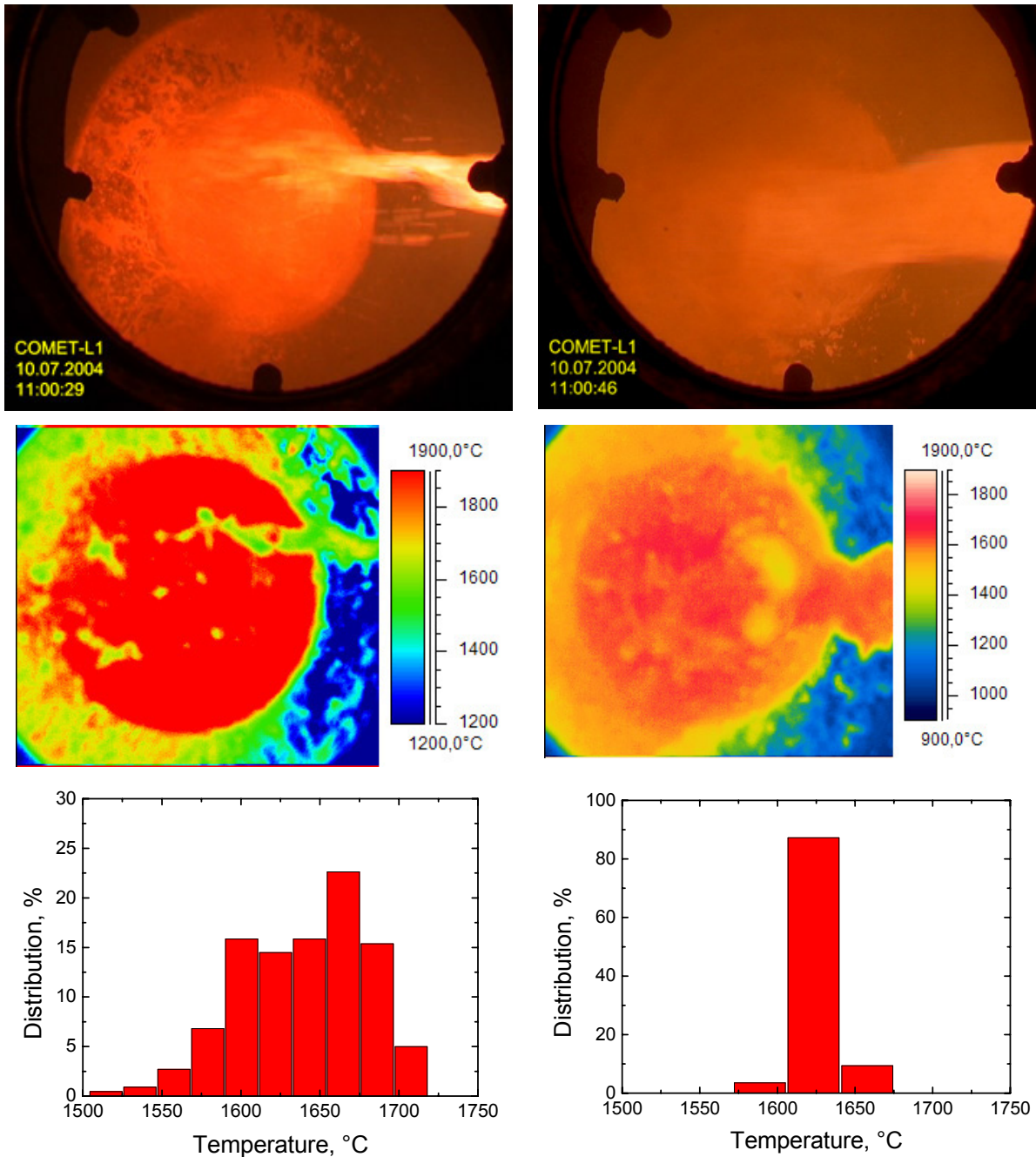
Figure 15: Temperature of the metallic melt jet (left) and of the oxidic melt jet (right). The upper video picture corresponds to the infrared picture in the middle. Temperature histograms from the melt jet are plotted below.

experiment. It is the first time, that a high quality infrared video camera was successfully used to obtain important information of the oxide temperatures.

This evaluation was performed for the surface of the oxidic melt for the first 3000 s of the test, using the predefined oxide emissivity. The minimum and maximum temperatures of the oxidic melt surface are plotted in Figure 16. For the heating period until 958 s and shortly after, the maximum temperature can be reasonably assigned to the temperature of the bulk of the oxide melt, as represented by fresh material that is transported to the surface, e.g. by rising gas bubbles. After the fast decrease of the melt overheat, these temperatures are in the liquidus/solidus range of the oxide melt mixture. The minimum temperature in the period from 500 to 950 s and after 1200 s represents the temperature of the crust on the melt surface. After end of heating, the temperature drop of the crust is significantly faster than of the melt. During the heating phase from 500 to 950 s, the temperatures indicate a quasi-stationary status of the melt, in that the simulated decay heat is in equilibrium with the heat losses to the boundaries, causing the temperature of the melt to remain relatively constant.

IR registration gives however no quantitative information when water is added to the surface of the melt, as water is opaque for IR radiation.
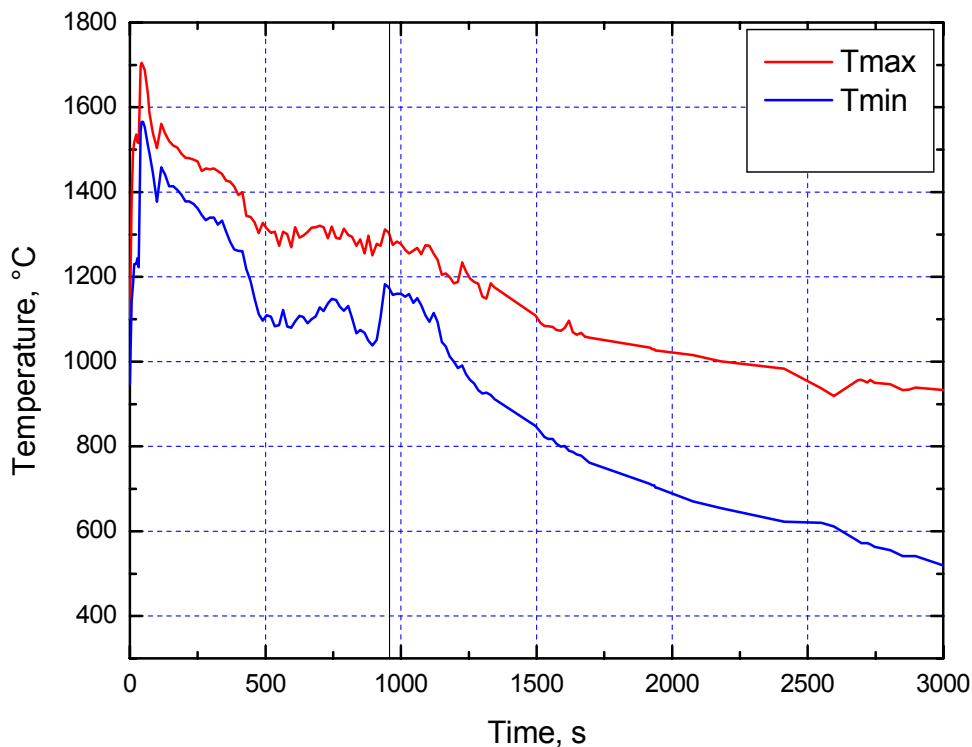
Figure 16: Evolution of surface temperatures of the oxide melt measured by the IR camera. End of heating marked by line at 958 s.

3.4.2 Decay heat simulation and melt behaviour

Operation of the induction system to simulate the internal decay heat in the melt was started some 2 minutes before the melt was poured into the crucible. The voltage of the induction coil was controlled by the operator throughout the heating period, to achieve the net power input to the melt according to the test plan. Online measurements of the net power and of the total power gave the necessary information to the operator.

Figure 17 and Figure 18 show the characteristics of decay heat simulation by induction heating. Besides the important information on power input and induction voltage, the efficiency of heating and the power fluctuations allow qualitative estimates on the status of the steel melt, as the geometry of the metal influences the electromagnetic coupling to the induction field.

The operator controls the induction voltage to achieve the desired net heating power. Initial power input was considerably lower than planned. Therefore, the operator increases the voltage at 90 s from 2.2. kV to the maximum allowed value of 2.6 kV, remaining constant until end of heating at 958 s. This brings the net input power to ~120 kW at 100 s, which is still below the desired 200 kW. The slight improvement of the very small heating efficiency (Figure 18) is due to the ongoing downward concrete erosion, which brings the metal melt closer to the induction coil and finally deposits 150 kW in the metal melt. Major fluctuations in net power and efficiency occur until 600 s and are the consequences of melt relocations. This correlates with different events that were visible at the surface of the melt, namely transport of dark material, probably detached crusts, from the bulk of the melt to its surface at 260 s and 400 s, and several more pronounced gas eruptions from 500 to 600 s. In this period, a partial surface crust is formed that is to some extent re-melted by fresh melt transferred from the bulk of the melt to the top crust.

From 600 to 900 s, fluctuations in power input are considerably reduced, as the metal melt has probably formed a closed crust near the concrete interface. Gas release and concrete erosion have reached a reduced level, and the temperature of the oxide melt is nearly constant (Figure 16). The surface of the melt is mostly covered by a crumbly crust. This phase ends when at 940 s major melt agitation and melt ejection occurs, leading to complete re-melting of the surface crust. This correlates with a clear increase of the power input (Figure 17) and indicates that some concrete material that accumulated under the metal is released, and the metal phase comes closer to the induction coil. Unfortunately, induction heating ends shortly after.
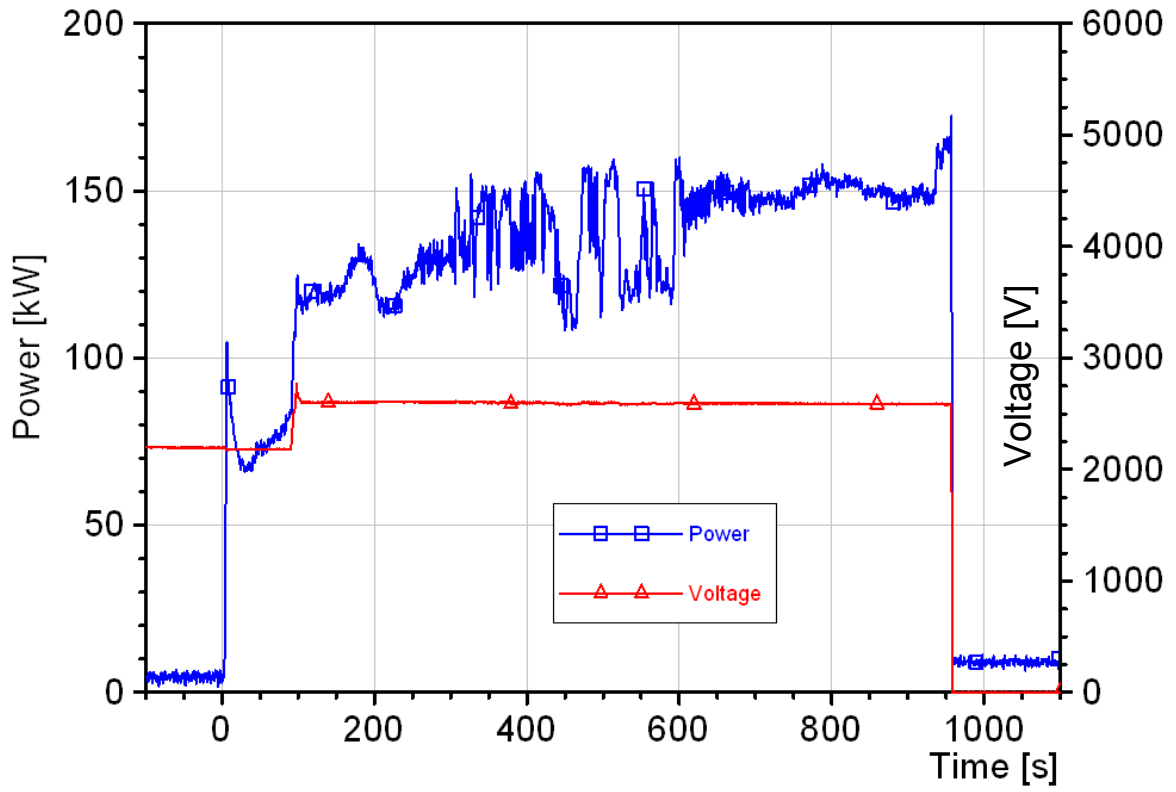
Figure 17 Net heating power in the melt and voltage of induction coil
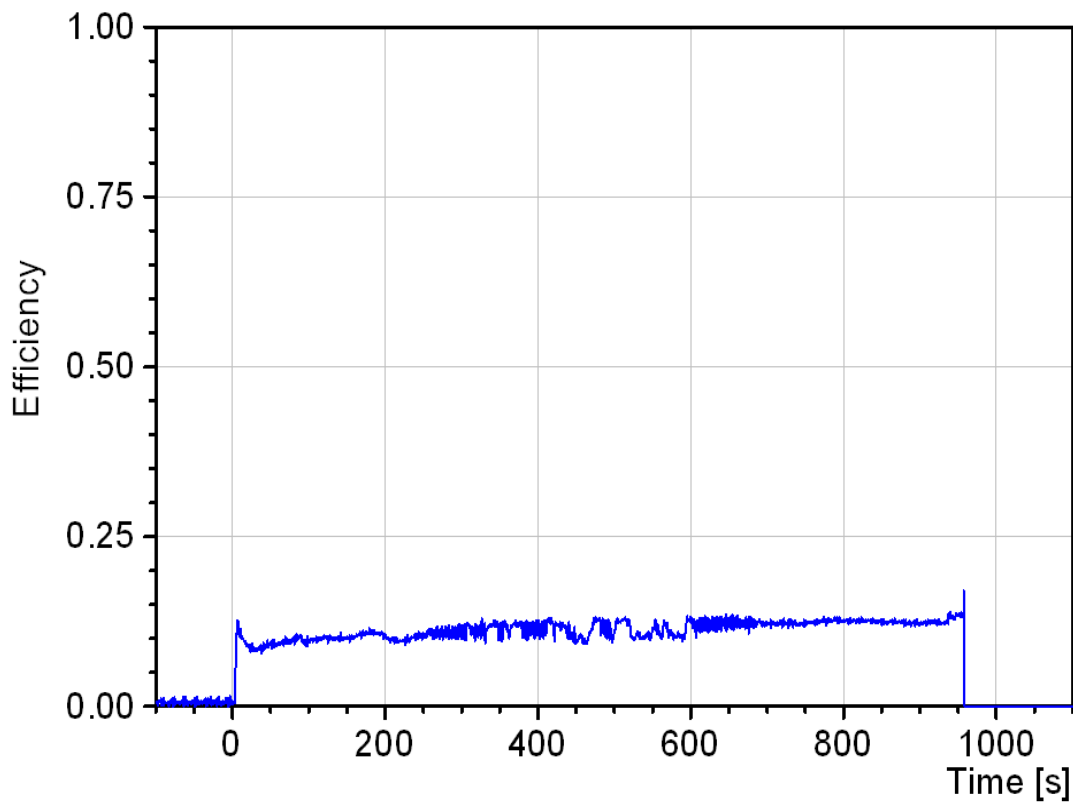
Figure 18: Efficiency of the induction heating, referred to the gross heating power

At 958 seconds, induction heating was interrupted by electrical failure of the frequency converter No. 4. After various attempts to re-establish the induction heating, the control board of the frequency converters were changed. However, restart of the heating was not successful. Therefore, after 1370 seconds no further efforts were made to reactivate the induction heating[1]. The experiment was continued with slow cool-down of the melt.
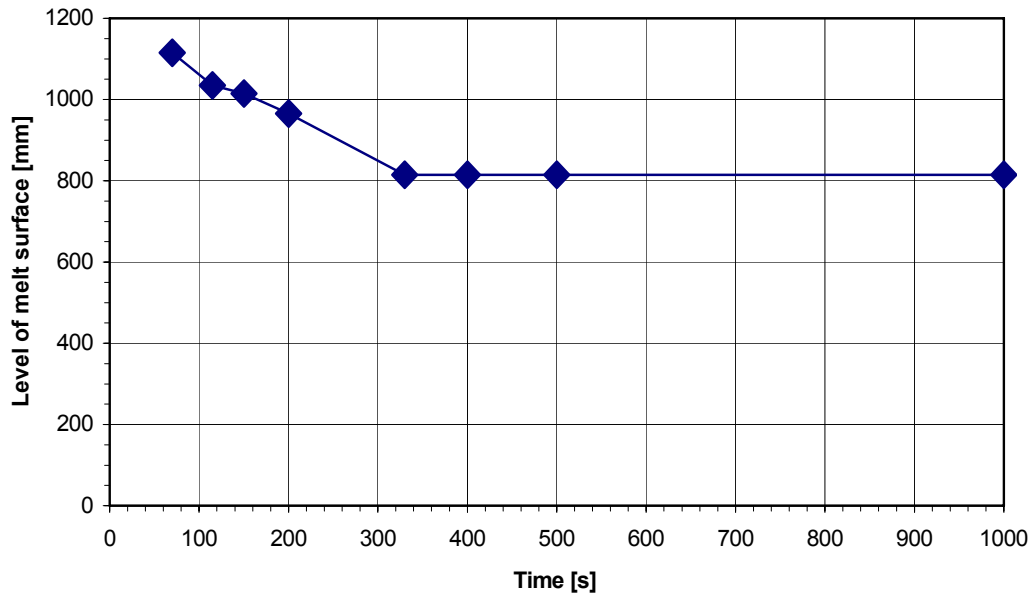
Figure 19: Level of the upper melt surface as estimated from video observation

The level of the melt surface in the crucible decreases during the test mainly because of different void content predominantly in the oxide melt (Figure 19). The void was highest in the first phase of the interaction and led to an increase in the melt level by ~400 mm, corresponding to a void in the oxide of ~50 %. At ~400 s, the melt had collapsed considerably. Because of existing crusts, the estimation of the residual void is difficult, but may be on the order of ~20 %.

The viscosity of the oxide underwent different states: The low viscosity at the beginning increased to higher values when the temperature was reduced. Admixture of melted concrete, mainly silica, subsequently reduced the viscosity, especially shortly before "power off", when after release of accumulated concrete the crust re-melted and a crust free surface appeared. This shows that the oxide properties are substantially changed both by temperature and composition. Admixture of silica is also important for the liquidus solidus range of the oxide melt which is extended towards lower temperatures by increasing silica content.

---

[1] Repair by a specialist in power electronics was successful after the test, but localisation of the defects took more than one day.

3.4.3 Concrete erosion and cavity shape

Because of the early interruption of the heating phase in the test, the erosion process is not as pronounced as expected. Therefore, quantitative details are presented here with due caution.

The interaction of melt and concrete in the first period of the test until some 200 s is characterized by significant agitation and some splashing of the upper oxide melt layer, caused by high gas release from the decomposing concrete. In this time period, axial and lateral erosion rates of the cavity by the metal melt are similar and mainly controlled by the overheat of the melt, and hence decrease rapidly during the first few hundred seconds. The initial, high erosion rate is dominated by the metal melt at the lower crucible, and leads to fast reduction of the overheat of the melt. Subsequently, erosion is delayed, as a balance between simulated decay heat and heat losses to the boundaries has established, and there is a high probability, that the metal melt starts to form crusts at the concrete interface.

For a detailed analysis of concrete erosion rates and cavity shape, the failure times of thermocouples that are embedded in the concrete cavity are evaluated. The thermocouples are positioned in two separate planes, namely SW – NE and SE – NW. As more thermocouples are placed in the SW-NE plane, the information gathered from this plane provides a more complete information.

In each instrumentation plane(Figure 20 and Figure 21), specific lines were defined along which the erosion was evaluated. Each line includes a set of thermocouples. The SW – NE plane (Figure 20) has seven lines t1 - t7, the SE – NW plane (Figure 21) has five lines. Moreover, each side of the main planes (left / right) was examined separately as the erosion was not symmetric. The left part is identified by the "-" sign.

The heights (depth) in mm, where the thermocouples are located, are shown on the right side of Figure 20 and Figure 21. In radial direction, the thermocouples are positioned at the following radii: 0 mm $\leftrightarrow$ (centre line); 180 mm $\leftrightarrow$ (only for thermocouples in SW – NE plane lines t2 and "-"t2); 310 mm $\leftrightarrow$ (lines t3 and "-"t3); 350mm; 380 mm; 420 mm ; 460 mm, and 500 mm. A detailed listing of the location of all thermocouples and their assignment to the data acquisition are given in Appendix B, Table B1.
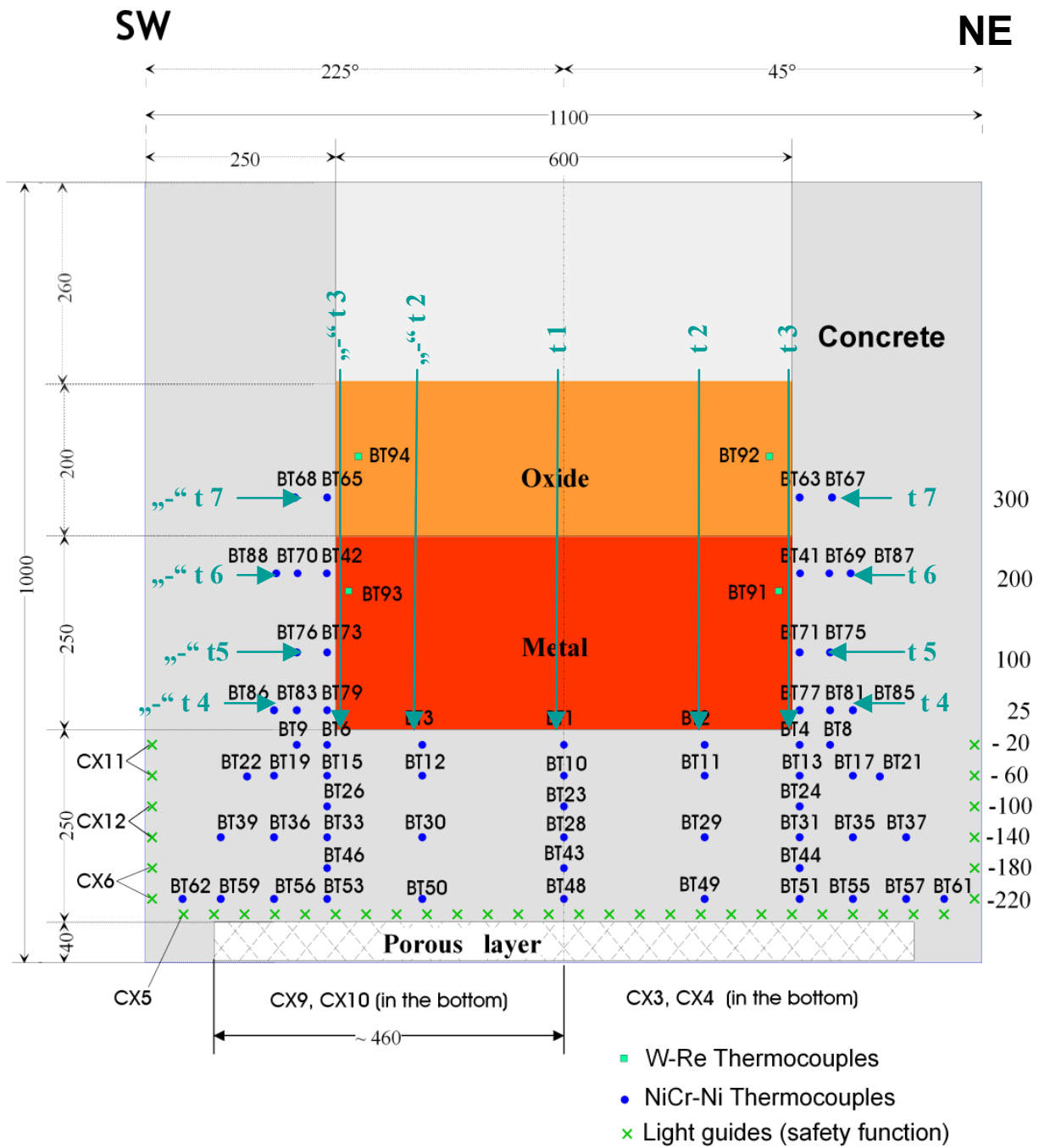
Figure 20: SW – NE plane with the location of the TC's and the seven lines t1 - t7
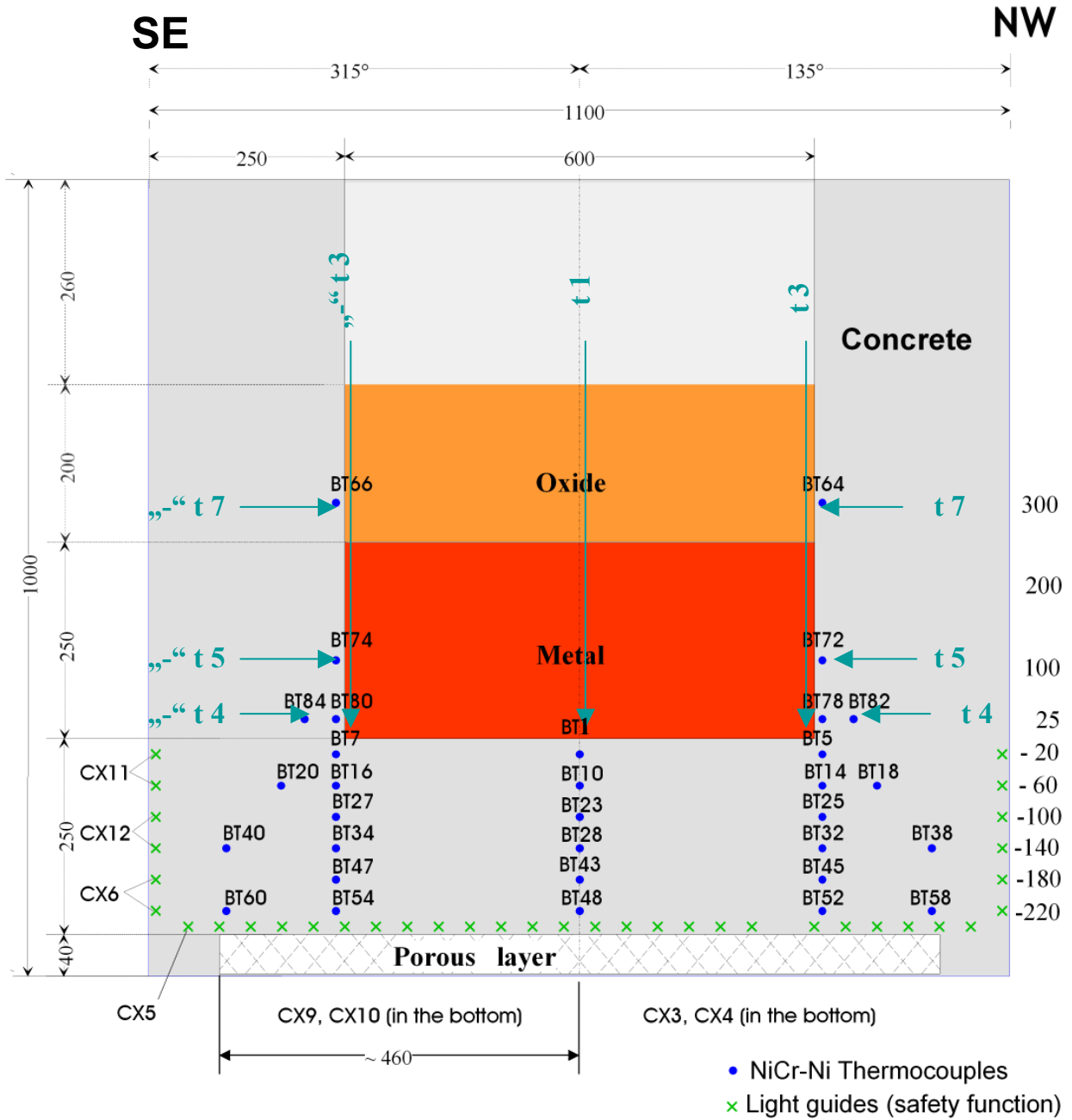
Figure 21: SE – NW plane and location of the TC's with five lines

Table 5 gives the position of each instrumentation line.

Table 5: Lines location

Line			Position, mm		
t 1			r = 0		
t 2	/	"-" t 2	r = 180	/	-180
t 3	/	"-" t3	r = 310	/	-310
t 4	/	"-" t 4	z = 25 right	/	25 left
t 5	/	"-" t 5	z = 100 right	/	100 left
t 6	/	"-" t 6	z = 200 right	/	200 left
t 7	/	"-" t 7	z = 300 right	/	300 left

The actual erosion front is defined by failure of the thermocouples (the complete signals are given in Appendix C, Figure C1 to C13). Thermocouples with incorrect signals are neglected. Thermocouples BT 36 and 60 were defect already before the test. Further on, thermocouples BT45 and BT 64 seem to be interchanged. Their signals are used accordingly.

Concrete erosion versus time in SW – NE plane is presented in Figure 22, the erosion in SE – NW plane is shown in Figure 23. The solid lines are derived from thermocouples staggered in the vertical direction, the dotted lines for the lateral direction. Only few discrete measurement points exist for failure of the thermocouples. Downward erosion stopped between the -60 and –100 mm instrumentation plane and probably did not exceed –80 mm. Maximum radial erosion is some 50 mm only through the metal phase (detected by 1 thermocouple only), and some 10 mm through the oxide phase at the 300 mm instrumentation level.

For the first 100 to 200 s with the high erosion rate, there is the tendency that the erosion rates by the metal phase are rather similar in the downward and sideward direction and are in the region of 0.15 mm/s, possibly slightly lower in the lateral direction with 0.11 mm/s. This high erosion rate by the metal melt is due to the initial overheat of the melt, which reduces quickly as measured by the IR camera in Figure 16. With cool-down of the melt, erosion rates until 500 s reduce to ~0.07 mm/s, as seen by the smaller slope of the lines. Thereafter, crusts are expected to form at the concrete interface leading to further reduction of the erosion rates. However, as no thermocouple was contacted at the –100 mm plane, no data are available.
As the erosion by the oxide melt is rather low, cavity formation is clearly dominated by the metal melt.
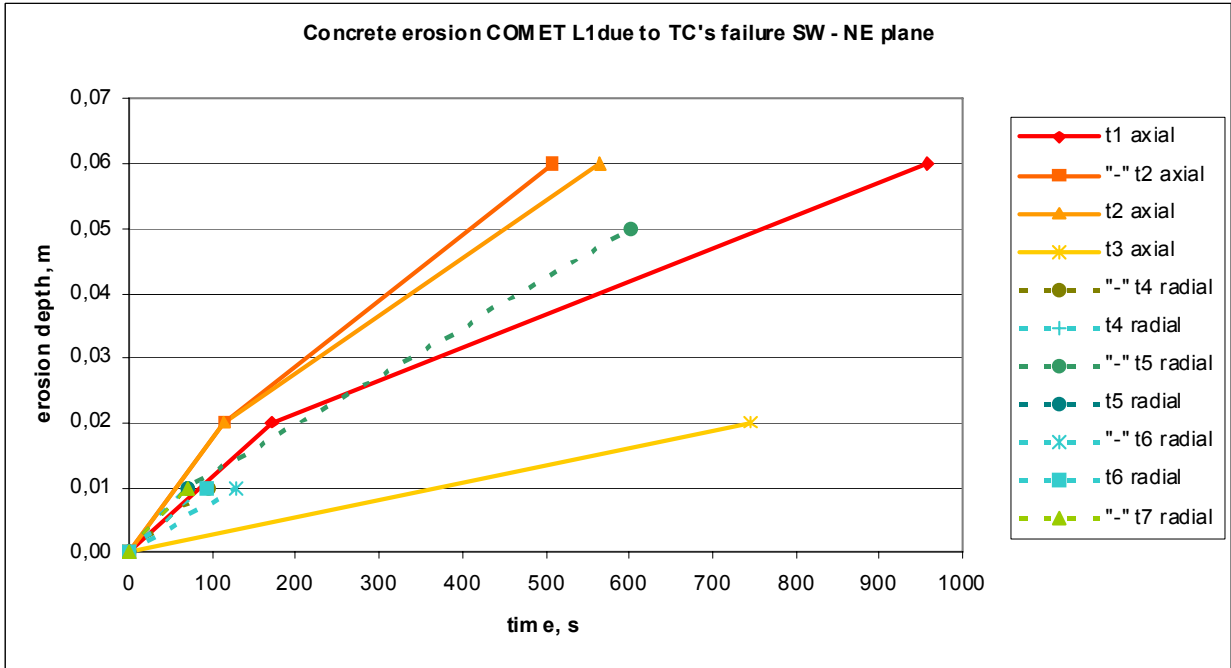
Figure 22: Concrete erosion in SW – NE plane.

Solid lines – downwards; dotted lines – sidewards
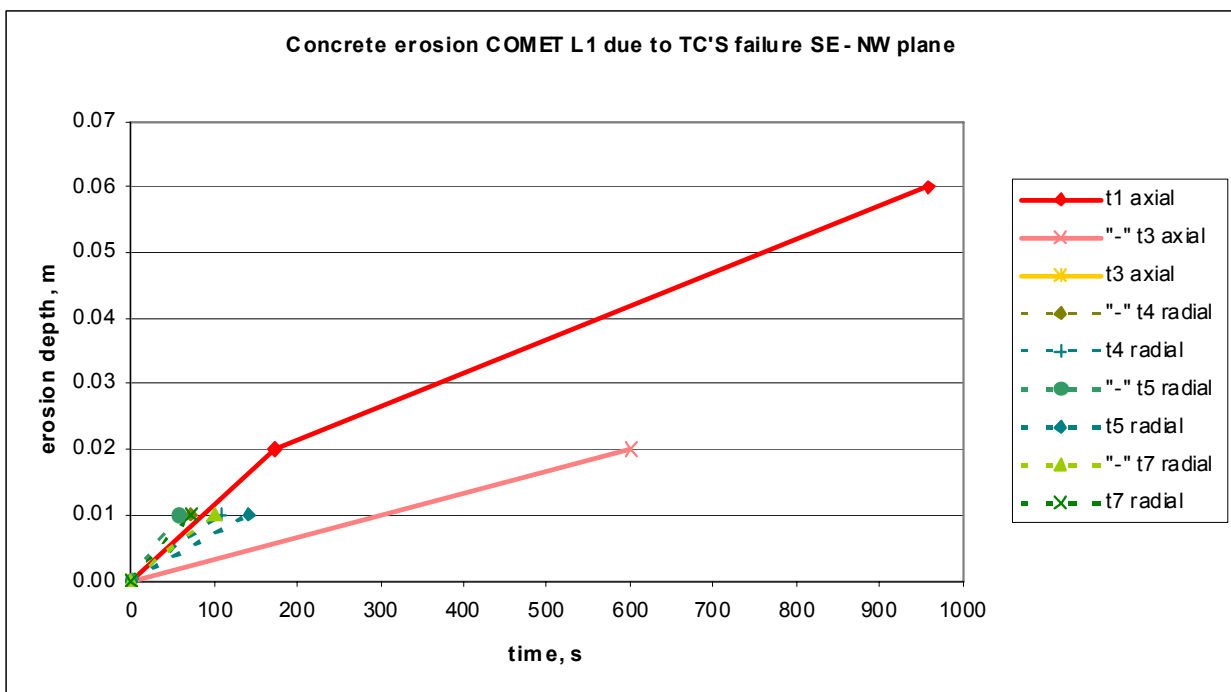
Figure 23: Concrete erosion in SE – NW plane

Solid lines – downwards; dotted lines - sidewards

Thermocouples in the centreline failed later than those positioned on lines "-" t 2 and t 2. A reason for that may be the lower induction field in the axis of the induction coil. Furthermore the erosion in the bottom corners of the crucible is slower than on the "plane" surfaces on bottom and sidewall. Only one of the thermocouples located near the corner failed during the heating period. This is due to geometrical reasons: Heat delivered to the surface of the 2-d corner is more easily conducted to the bulk of the concrete than from an even surface in 1-d geometry. This results in slower heat up and erosion.

To estimate the final cavity erosion, the temperature behaviour of the thermocouples near the erosion front was evaluated versus time. Those thermocouples near the erosion front that did not fail show a significant increase of the temperature. From this magnitude and velocity of the temperature rise, the distance to the melt front was estimated. As a result, Table 6 and Table 7 give the estimated, eroded concrete depth and the uncertainty band of the front position along the lines t1 through t7 in the instrumentation planes SW–NE and SE-NW, respectively, as evaluated independently by two persons.

Figure 24 and Figure 25 present the cavity shapes for the planes SW–NE and SE-NW, respectively. The figures include the initial cavity at time 0, the (inner) cavity as defined by failed thermocouples at time 958 s, and the uncertainty band as defined by estimation of the final cavity described above. Because of lack of further information, the individual points are connected by straight lines. It is important to note that the depression at the bottom of the cavity at the ±180 mm radius, that is measured in the plane SW-NE, is not visible in the plane SE-NW because of lack of thermocouple instrumentation at that radius.

These estimates are compared in Section 3.4.6 with information that is determined from the sectioned crucible, which became available several months after the test (Figure 39). For a future experiment, a more dense thermocouple instrumentation would be highly desirable. However, this is limited by technical and financial restrictions.

An important and, in spite of all uncertainties, reliable result is the clear anisotropic behaviour of axial and radial erosion later in the test, mainly in the time period 600 – 1000 s, after removal of the overheat of the metal melt. Slow concrete erosion and the lack of major power oscillations (Figure 17) indicate that the metal phase has formed a crust, because decay heat is too low to keep the melt completely liquid. This is also predicted by computer calculations with the WECHSL code. The consequence is, that the encrusted metal melt tends to penetrate

Table 6: Final concrete erosion in plane SW-NE, estimated from temperature behaviour

Line	Estimation 1, cm	Estimation 2, cm
t 1	4 - 6	4 - 6
„-" t 2	7.5 – 9	8 – 10
t 2	7 – 8.5	7 – 9
„-" t 3	1.7	1.7
t 3	2.5	2.5
„-" t 4	3 - 4	3 - 4
t 4	3 - 4	3 - 4
„-" t 5	6 -7	6 - 8
t 5	1.6 - 2	2.5 – 3.5
„-"t 6	2.5 - 3	3.5 – 4.5
t 6	3 - 4	3.5 – 4.5
„-" t 7	2 - 3	1.5 - 3
t 7	No failure	1.5 - 3

Table 7: Final concrete erosion in plane SE-NW, estimated from temperature behaviour

Line	Estimation 1, cm	Estimation 2, cm
t 1	4 - 6	4 - 6
„-" t 3	2.5 – 3	2.5 – 3
t 3	1.9	1.7
„-" t 4	2.5 – 3.5	3 – 4
t 4	2.5 – 3	2.5 – 3.5
„-" t 5	1 – 2.5	2.5 – 4
t 5	1 – 2.5	2.2 – 4
„-"t 7	1 - 2	1.5 - 3
t 7	1 - 2	1.5 – 3
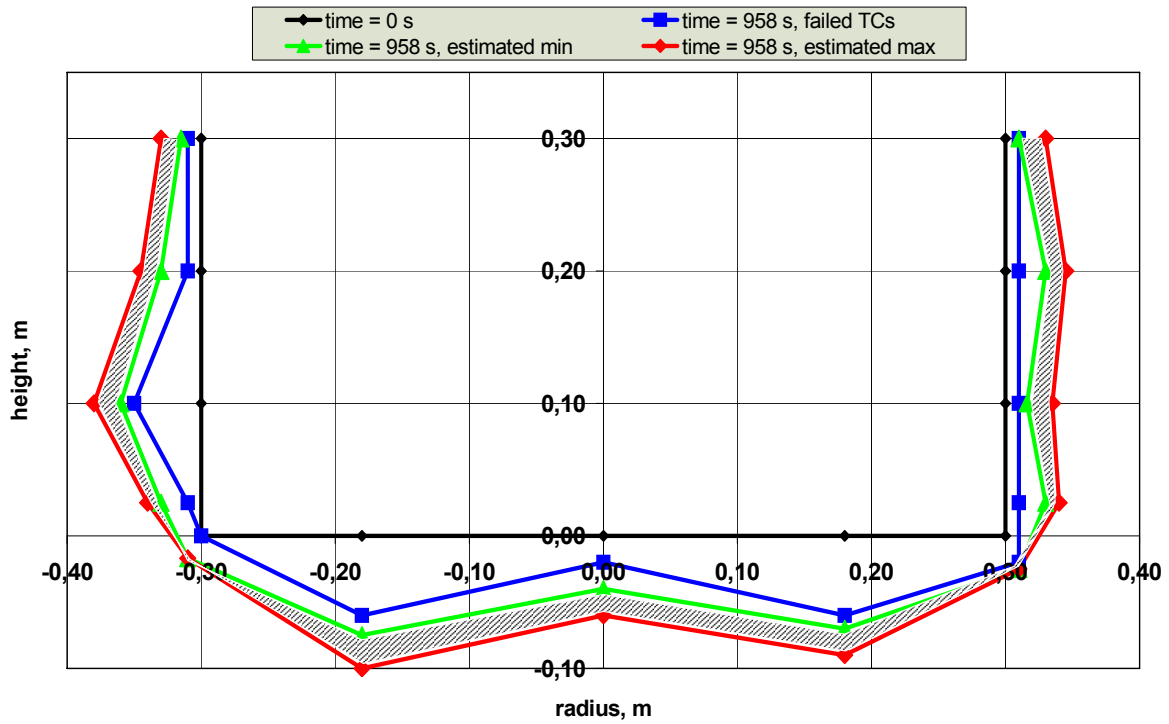
Figure 24: Initial and final cavity shape in the SW – NE plane. The shaded area gives the uncertainty range of the final cavity estimated from thermocouple measurements
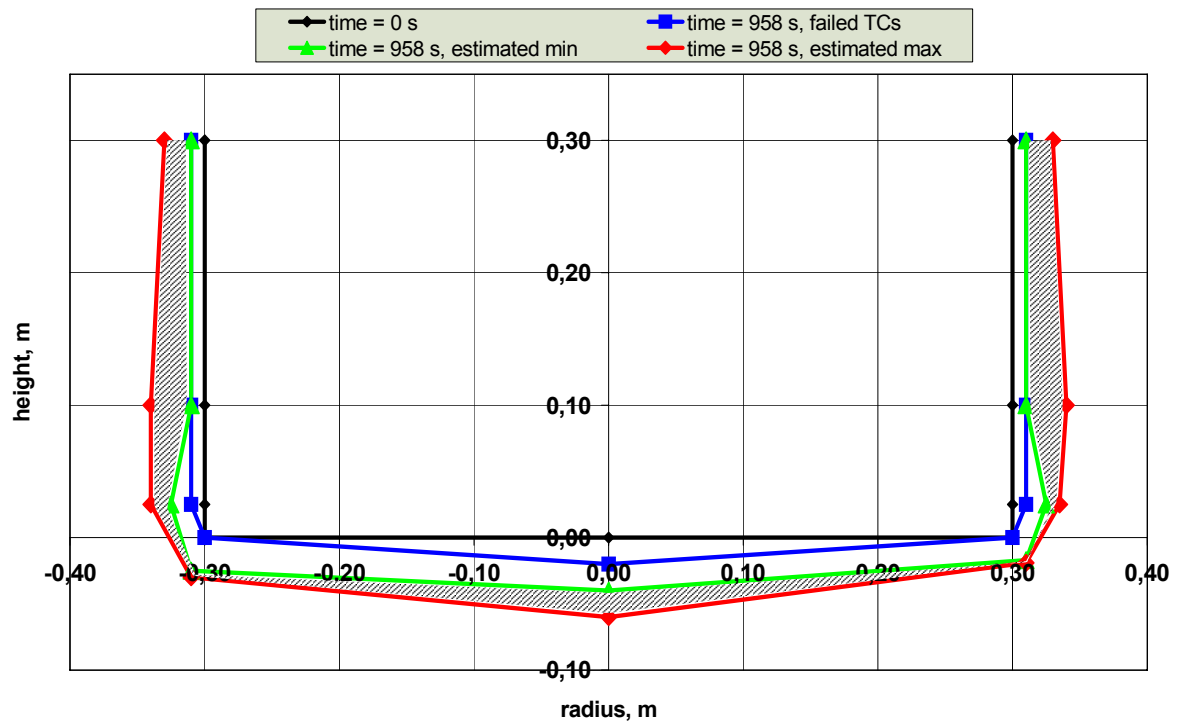
Figure 25: Initial and final cavity shape in the SE – NW plane. The shaded area gives the uncertainty range of the final cavity estimated from thermocouple measurements. Note that no thermocouples were present at the ± 0.18 m radius.

like a solid body, that is predominantly into the axial direction. Furthermore, the existence of a solid crust has important consequences for decay heat simulation by induction heating: Induction heating deposits the energy in a limited volume that is defined by the "skin effect" or the "penetration depth" of the induction field. The lack of macroscopic mixing by turbulent agitation of the steel melt after formation of a stable interface crust may therefore result in a non-homogeneous power distribution that may be concentrated near the bottom layer of the metal phase. This would enhance downward erosion too.

3.4.4 Gas release

The gases produced during MCCI are measured in the off-gas system, which connects the crucible with the open atmosphere.

The gas pressure in the hood is given in Figure 26, showing a practically constant atmospheric pressure. No oscillations were detected, as the off-gas line is sufficiently wide to release all gases to the atmosphere.
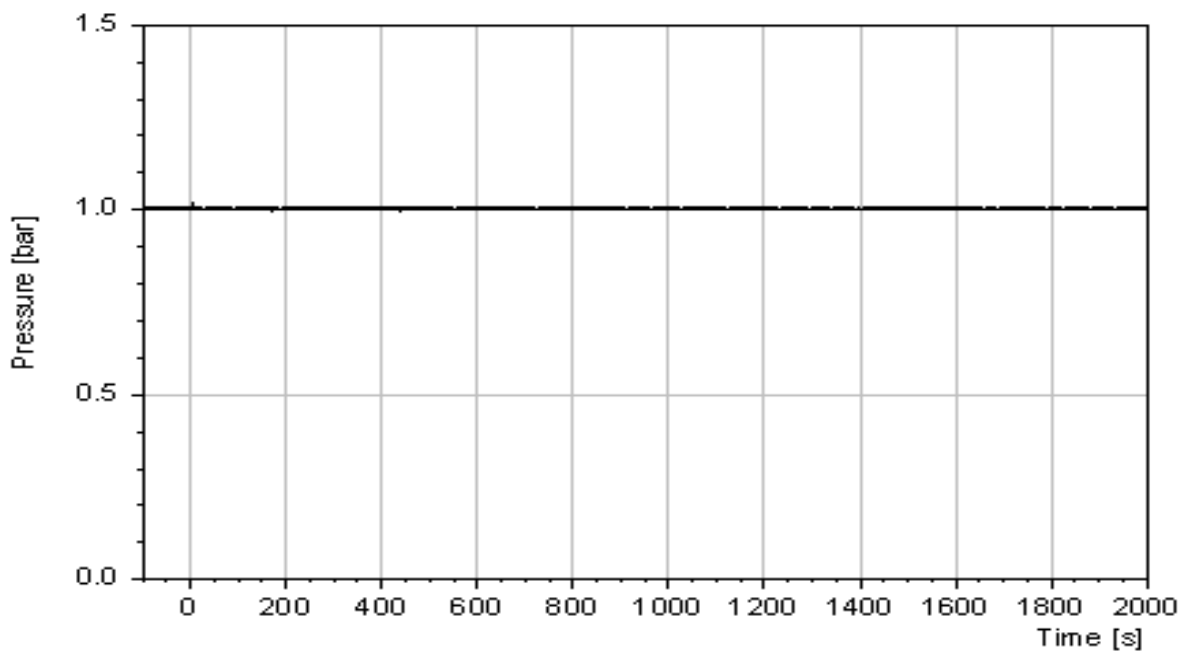
Figure 26: Gas pressure in the hood, showing atmospheric pressure

The off-gas temperature in the crucible hood, measured by the thermocouple positioned in the gas flow, is shown in Figure 27. The measured temperature is influenced by the gases released from the melt surface, by the addition of the argon cover gas, which has 20°C, and by the temperature of the inner liner of the crucible.
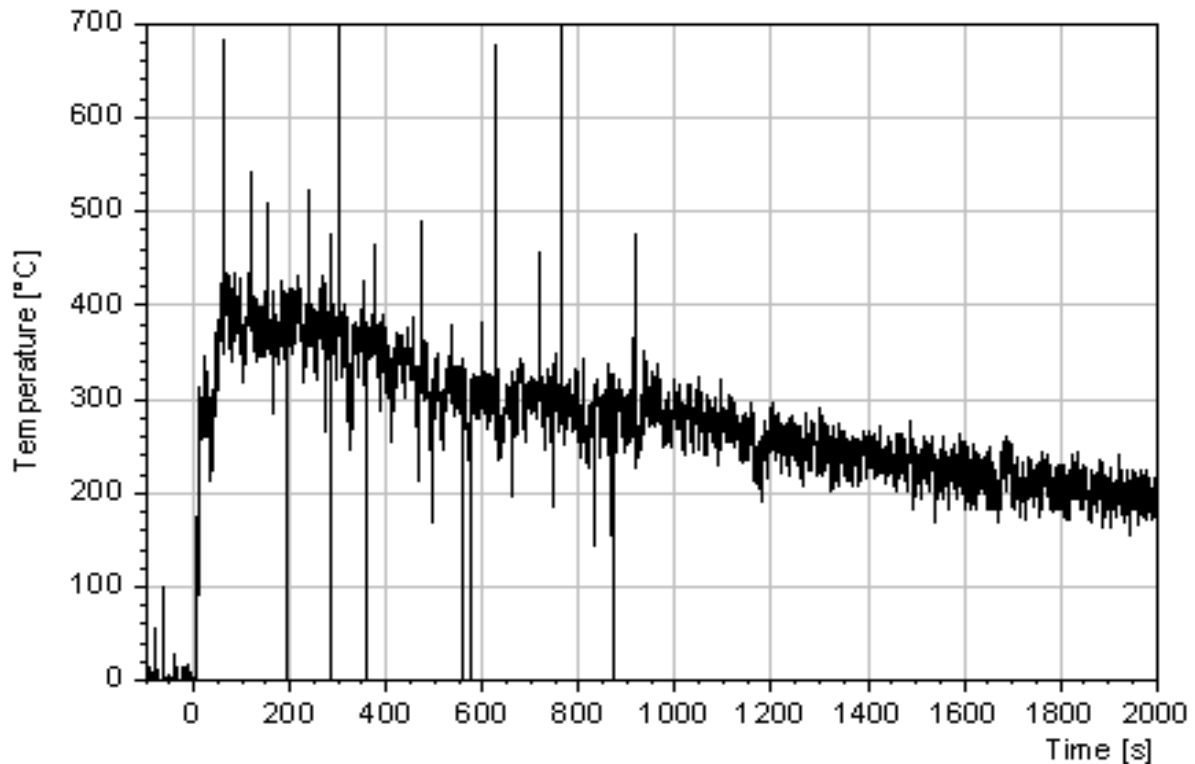
Figure 27: Gas temperature in the hood

When the melt is poured into the crucible the off-gas temperature increases to 400°C and then slowly reduces to 300°C at the end of the heating phase at 1000 s. Later on, during the long-term cool-down of the melt, the temperature decreases slowly: 200°C are reached after 2000 s, 130°C at 4000 s. Top flooding of the melt at 5000 s brings the off gas temperate to 100°C and below.

The off gas composition is measured online by the quadrupole mass spectrometer. The measurements were analysed by G. Schumacher [10] and the results are provided in the next two figures. Figure 28 shows the results for the gas release rates of the four most important gases (H_2, CH_4, CO, and CO_2). Not measured is the release of steam, as steam must be removed by condensation before the gas is fed to the mass spectrometer. The constant argon cover gas flow (see Annex C, Figure C14) is used as reference to determine the release rates of the gas species based on their measured concentration. The gas rates are referred to standard conditions, that is to 0°C and 1 bar pressure (22.4 l/s correspond to 1 mol/s). Because of significant response time of < 50 s for the gas measurement system, there is a delay between generation and registration of the gases.
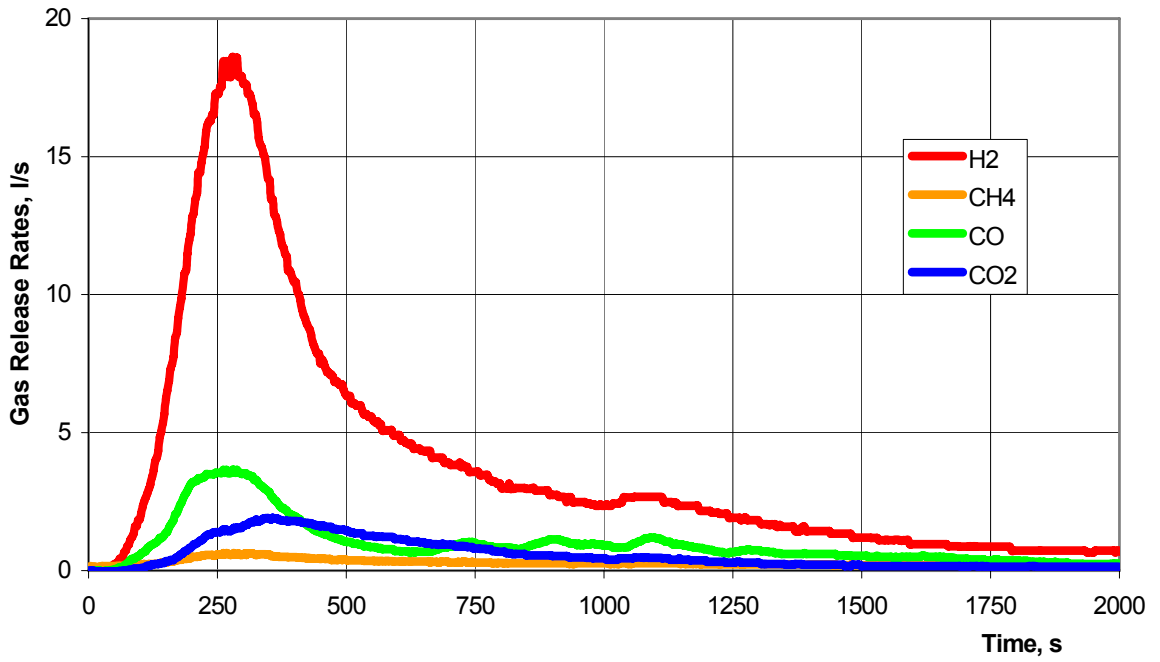
Figure 28: Gas release rates
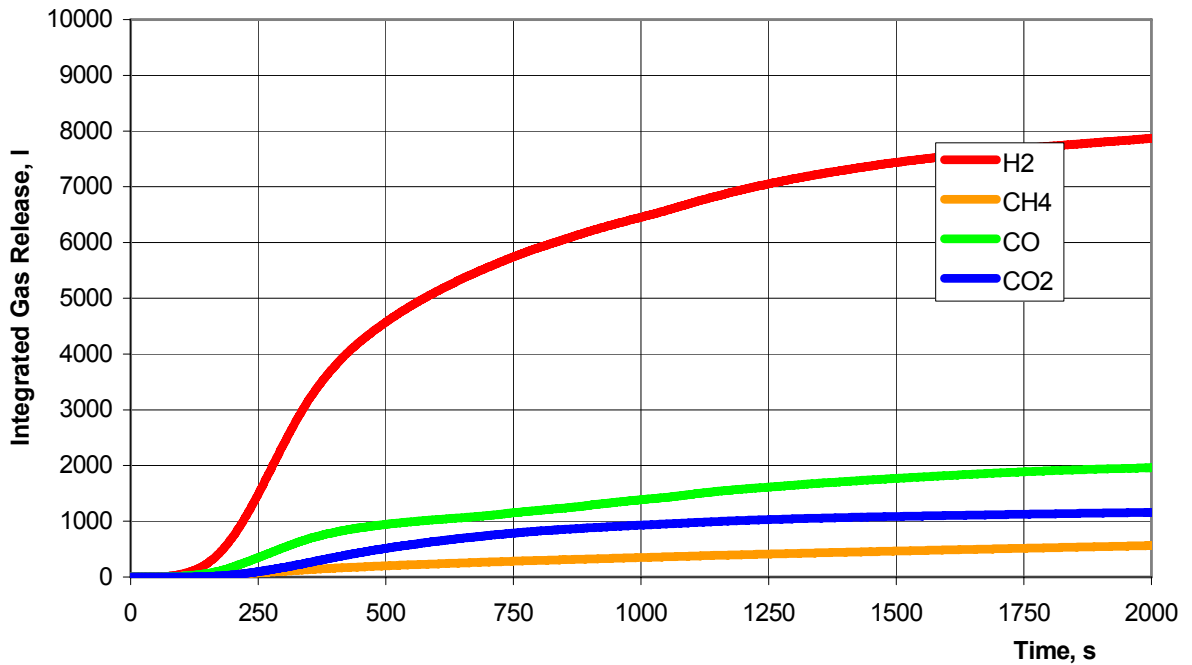
Figure 29: Integrated gas release

The dominant and most important gas is hydrogen, which is generated by the oxidation/reduction reaction of released steam with the metal phase, leading to hydrogen and iron oxide. Similarly, CO is reduced from CO_2. Both reactions are under present conditions not complete. The CO : CO_2 ratio is of the order 2:1. A similar ratio may be assumed for the ratio H_2 : H_2O during heating of the melt. Very little methane is released. As typical for siliceous concrete, CO release is 1/10 of the H_2 release, and results from carbonates that are present in small quantities in the concrete.

As gas release is directly coupled to the erosion rate, the time behaviour clearly replicates the concrete erosion described above. The fast drop of the initial high erosion and the slow, nearly constant erosion in the range 600 to 1000 s are clearly visible.

Figure 29 provides the integrated gas release as determined by the integration of the data given in Figure 28. During the first 2000 seconds of the test, approximately 8000 l of hydrogen were released.

3.4.5 Long-term melt behaviour and consequences of flooding

After the unexpected interruption of the induction heating system at 959 s, restart of heating by different actions was not successful. It was decided to observe cool-down of the melt without flooding the melt surface. Cool down occurred very slowly. The surface of the melt was free of crusts when the power was lost. Moderate gas flow from decomposing concrete through the surface of the melt persisted until 1560 s. During this period, first a thin viscous skin was formed, then some islands of floating crust appeared. Subsequently, the surface consisted of two different structures: (i) The bright, more and more viscous oxide melt and (ii) pieces of dark, floating crust. This corresponds to the situation which is illustrated by the temperature history in Figure 16 after 1000 s: (i) The hotter melt, temperature of 1300°C slowly decreasing, and (ii) the colder crust generated since 1200 s which was considerably colder and showed a faster temperature reduction. The fraction of the crust covering the central surface gradually increased and covered some 50 % of the surface at 2400 s and some 70 % at 3600 s in Figure 30 a and b, respectively. The ongoing temperature reduction of the oxide "melt" e.g. below 1000°C at 2200 s indicated that solidification occurred in the hot oxide, but evidently with a slower temperature drop than the dark crust. Obviously, the islands of dark crust acted like shields for thermal radiation. At 4800 s the dark crust covered the surface nearly completely, but hotter oxide was still visible through gaps.
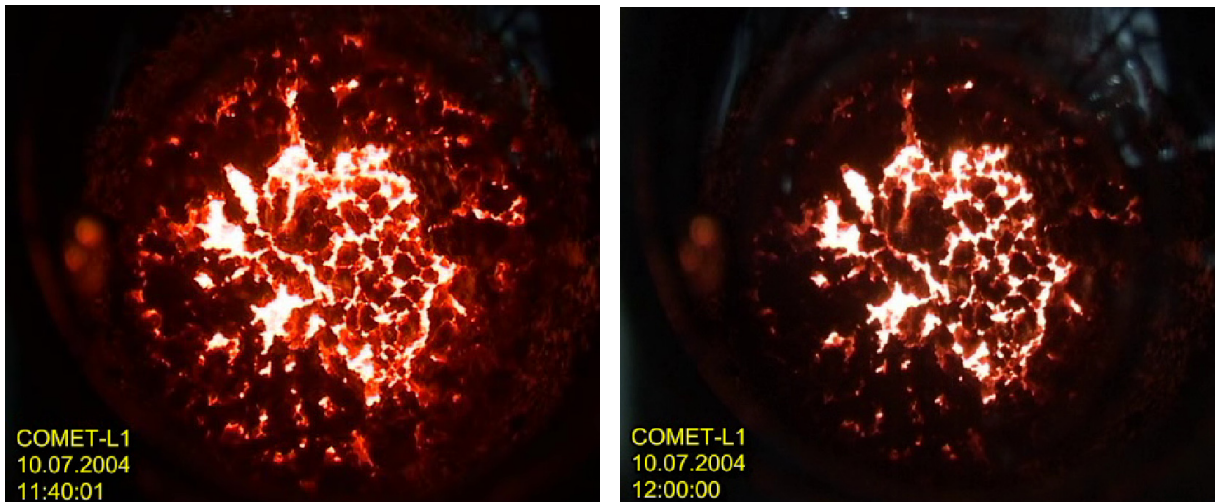
Figure 30: Surface of the melt during solidification: left – after 2400 s; right – after 3600 s

Three of the four thermocouples failed during the early test phase by contact with the metal melt, but formed new junctions near the interface, and delivered reliable temperatures within a small band of uncertainties. The maximum temperature measured at 1000 s was 1300°C, which agreed with the oxide temperature that was measured by the infrared camera at the oxide surface. These temperatures decreased to some 1100°C (steel is solidified) at 3000 s, when the oxide temperature near the upper surface had already reduced to some 950°C.
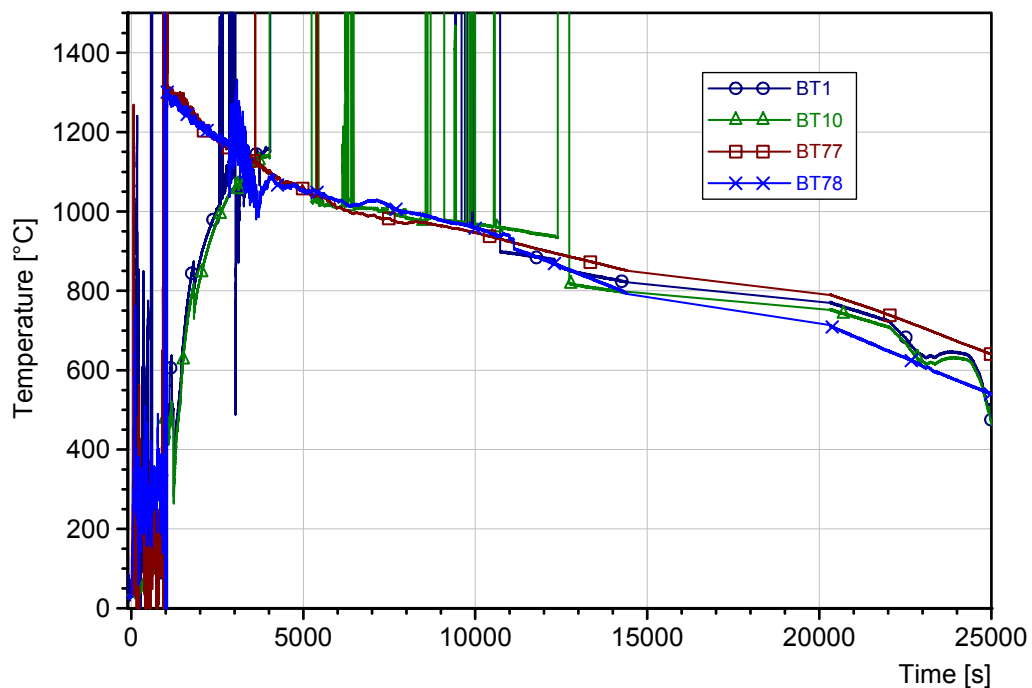
Figure 31: Temperatures measured near the inner surface of the concrete cavity at the bottom. Sharp spikes are due to failure and reformation of the thermocouple junction.

The higher temperature in the lower crucible seems plausible because of the poor thermal conductivity of the hot concrete. Nevertheless it is remarkable that at this time the temperature registered near the outer surface of the lower crucible was ~30°C only, although no cooling took place. Simultaneously, the temperature in the porous sublayer beneath the concrete crucible was 20 to 30°C only.

Shortly after 3000 s the operator activated water supply with 0.85 litres/s to the porous layer below the crucible, and at 3700 s to the outer sidewall of the concrete crucible, with the intention to keep the bottom part of the crucible cold and prevent the induction coil from damage if the crucible would fail. Figure 32 shows the water supply to the bottom and sidewalls of the crucible, and Figure 33 gives the resulting water level at the sidewall of the crucible.

At 4800 s, water supply was reactivated, so that the solidified surface of the melt was quenched and covered with water at 5200 s. A boiling water overlayer of some 20 cm was established at 5500 s. Figure 31 shows no influence of surface quenching on the temperature at the lower bottom of the melt. At 9500 s, water supply from the showerhead was activated and the water level above the melt surface was maintained. To remove the energy from the crucible, the coolant water was drained and fresh water was supplied several times. These procedures did not change the geometrical structure of melt and crucible.

Although the solidified surface of the melt and the concrete crucible were in direct contact with water, the energy removal form the hot, mostly solidified "melt" was very low as limited by heat conduction. After 25,000 s, which is after 7 hours, the lower concrete interface has still temperatures near 600°C (Figure 31), which indicates that major water ingression to the bulk of the melt did not occur. Further cool-down of the melt was allowed over 40 hours.
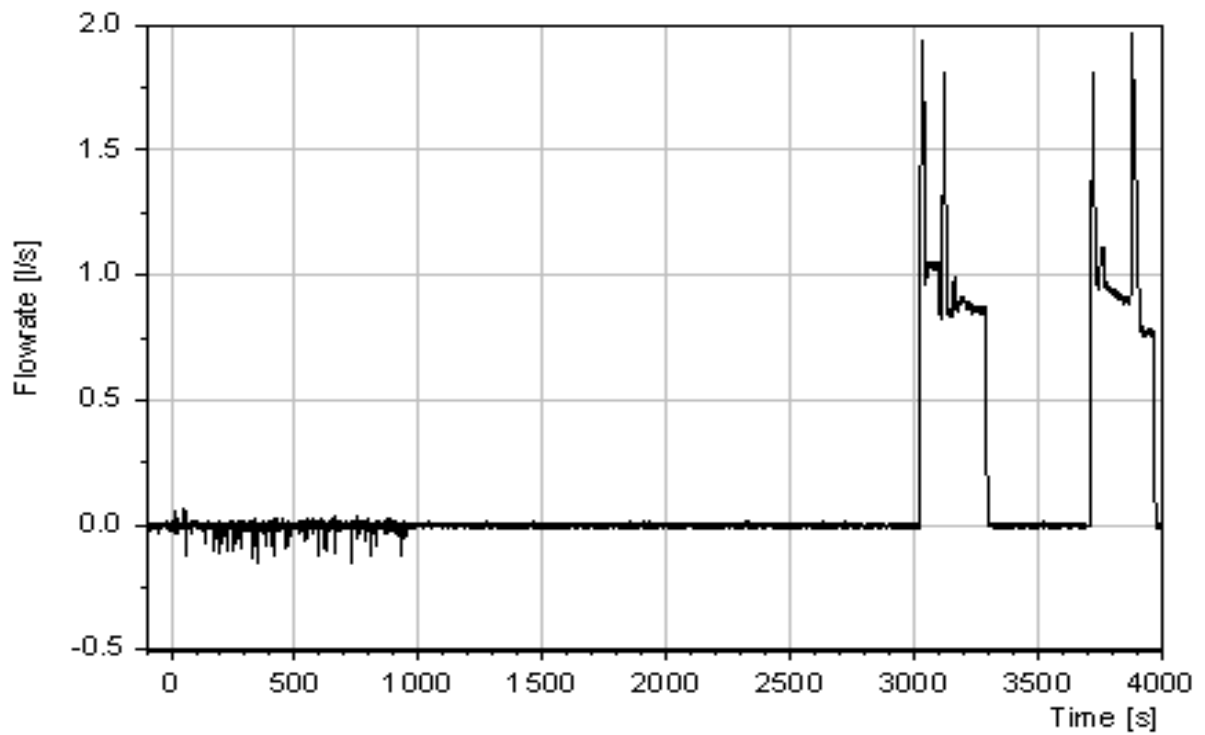
Figure 32: Water flow rate to the bottom and to the sidewalls (WF 16)
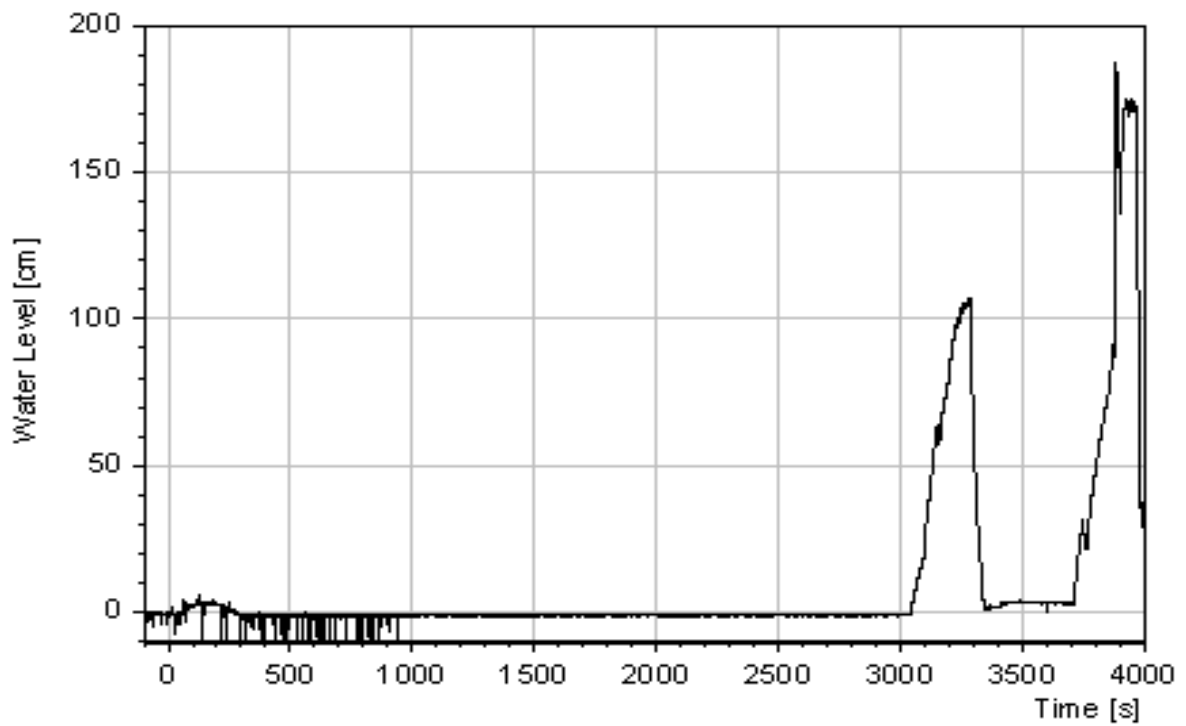
Figure 33: Water level in gap at the sidewall (CL1)

3.4.6   Post test analyses

Two days after the test, disassembly of the facility was started to document the status of the cavity and the debris configuration. A first view from above into the open crucible enclosed by the outer protection tube is shown in Figure 34 and Figure 35. This view corresponds to the schematic drawing of Figure 2 after removal of the crucible hood.
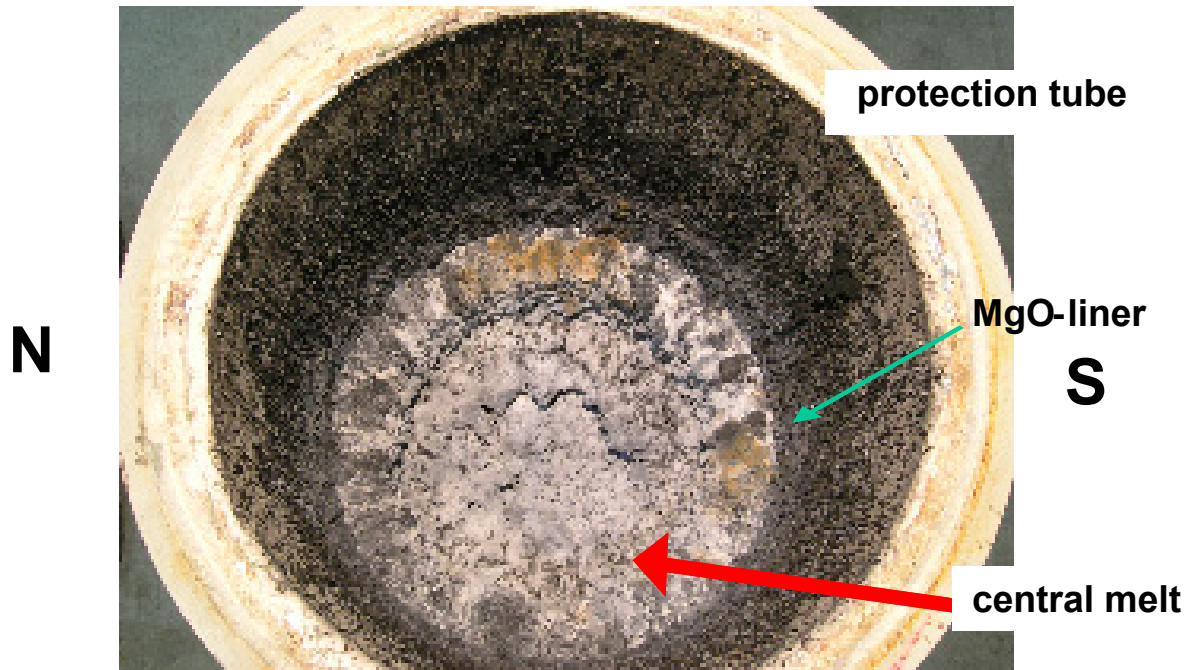
Figure 34: View from above into the open facility after the experiment

Figure 35: Closer view from above into the open facility after the experiment

Figure 36 shows the upper melt surface after disassembly of the test rig and removal of the surrounding protection tube

Figure 36: View of the melt surface after the test
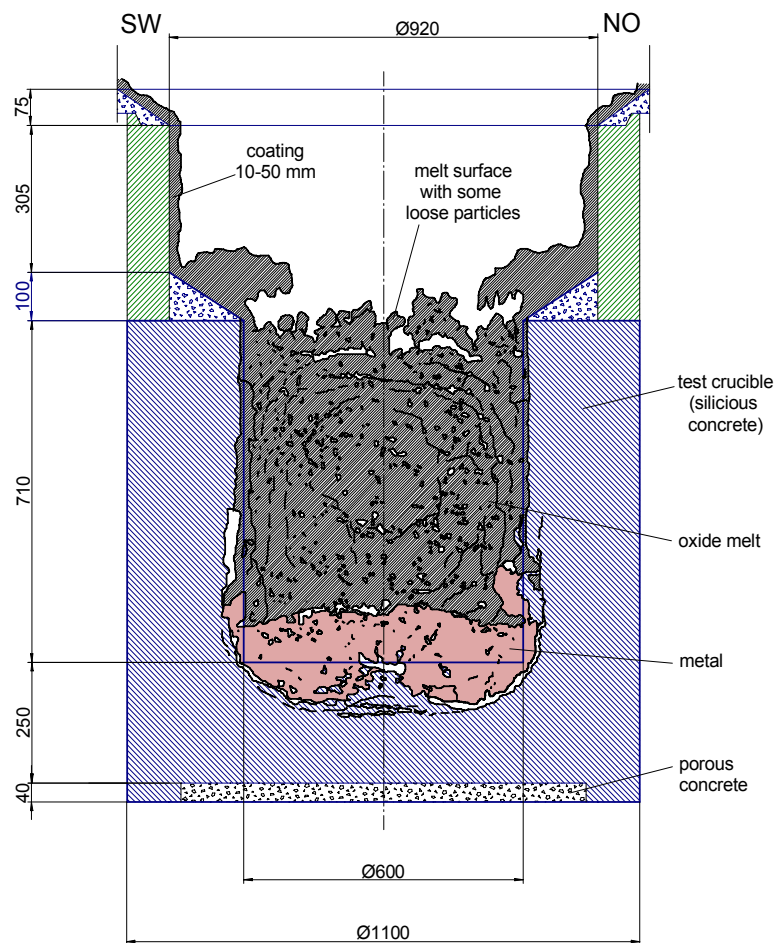
Figure 37: Contour of the melt after the test

The outer ring in Figure 36 from which some solidified oxide melt material was removed is the MgO-ring that is located on top of the concrete crucible. The level of the central, very rough surface of the solidified melt corresponds to the upper edge of the concrete crucible. The artist's view of the cross section of the crucible, represented in Figure 37, shows the different crusts and their structure. The upper part of this figure gives a good illustration of the decline of the melt surface when the void in the oxide melt reduced during the first few hundred seconds from the upper edge of the MgO ring down to the upper edge of the concrete crucible, as the initial high gas release reduced during the test. The surface of the solidified melt is very rough and is covered with some loose particles that fell down from the sidewalls. This figure also includes the sectioned crucible which is described in further detail below.

By a mass balance after the experiment it was confirmed that the oxide mass that was retained in the slag wagon was only 33 kg. Consequently, nearly all melt generated by the thermite reaction, was poured into the test crucible. From the oxide mass some 95 kg of the melt was splashed to the upper part of the protection tube during the initial phase of intense interaction. 168 kg are frozen on the MgO ring in the early phase of MCCI. Consequently, the residual mass of initial oxide in the concrete crucible is 204 kg, augmented by the melted concrete.

The crucible was sectioned several months after the test along the main instrumentation plane SW-NE, and the pictures became available April 2005. They are presented in Figure 38 and Figure 39. Figure 38 is the view of the two sectioned half cylinders The lower cavity is filled with the iron regulus of the melt, overlaid by the oxide layer. Both layers show a low porosity, most of the porosities are closed voids, and do not allow water ingression. This explains the very slow reduction in temperature after end of heating. A closer view of the oxide phase shows very fine cracks that are allocated in the form if circles (or spheres) around the centre of the oxide. The typical distance of the cracks is 2 to 5 cm. The origin of these cracks is with high probability the shrinking of the oxide melt during solidification. This means, that these cracks would not exist, if the bulk of the melt would remain at high temperatures because of the pertinent release of decay heat in a real corium melt.

The oxide melt contains a significant amount of unmelted silica gavels. These are the consequence of low heat fluxes to the concrete surface. Under these conditions, the 800 to 900°C isotherms separate from the melting front and extend into the deeper concrete. This gives rise to decomposition of the cement matrix in front of the melt front, the heated concrete loses its mechanical strength, and the aggregates may be transferred into the melt before being melted.

Figure 38: Eroded concrete crucible sectioned in direction NE-SW, front and rear semi cylinder.

SW-NE

428078

NE-SW

428080
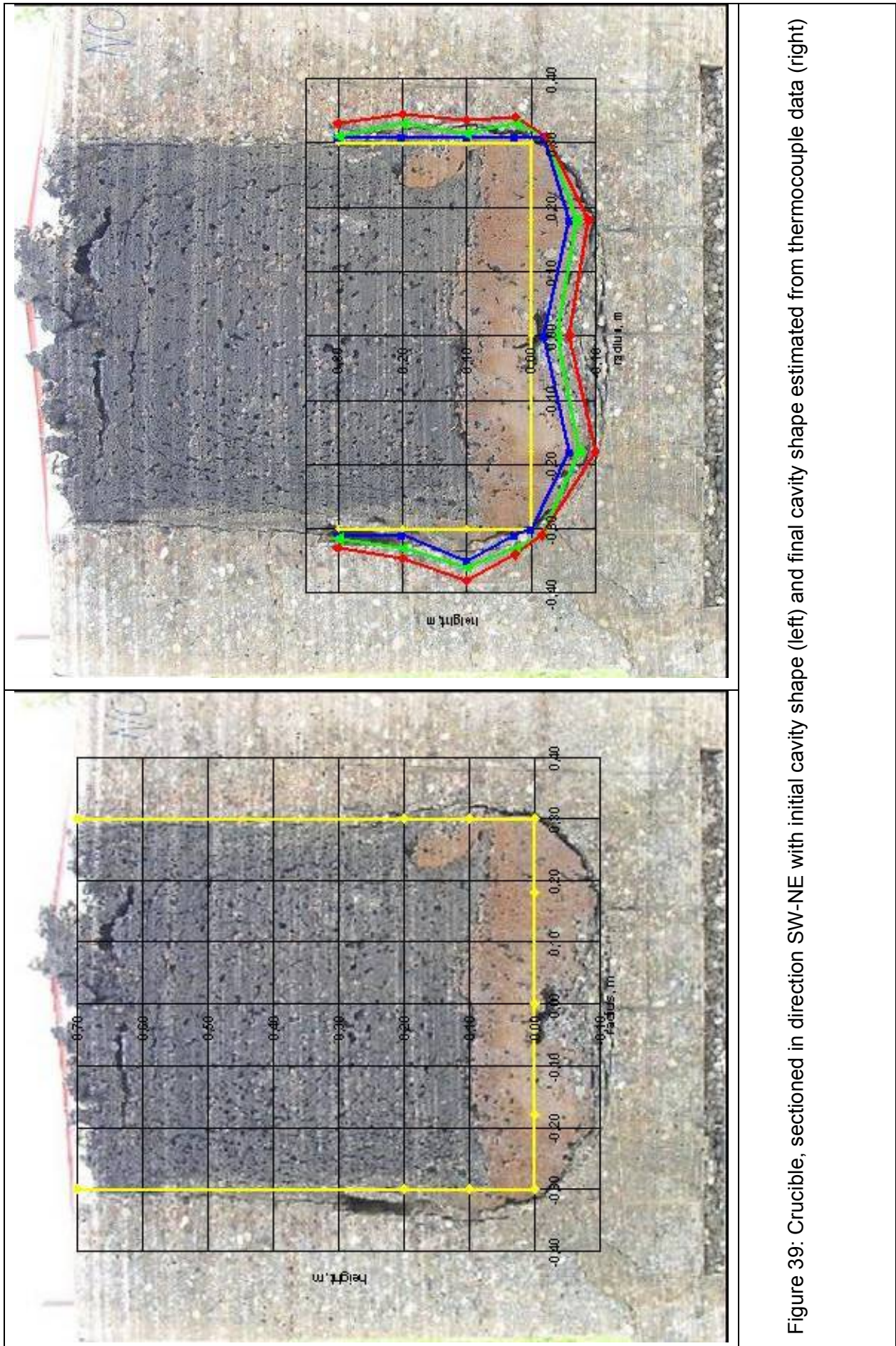
Figure 39: Crucible, sectioned in direction SW-NE with initial cavity shape (left) and final cavity shape estimated from thermocouple data (right)

The interface between metallic and oxidic regulus is quite even with the exception of the outer boundary where some metal extends into the oxide.

The metallic regulus is symmetric with respect to the centreline, but shows a remarkable feature. Near the centreline, the metallic melt did not erode the bottom concrete cavity but solidified very close to the initial cavity level. In contrast, the maximum of downward erosion occurred at the 18 to 20 cm radius where some 10 cm downward erosion occurred. The reason for this behaviour is seen in the non homogeneous distribution of the induction heating which is a minimum near the centreline of the induction coil, a consequence of the electromagnetic field. As turbulent mixing in this experiment after onset of crust formation was not sufficient to generate a homogeneously mixed metallic melt, the erosion near the centreline is not prototypic. This process was already mentioned in section 3.4.3. The residual concrete in this area was destroyed by the high temperature, in that the cement matrix was destroyed, and the aggregates persisted without being melted. This is the process described above with respect to the source of the silica gravels in the oxide melt.

Figure 39 illustrates the erosion that occurred during the test. The left figure gives the contour of the initial cavity in yellow, the right figure shows in addition the end of erosion as determined by the failed thermocouples (blue), and the green and red lines as the minimum and maximum estimated erosions by extrapolation of the temperature profiles, as extracted by Figure 24. The minimum estimation (green), is indeed very close to the final cavity. An exception is the centreline where erosion is overpredicted, as in this area the thermocouple BT1 failed near 1200°C by chemical attack of the heated concrete, but was not reached by the melt front.

The cavity erosion by the oxide melt is virtually zero in the upper cavity. The lower 30 cm of the sidewalls show more pronounced radial erosion, maximum erosion 4 cm, which is predominantly due to the attack of the metal melt. In contrast, downward erosion by the metal melt extends to some 10 cm with the maximum near the 20 cm radius. Although the uneven downward melt front is partly due to the inhomogeneous decay heat distribution after formation of a stable metallic interfacial crust, the more pronounced downward than sideward erosion seems to be imminent to the erosion by the metal melt also for low heat fluxes. This is in agreement with the former BETA experiments V 3.1 to 3.3 at low induction power, that showed similar erosion rates, although induction heating was by means of a cylindrical induction coil, that generated an electromagnetic field which differs from the horizontal, even induction coil. It is therefore concluded, that in the former and present experiments, induction heating in simulation of the nuclear decay heat does not significantly change the ratios of downward and

sideward concrete erosion. However, more reliable data are highly desired in a future experiment with longer experimental time.

Another interesting subject is the minor erosion of the bottom corner of the cavity, which shows virtually no erosion for the limited experimental time. Slower erosion in a corner as compared to an even surface is largely due to geometrical reasons, as explained in section 3.4.3.

4 Conclusions from the experimental results

The results of this experiment are summarized as follows:

- The experiment COMET-L1 investigates the interaction of a melt with siliceous concrete in a large cylindrical cavity. Internal heat generation corresponds to the power density of the decay heat some hours after start of concrete erosion. The experiment aims to identify and to quantify important long-term processes in the accident situation, when the steel phase of the corium melt is layered beneath the oxide melt.

- 460 kg steel melt plus 927 kg less dense oxide melt were poured into the concrete crucible, leading to an initial collapsed melt height of 780 mm.

- The simulated decay heat that was deposited in the steel melt was ~25 % lower than planned, but covers an interesting range to extend previous experiments and current computer models. Unfortunately, decay heat simulation ended after 960 s because of failure of a power control board. Therefore, the concrete erosion observed in this experiment is less pronounced than expected.

- In the early phase of the test, measurements show fast decrease of the melt overheat and reduction of the initially high concrete erosion rate. Concerning concrete erosion by the lower metal phase, initial erosion into axial and lateral direction is similar with erosion rates of ~ 0.15 mm/s. For the lateral erosion by the oxide phase, the overall erosion is relatively small, so that no detailed erosion rates of the oxide can be derived. This is due to the fact that for the given conditions the temperature of the oxide melt is close to the decomposition temperature of the concrete.

- The early phase of MCCI was accompanied with high gas production (mainly hydrogen) and intense agitation of the melt.

- During the subsequent phase of equilibrium between decay heat and removed heat, slow concrete erosion and slow gas release are interrupted by several phases of more intense gas eruptions and melt agitation. Consequently, surface crusts on top of the oxide may grow and are re-melted. For the lower metal phase, there are indications for formation of a crust at the concrete interface. Erosion is then propagating mainly into the axial direction, as the encrusted metal melt tends to move like a solid body. In conclusion, the melt shows anisotropic erosion, in that downward erosion is more pronounced than lateral erosion.

- After end of heating the melt cools down very slowly, as detected by temperature measurements of the upper surface of the melt and at the lower inner interface of the concrete crucible. Late surface flooding that was initiated after formation of a stable surface crust has little effect to improve heat removal from the bulk of the (mostly solidified) melt. The sectioned crucible contains dense oxidic and metallic melt layers with some closed porosity, to which water ingression did not occur.

The observed phenomena and measurements shall be used to validate models and computer codes. Comparison with former BETA tests [11] in the low power range, such as BETA-V2.1, shows the following tendencies: The initial fast drop of the temperature of the layered melts, which is due to the high initial erosion rate, is confirmed. Qualitative agreement is also found in the subsequent phase of the test after some 150 s, in that the axial erosion rate by the metal melt is more pronounced than the lateral erosion rate. Comparison with high power experiments shows, however, that lateral erosion through the metal phase becomes more important when the heating power is reduced. The low power density in the present test favours the existence of metal crusts, which may have a strong influence on the shape of the cavity. The short duration of the present test is however not sufficient to quantify these phenomena. Therefore, further experiments and considerations are required to understand the formation and re-melting of crusts at the concrete interface. A further experiment with low internal decay power will indeed be performed in the framework of the LACOMERA program to extend the present experiment. Additional tests with pure oxide melts [2] are needed to complete our understanding on corium erosion.

Acknowledgements

References

[1]   A. Miassoedov et al. Large Scale Experiments on Core Degradation, Melt Retention and Coolability (LACOMERA). FISA-2003: EU Research in Reactor Safety, Luxembourg, L, November 10-13, 2003, Preproc. p. 239-244.

[2]   M. T. Farmer, S. Lomperski, S. Basu, Results of Reactor Materials Experiments Investigating 2-d Core-Concrete Interaction and Debris Coolability, Proc. ICAPP '04, Pittsburgh, PA, June 13-17, 2004, Madison, Wis.: Omnipress, Paper 4102.

[3]   H. Alsmeyer, T. Cron, G. Messemer, W. Haefner, ECOKATS-2: A large scale experiment on melt spreading and subsequent cooling by top flooding, Proc. ICAPP '04, Pittsburgh, PA, June 13-17, 2004, Madison, Wis.: Omnipress, Paper 4134.

[4]   I. Ivanov, B. Kalchev, Severe accident simulation of a long term corium-concrete interaction, water/melt mixing by the cooling and quantification of the erosion and decomposing of a concrete applicable to VVER plants, Proposal for LACOMERA experiment, December 2003.

[5]   M. Cranga, IRSN – France, COMET dry 2D MCCI experiment, Proposal for LACOMERA experiment, December 2003.

[6]   H. Alsmeyer, T. Cron et al., Melt cooling by bottom folding: The experiment CometPC-H3; Ex-vessel core melt stabilization research; SAM-ECOSTAR-D44; January 2003.

[7]   H. Alsmeyer, Internal note, July 2004.

[8]   T. Cron, Internal note, June 2004.

[9]   T. Cron, G. Messemer, B. Remy, Internal note, July 2004.

[10]   G. Schumacher, Internal note, August 2004.

[11]   H. Alsmeyer, 1987, BETA experiments in verification of the WECHSL code: Experimental results on the melt-concrete interaction, Nucl. Eng. and Design, 103,115-125.

Appendices

Appendix A: Instrumentation Plan for COMET-L1

A.1 AUFBAU DES VERSUCHSTIEGELS

Mit dem Experiment Comet-L1 wird die Betonerosion einer induktiv beheizten Thermitschmelze und ihre Kühlbarkeit von oben untersucht. Nach dem Eingießen beginnt die Erosion der Schmelze im Beton und nach einem senkrechten Erosionsfortschritt von ca. 15 cm wird von oben Wasser auf die Schmelze gegossen. Für das Experiment wurde ein spezieller dickwandiger Betontiegel hergestellt. Abbildung 1 zeigt die Anordnung des Versuchstiegels in der COMET-Anlage. Der Betontiegel hat einen Außen Ø von 1100 mm und ist 1000 mm hoch. Der Innenraum zur Aufnahme der Schmelze hat einen Ø von 600 mm und ist 710 mm tief. Der Tiegelboden ist 290 mm dick und die Tiegelwand ist 250 mm breit. Auf der Unterseite des Tiegelbodens ist eine poröse Betonschicht eingebaut (920 mm Ø, 40 mm hoch), durch die die Schmelze jederzeit nach dem Comet-Konzept von unten gekühlt werden kann.

A.2 KOORDINATEN UND INSTRUMENTIERUNGSEBENEN

Zur Registrierung der Schmelzentemperatur und zur Überwachung des Erosionsfortschrittes sind 92 Thermoelemente in den Betontiegel eingebaut. Abbildung 2 zeigt den Versuchstiegel von oben mit den beiden vertikalen Instrumentierungsebenen, die mit Thermoelementen versehen sind. Die Primärebene verläuft in Richtung 45°-225°, die Sekundärebene 90° dazu in Richtung 135°-315°. Aus der Abb. ist die radiale Position der TE zu entnehmen. Zur Messung der Schmelzentemperatur sind in einer um 8° gedrehten dritten Ebene 4 W/Re-TE vorgesehen.

Durch den rotationssymmetrischen Aufbau der Versuchsanordnung ist es zweckmäßig für Positionsangaben Zylinderkoordinaten (r, φ, z) zu benutzen. Die Oberkante des Betonbodens ist die Bezugsebene (z = 0) mit dem Koordinatenursprung in der Tiegelmitte. Die Winkellage 0° liegt im Osten (Hallentor). In den Abbildungen 3 und 4 sind die Positionen der TE als Schnitte durch die beiden Instrumentierungsebenen dargestellt. Über die Tiegelhöhe existieren mehrere horizontale Instrumentierungsebenen:

Instrumentierungsebene	1	untere Hälfte der Oxidschmelze	z = 300 mm
Instrumentierungsebene	2	oberes Niveau der Metallschmelze	z = 200 mm
Instrumentierungsebene	3	Mitte der Metallschmelze	z = 100 mm
Instrumentierungsebene	4	unteres Niveau der Metallschmelze	z = 25 mm
Instrumentierungsebene	5	20 mm tief im Betonboden	z = -20 mm
Instrumentierungsebene	6	60 mm tief im Betonboden	z = -60 mm
Instrumentierungsebene	7	100 mm tief im Betonboden	z = -100 mm
Instrumentierungsebene	8	140 mm tief im Betonboden	z = -140 mm
Instrumentierungsebene	9	180 mm tief im Betonboden	z = -180 mm
Instrumentierungsebene	10	220 mm tief im Betonboden	z = -220 mm

crucible hood with
off-gas line

tie rod

⌀ 1143

MgO - liner

composite
protection tube

⌀ 920

⌀ 1100

porous insulation

⌀ 600

concrete crucible

coolant water
on demand

instrumentation
port

sealing foil

porous concrete

protect plate

induction coil

transport car
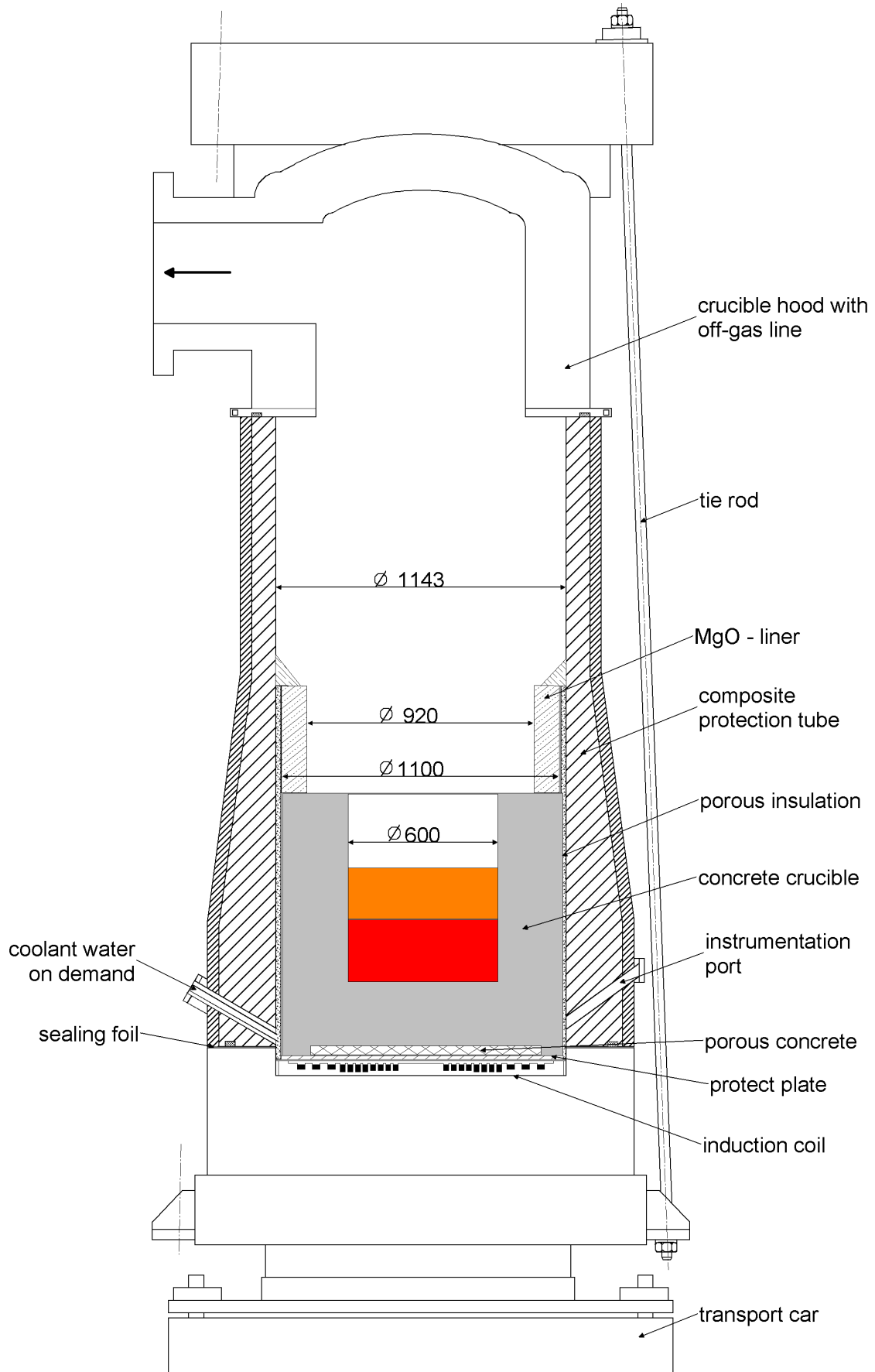
Abb. 1: **Comet-L1: Experiment zur Betonerosion mit Kühlung von oben**
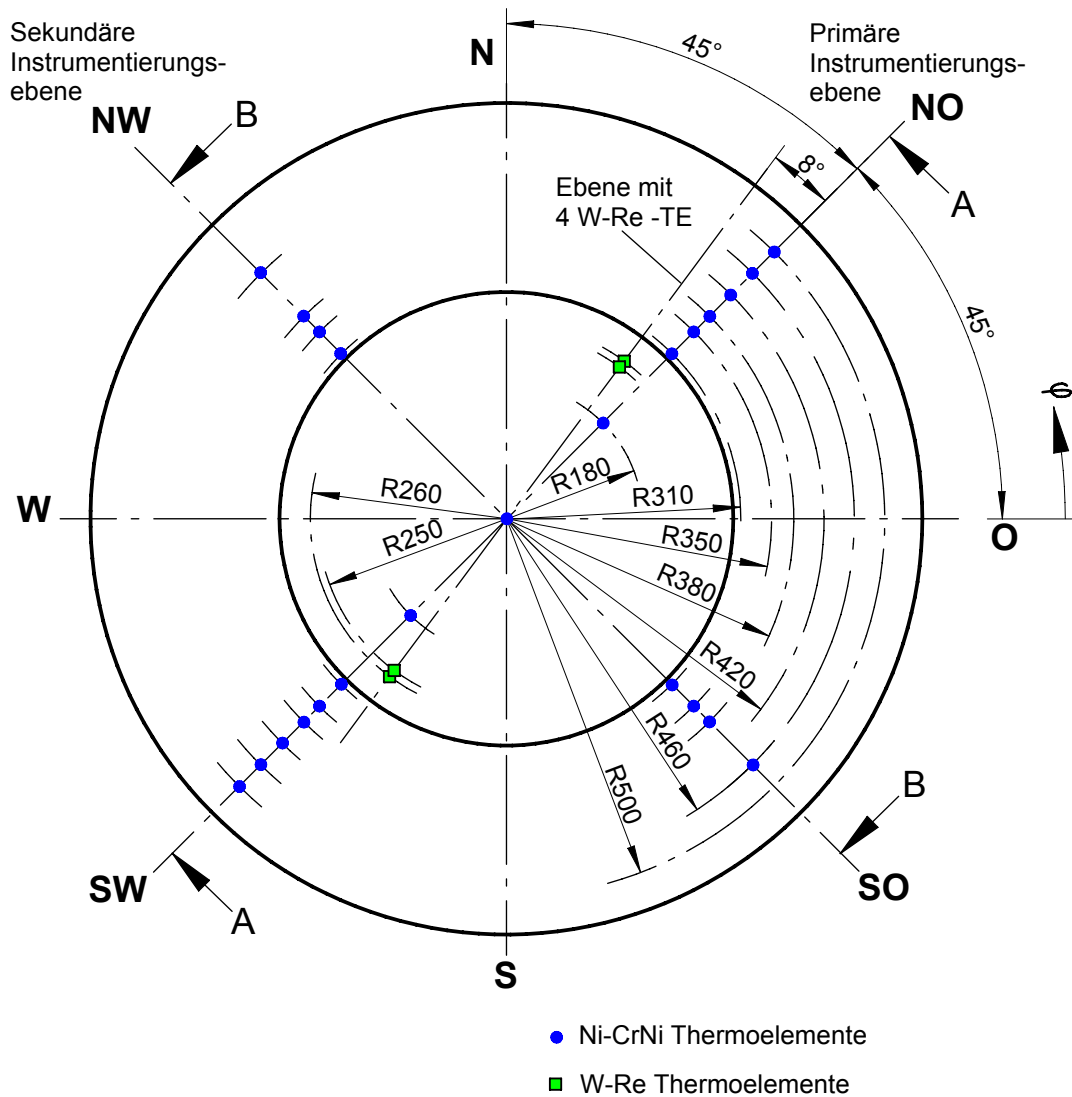
Abb. 2: Betontiegel von oben mit den Positionen der Thermoelemente

A.3 INSTRUMENTIERUNG

Durch die begrenzte Anzahl von Messkanälen ist die Instrumentierung in der Primärebene dichter als in der Sekundärebene. Die Messpositionen innerhalb einer Ebene sind symmetrisch zur Rotationsachse. Nach unten nimmt die Instrumentierungsdichte zu. Außer den 4 W/Re-Thermoelementen in der Schmelze sind alle im Betontiegel eingesetzten Thermoelemente vom Typ Ni/CrNi (Typ K). Ausgehend von ihrer Messposition verlaufen die Thermoelemente im Beton senkrecht nach unten und werden dann unterhalb der Messebenen seitlich aus dem Tiegel herausgeführt.

Wie aus den Abbildungen 3 und 4 zu ersehen sind zur Sicherheit gegen Durchschmelzen im unteren Rand und im Boden des Betontiegels mehrere Lichtleiterschleifen eingebaut, die bei Zerstörung durch Schmelze eine Induktorabschaltung auslösen und so eine weitere Erosion verhindern sollen. Gleichzeitig zur Induktorabschaltung wird die Kühlung der Schmelze über die untere poröse Schicht gestartet. Dieser Kühlvorgang kann bei Notwendigkeit jederzeit von Hand ausgelöst werden.

In Abb. 3 sind auch die W/Re-Thermoelemente BT 91, BT 92 und BT 93, BT 94 zur Messung der Schmelzentemperatur eingezeichnet. In Realität befinden sie sich in einer anderen Ebene (siehe Abb. 2), um 8° zur Zeichnungsebene gedreht. BT 92 und BT 94 sitzen 350 mm über dem Tiegelboden bei r = 250 mm. BT 91 und BT 93 befinden sich 260 mm über dem Tiegelboden bei r = 260 mm. Die oberen W/Re-Elemente dienen zur Messung der Oxidtemperatur, die unteren zur Messung der Metalltemperatur.
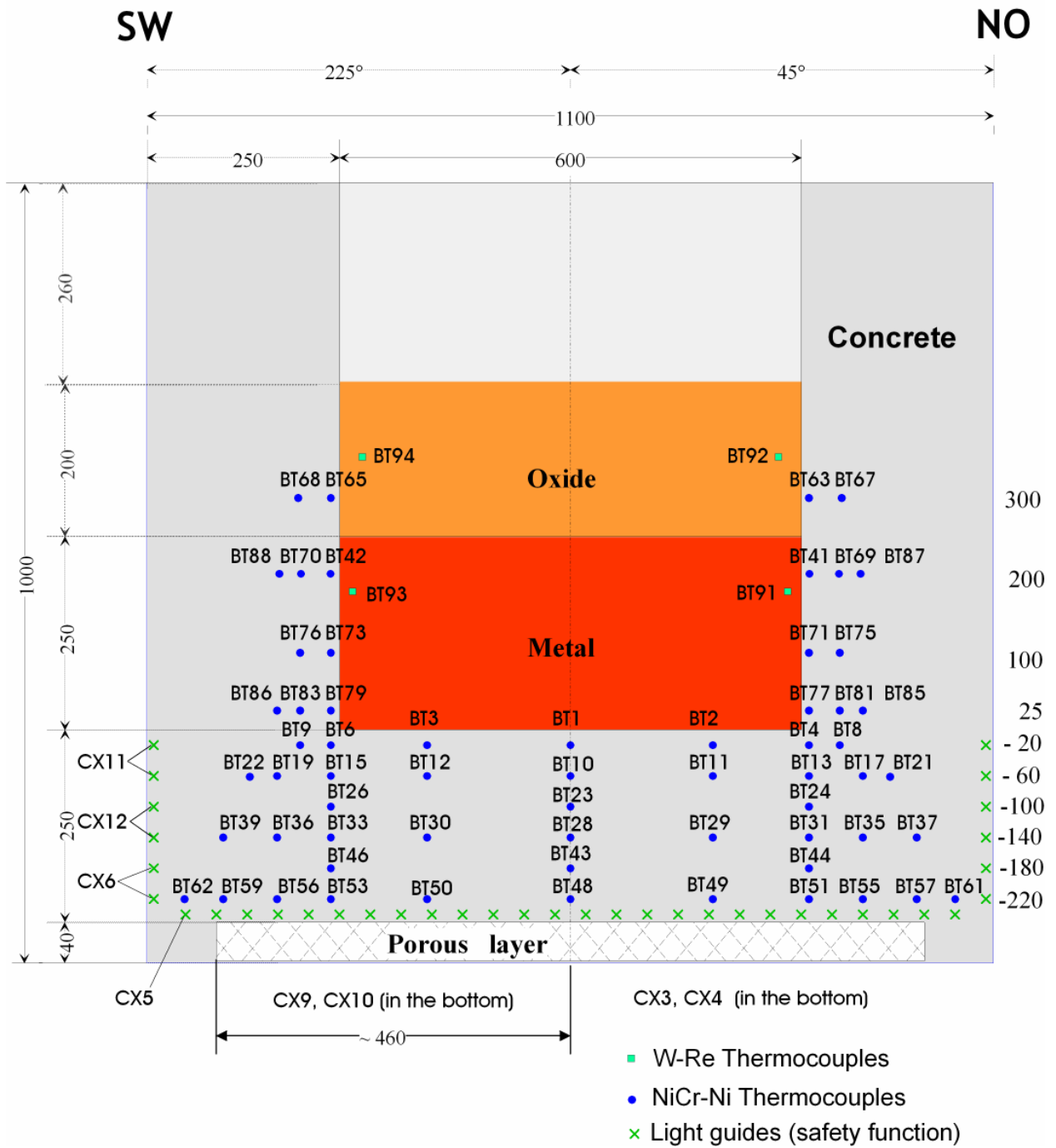
Abb. 3: **Anordnung der Thermoelemente in der Primärebene** (Schnitt A-A (SW-NO) unter 45° durch den Betontiegel, siehe Abb. 2)
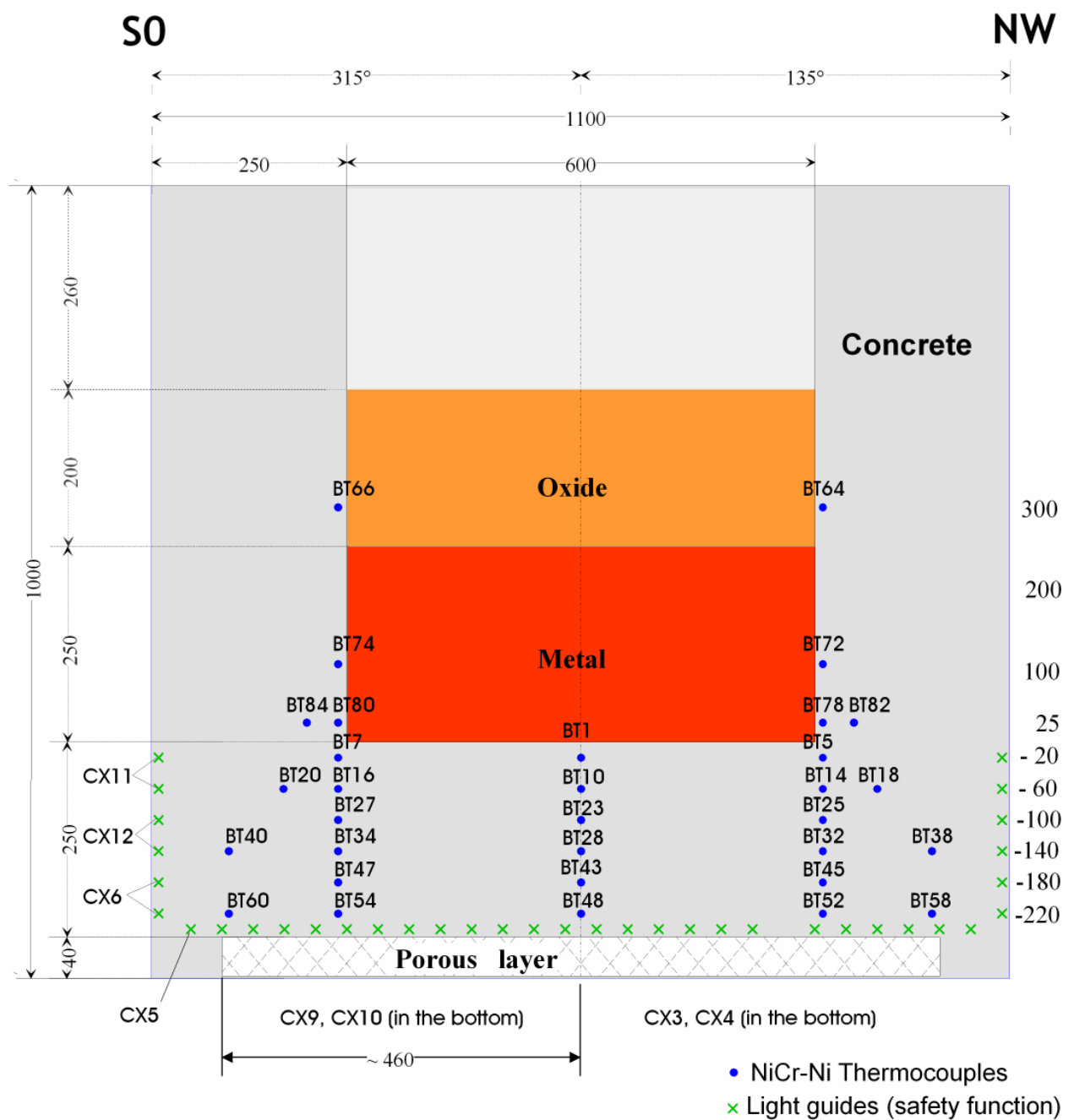
Abb. 4: Anordnung der Thermoelemente in der Sekundärebene (Schnitt B-B (SO-NW) unter 135° durch den Betontiegel, siehe Abb. 2)

A.3.1 Instrumentierungsebene 1 (300 mm)

Diese oberste horizontale Instrumentierungsebene oberhalb des Tiegelbodens, im Abstand von 300 mm, enthält 4 NiCr/Ni - Thermoelemente in der Primärebene und 2 NiCr/Ni - Thermoelemente in der Sekundärebene. Sie dienen zur Messung der Erosionsgeschwindigkeit in der Tiegelwand. Abb. 5 zeigt die Lage der Thermoelemente in der Ebene.

Die Positionen sind:

Primärebene

Name	Radius	Winkel	Höhe
BT 63	310	45	300
BT 65	310	225	300
BT 67	350	45	300
BT 68	350	225	300

Sekundärebene

Name	Radius	Winkel	Höhe
BT 64	310	135	300
BT 66	310	315	300
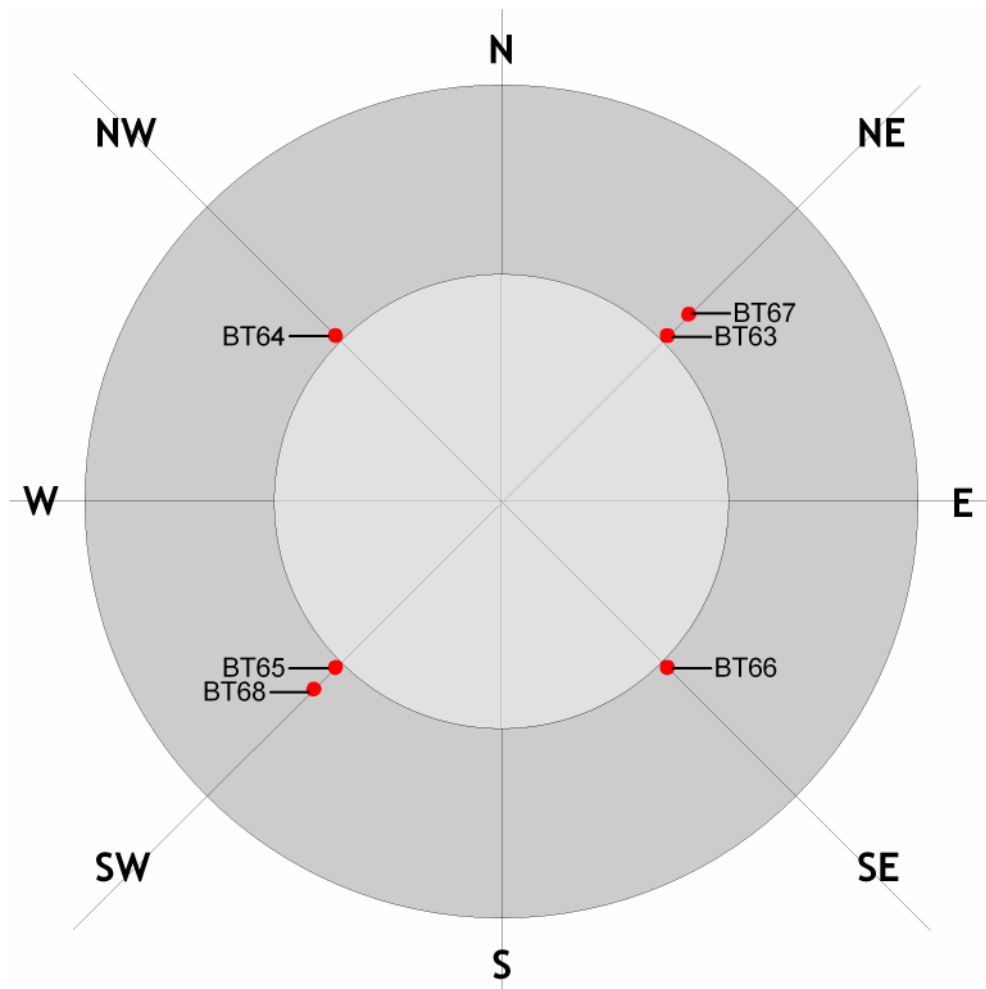
Abb. 5:   Instrumentierungsebene 1 (+300 mm)

A.3.2   Instrumentierungsebene 2 (200 mm)

Die zweite horizontale Instrumentierungsebene oberhalb des Tiegelbodens, im Abstand von 200 mm, enthält 6 NiCr/Ni - Thermoelemente in der Primärebene. In der Sekundärebene sind in dieser Höhe keine Thermoelemente vorgesehen. Die Thermoelemente dienen zur Messung der Erosionsgeschwindigkeit in der Tiegelwand. Abb. 6 zeigt die Lage der Thermoelemente in der Ebene.

Die Positionen sind:

Primärebene

Name	Radius	Winkel	Höhe
BT 41	310	45	200
BT 42	310	225	200
BT 69	350	45	200
BT 70	350	225	200
BT 87	380	45	200
BT 88	380	225	200
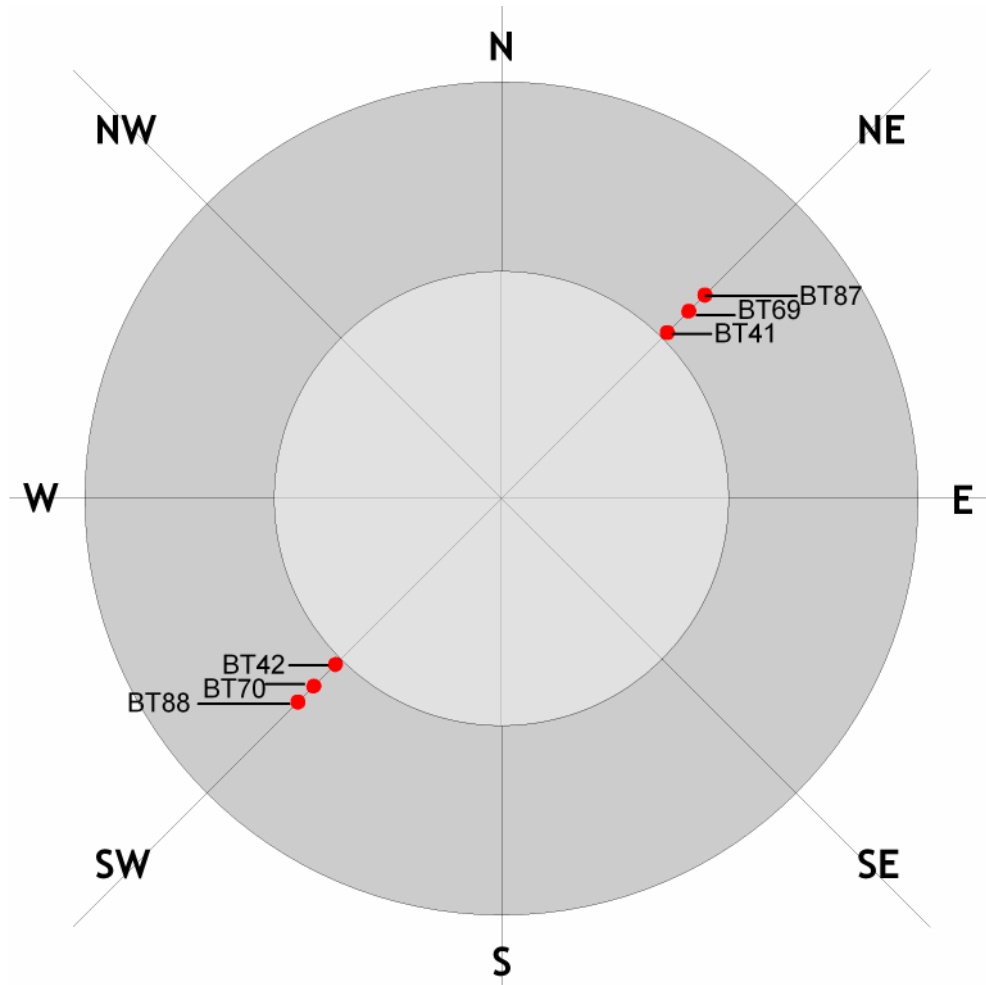
Abb. 6:   Instrumentierungsebene 2 (+ 200 mm)

A.3.3 Instrumentierungsebene 3 (100 mm)

Die dritte horizontale Instrumentierungsebene oberhalb des Tiegelbodens, im Abstand von 100 mm, enthält 4 NiCr/Ni - Thermoelemente in der Primärebene und 2 NiCr/Ni - Thermoelemente in der Sekundärebene. Sie dienen zur Messung der Erosionsgeschwindigkeit in der Tiegelwand. Abb. 7 zeigt die Lage der Thermoelemente in der Ebene.

Die Positionen sind:

Primärebene

Name	Radius	Winkel	Höhe
BT 71	310	45	100
BT 73	310	225	100
BT 75	350	45	100
BT 76	350	225	100

Sekundärebene

Name	Radius	Winkel	Höhe
BT 72	310	135	100
BT 74	310	315	100

Abb. 7:   Instrumentierungsebene 3 (+ 100 mm)

A.3.4   Instrumentierungsebene 4 (25 mm)

Die vierte horizontale Instrumentierungsebene über dem Tiegelboden, im Abstand von 25 mm, enthält 6 NiCr/Ni - Thermoelemente in der Primärebene und 4 NiCr/Ni - Thermoelemente in der Sekundärebene. Sie dienen zur Messung der Erosionsgeschwindigkeit in der unteren Tiegelwand. Abb. 8 zeigt die Lage der Thermoelemente in der Ebene.

Die Positionen sind:

Primärebene

Name	Radius	Winkel	Höhe
BT 77	310	45	25
BT 79	310	225	25
BT 81	350	45	25
BT 83	350	225	25
BT 85	380	45	25
BT 86	380	225	25

Sekundärebene

Name	Radius	Winkel	Höhe
BT 78	310	135	25
BT 80	310	315	25
BT 82	350	135	25
BT 84	350	315	25
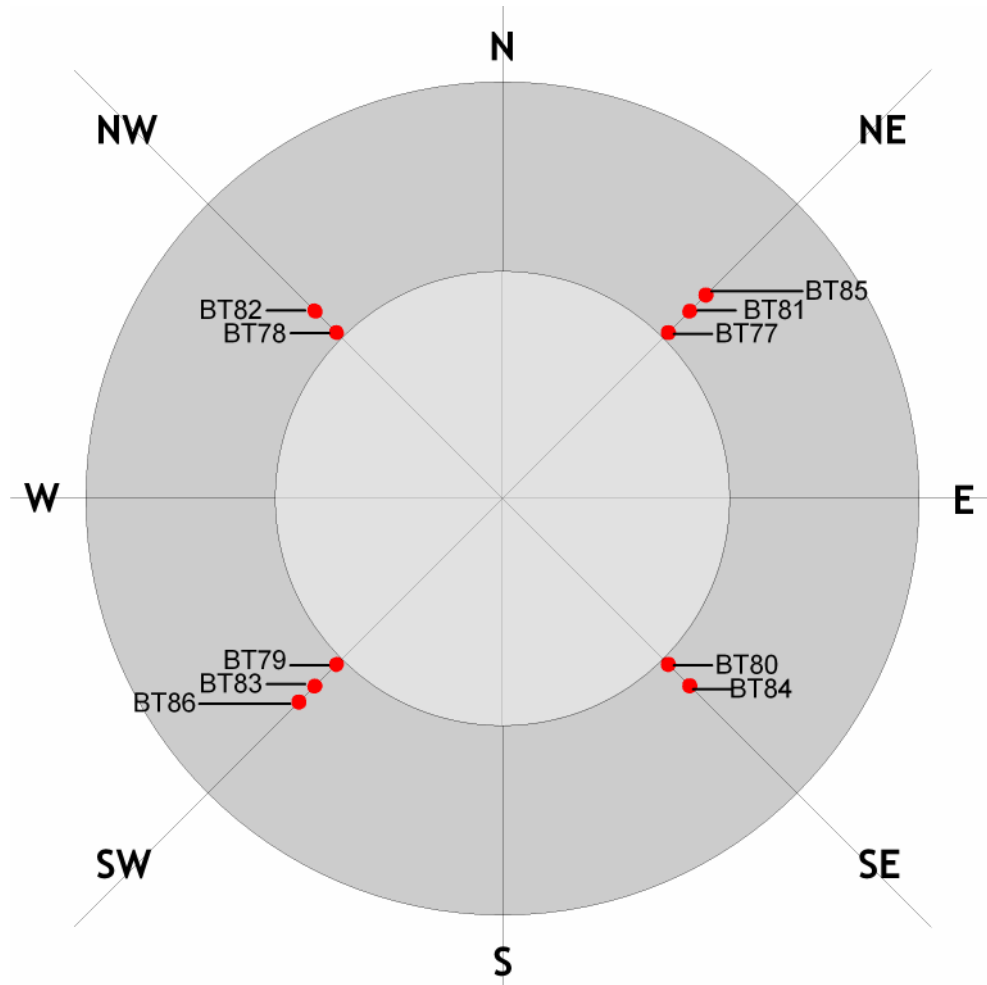
Abb. 8: Instrumentierungsebene 4 (+ 25 mm)

A.3.5   Instrumentierungsebene 5 (-20 mm)

Die erste horizontale Instrumentierungsebene im Tiegelboden, 20 mm tief, enthält 7 NiCr/Ni - Thermoelemente in der Primärebene und 2 NiCr/Ni - Thermoelemente in der Sekundärebene. Sie dienen zur Messung der Erosionsgeschwindigkeit im Tiegelboden. Abb. 9 zeigt die Lage der Thermoelemente in der Ebene.

Die Positionen sind:

Primärebene

Name	Radius	Winkel	Höhe
BT 01	0	0	-20
BT 02	180	45	-20
BT 03	180	225	-20
BT 04	310	45	-20
BT 06	310	225	-20
BT 08	350	45	-20
BT 09	350	225	-20

Sekundärebene

Name	Radius	Winkel	Höhe
BT 05	310	135	-20
BT 07	310	315	-20
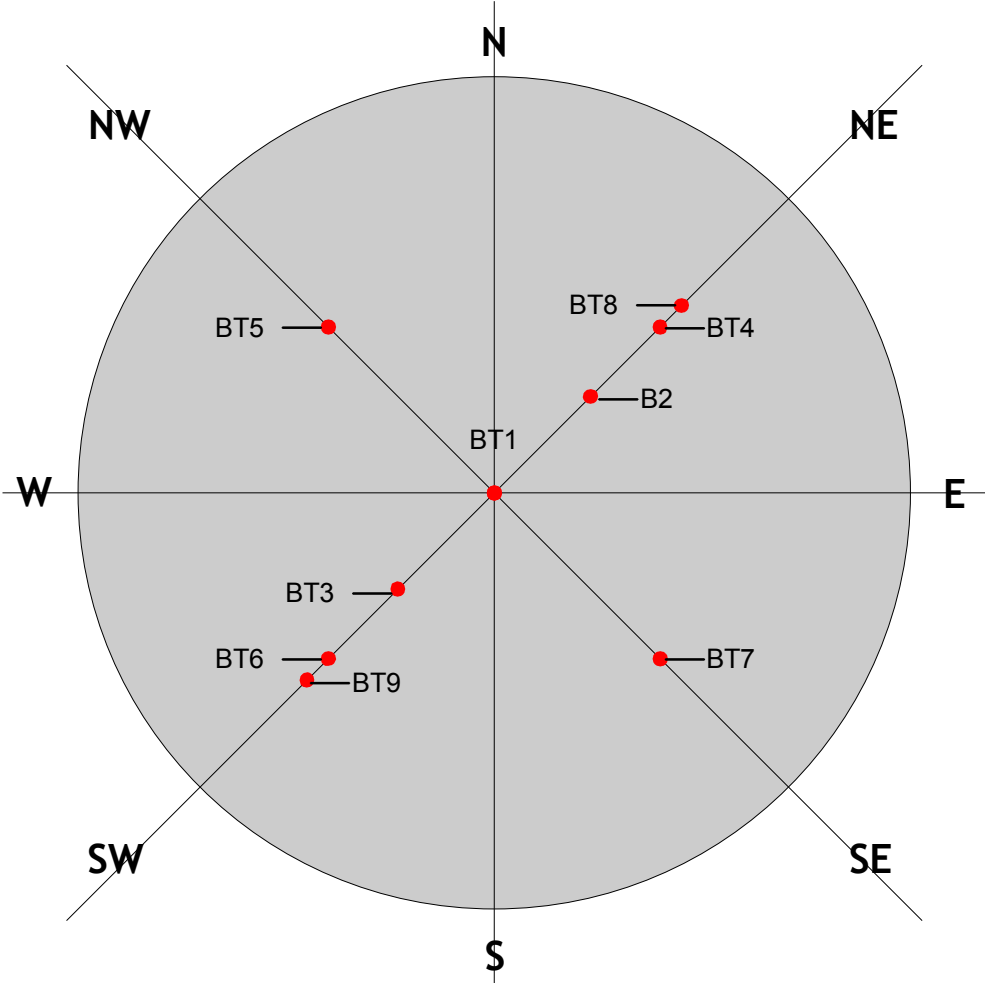
Abb. 9: Instrumentierungsebene 5 (- 20 mm)

A.3.6   Instrumentierungsebene 6 (-60 mm)

Die zweite horizontale Instrumentierungsebene im Tiegelboden, 60 mm tief, enthält 9 NiCr/Ni - Thermoelemente in der Primärebene und 4 NiCr/Ni - Thermoelemente in der Sekundärebene. Sie dienen zur Messung der Erosionsgeschwindigkeit im Tiegelboden. Abb. 10 zeigt die Lage der Thermoelemente in der Ebene.

Die Positionen sind:

<table>
<tr><td colspan="4" align="center">Primärebene</td><td></td><td colspan="4" align="center">Sekundärebene</td></tr>
<tr><td>Name</td><td>Radius</td><td>Winkel</td><td>Höhe</td><td></td><td>Name</td><td>Radius</td><td>Winkel</td><td>Höhe</td></tr>
<tr><td>BT 10</td><td>0</td><td>0</td><td>-60</td><td></td><td>BT 14</td><td>310</td><td>135</td><td>-60</td></tr>
<tr><td>BT 11</td><td>180</td><td>45</td><td>-60</td><td></td><td>BT 16</td><td>310</td><td>315</td><td>-60</td></tr>
<tr><td>BT 12</td><td>180</td><td>225</td><td>-60</td><td></td><td>BT 18</td><td>380</td><td>135</td><td>-60</td></tr>
<tr><td>BT 13</td><td>310</td><td>45</td><td>-60</td><td></td><td>BT 20</td><td>380</td><td>315</td><td>-60</td></tr>
<tr><td>BT 15</td><td>310</td><td>225</td><td>-60</td><td></td><td></td><td></td><td></td><td></td></tr>
<tr><td>BT 17</td><td>380</td><td>45</td><td>-60</td><td></td><td></td><td></td><td></td><td></td></tr>
<tr><td>BT 19</td><td>380</td><td>225</td><td>-60</td><td></td><td></td><td></td><td></td><td></td></tr>
<tr><td>BT 21</td><td>420</td><td>45</td><td>-60</td><td></td><td></td><td></td><td></td><td></td></tr>
<tr><td>BT 22</td><td>420</td><td>225</td><td>-60</td><td></td><td></td><td></td><td></td><td></td></tr>
</table>

Abb. 10:   **Instrumentierungsebene 6   (-60 mm)**

A.3.7 Instrumentierungsebene 7 (-100 mm)

Die dritte horizontale Instrumentierungsebene im Tiegelboden, 100 mm tief, enthält 3 NiCr/Ni - Thermoelemente in der Primärebene und 2 NiCr/Ni - Thermoelemente in der Sekundärebene. Sie dienen zur Messung der Erosionsgeschwindigkeit im Tiegelboden. Abb. 11 zeigt die Lage der Thermoelemente in der Ebene. Die Positionen sind:
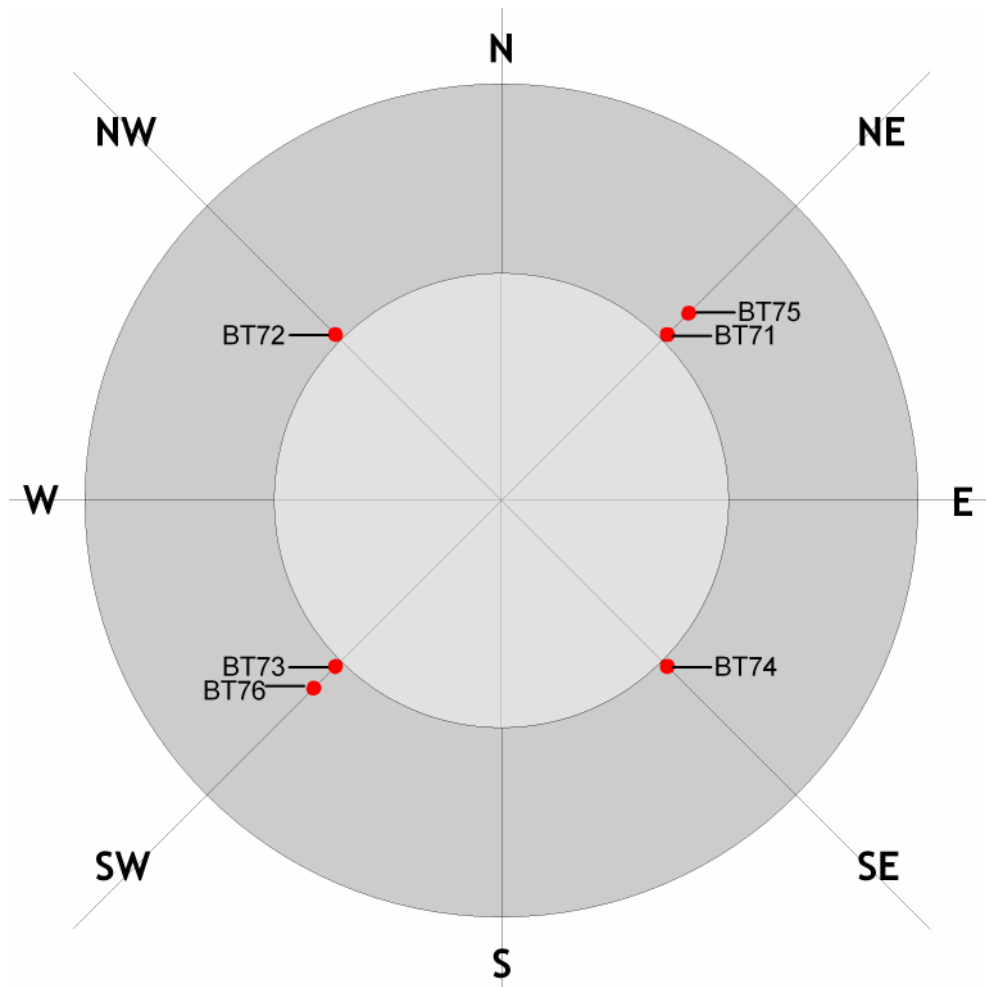
<table>
<tr><td colspan="4">Primärebene</td><td colspan="4">Sekundärebene</td></tr>
<tr><th>Name</th><th>Radius</th><th>Winkel</th><th>Höhe</th><th>Name</th><th>Radius</th><th>Winkel</th><th>Höhe</th></tr>
<tr><td>BT 23</td><td>0</td><td>0</td><td>-100</td><td>BT 25</td><td>310</td><td>135</td><td>-100</td></tr>
<tr><td>BT 24</td><td>310</td><td>45</td><td>-100</td><td>BT 27</td><td>310</td><td>315</td><td>-100</td></tr>
<tr><td>BT 26</td><td>310</td><td>225</td><td>-100</td><td></td><td></td><td></td><td></td></tr>
</table>
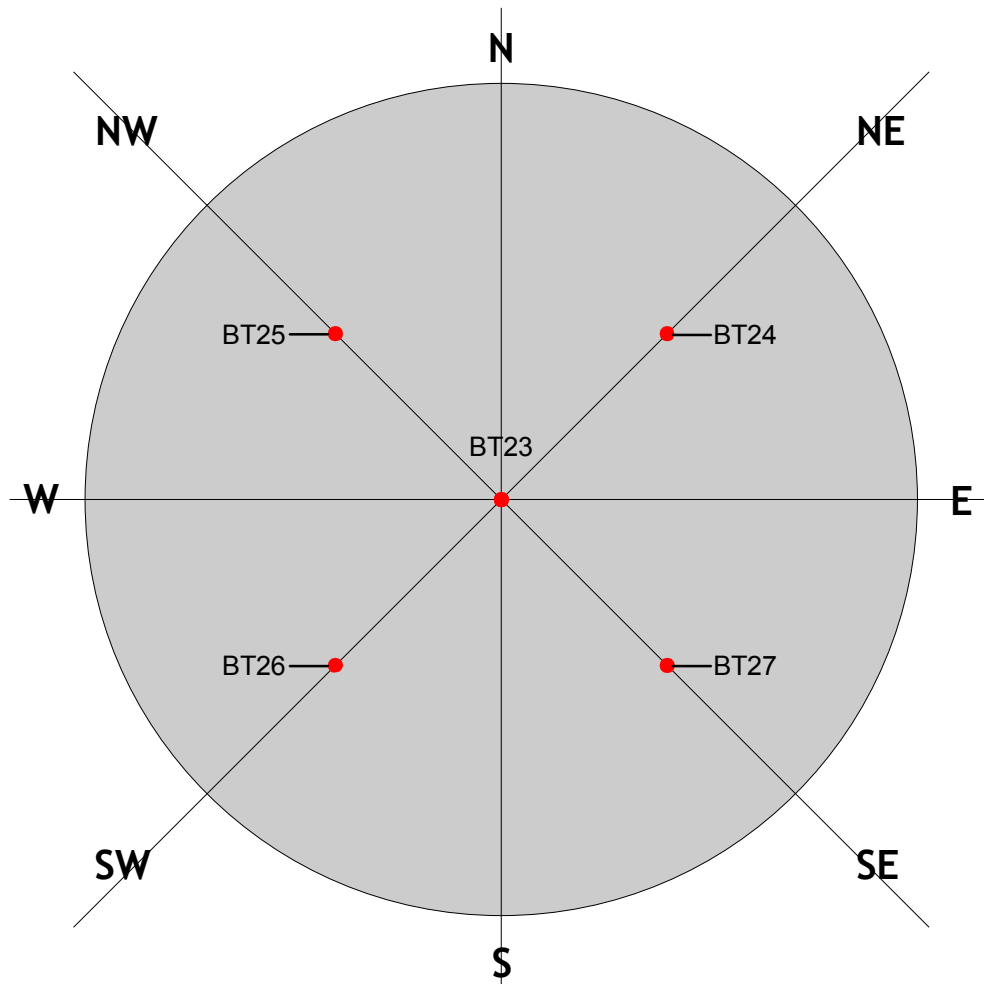
Abb. 11:   Instrumentierungsebene 7 (-100 mm)

A.3.8   Instrumentierungsebene 8 (-140 mm)

Die vierte horizontale Instrumentierungsebene im Tiegelboden, 140 mm tief, enthält 9 NiCr/Ni - Thermoelemente in der Primärebene und 4 NiCr/Ni - Thermoelemente in der Sekundärebene. Sie dienen zur Messung der Erosionsgeschwindigkeit im Tiegelboden. Abb. 12 zeigt die Lage der Thermoelemente in der Ebene.

Die Positionen sind:

Primärebene

Name	Radius	Winkel	Höhe
BT 28	0	0	-140
BT 29	180	45	-140
BT 30	180	225	-140
BT 31	310	45	-140
BT 33	310	225	-140
BT 35	380	45	-140
BT 36	380	225	-140
BT 37	460	45	-140
BT 39	460	225	-140

Sekundärebene

Name	Radius	Winkel	Höhe
BT 32	310	135	-140
BT 34	310	315	-140
BT 38	460	135	-140
BT 40	460	315	-140
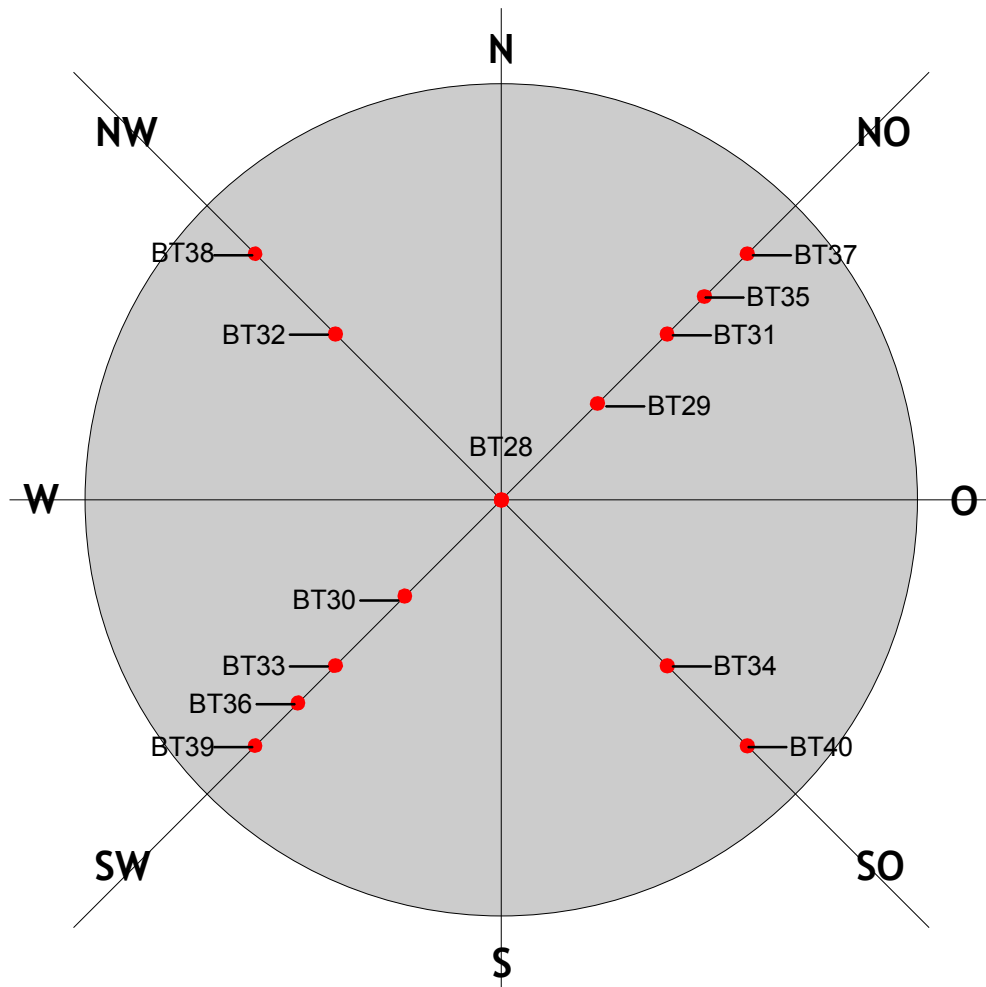
Abb. 12: Instrumentierungsebene 8 (-140 mm)

A.3.9   Instrumentierungsebene 9 (-180 mm)

Die fünfte horizontale Instrumentierungsebene im Tiegelboden, 180 mm tief, enthält 3 NiCr/Ni - Thermoelemente in der Primärebene und 2 NiCr/Ni - Thermoelemente in der Sekundärebene. Sie dienen zur Messung der Erosionsgeschwindigkeit im Tiegelboden. Abb. 13 zeigt die Lage der Thermoelemente in der Ebene.

Die Positionen sind:

<div style="display:flex">

Primärebene

Name	Radius	Winkel	Höhe
BT 43	0	0	-180
BT 44	310	45	-180
BT 46	310	225	-180

Sekundärebene

| Name	Radius	Winkel	Höhe
BT 45	310	135	-180
BT 47	310	315	-180

</div>
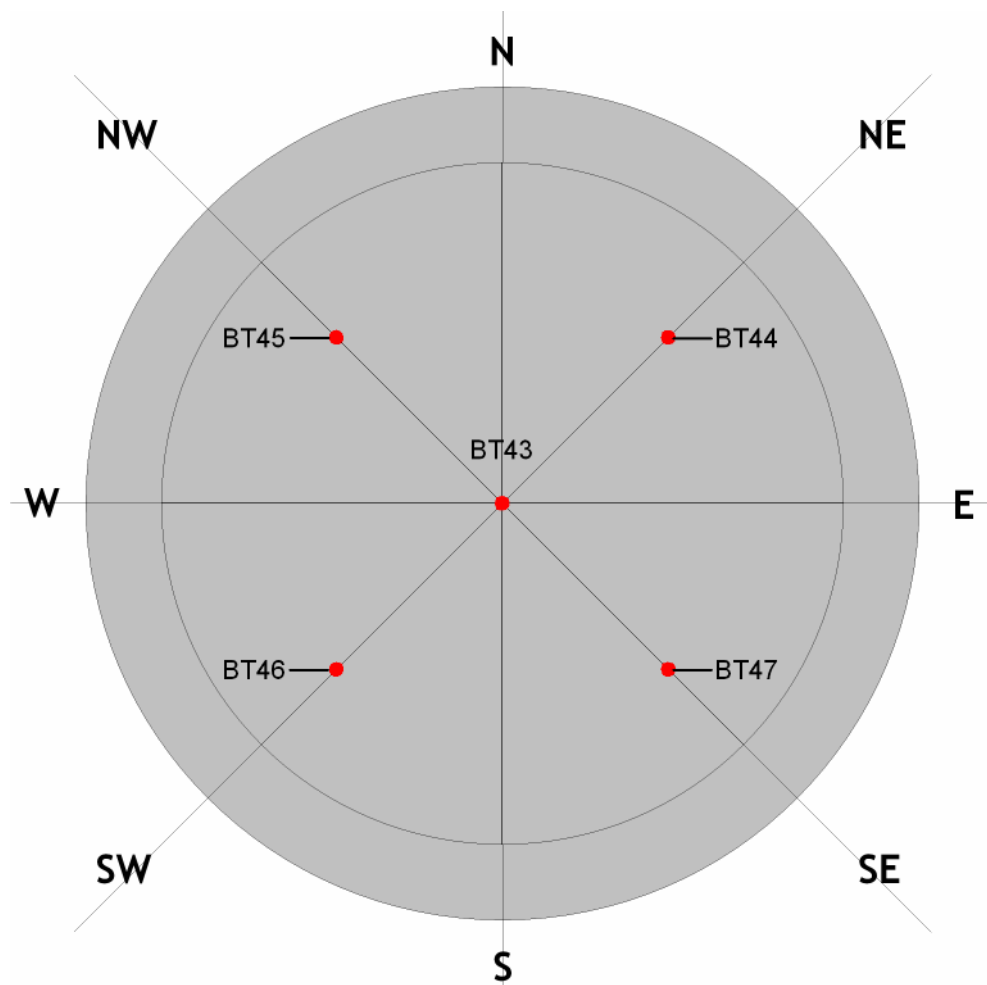
Abb. 13:   Instrumentierungsebene 9 (-180 mm)

A.3.10   Instrumentierungsebene 10 (-220 mm)

Die sechste horizontale Instrumentierungsebene im Tiegelboden, 220 mm tief, enthält 11 NiCr/Ni - Thermoelemente in der Primärebene und 4 NiCr/Ni - Thermoelemente in der Sekundärebene. Sie dienen zur Messung der Erosionsgeschwindigkeit im Tiegelboden. Abb. 14 zeigt die Lage der Thermoelemente in der Ebene.

Die Positionen sind:

<table>
<tr><td colspan="4" align="center">Primärebene</td></tr>
<tr><th>Name</th><th>Radius</th><th>Winkel</th><th>Höhe</th></tr>
<tr><td>BT 48</td><td>0</td><td>0</td><td>-220</td></tr>
<tr><td>BT 49</td><td>180</td><td>45</td><td>-220</td></tr>
<tr><td>BT 50</td><td>180</td><td>225</td><td>-220</td></tr>
<tr><td>BT 51</td><td>310</td><td>45</td><td>-220</td></tr>
<tr><td>BT 53</td><td>310</td><td>225</td><td>-220</td></tr>
<tr><td>BT 55</td><td>380</td><td>45</td><td>-220</td></tr>
<tr><td>BT 56</td><td>380</td><td>225</td><td>-220</td></tr>
<tr><td>BT 57</td><td>460</td><td>45</td><td>-220</td></tr>
<tr><td>BT 59</td><td>460</td><td>225</td><td>-220</td></tr>
<tr><td>BT 61</td><td>500</td><td>45</td><td>-220</td></tr>
<tr><td>BT 62</td><td>500</td><td>225</td><td>-220</td></tr>
</table>

<table>
<tr><td colspan="4" align="center">Sekundärebene</td></tr>
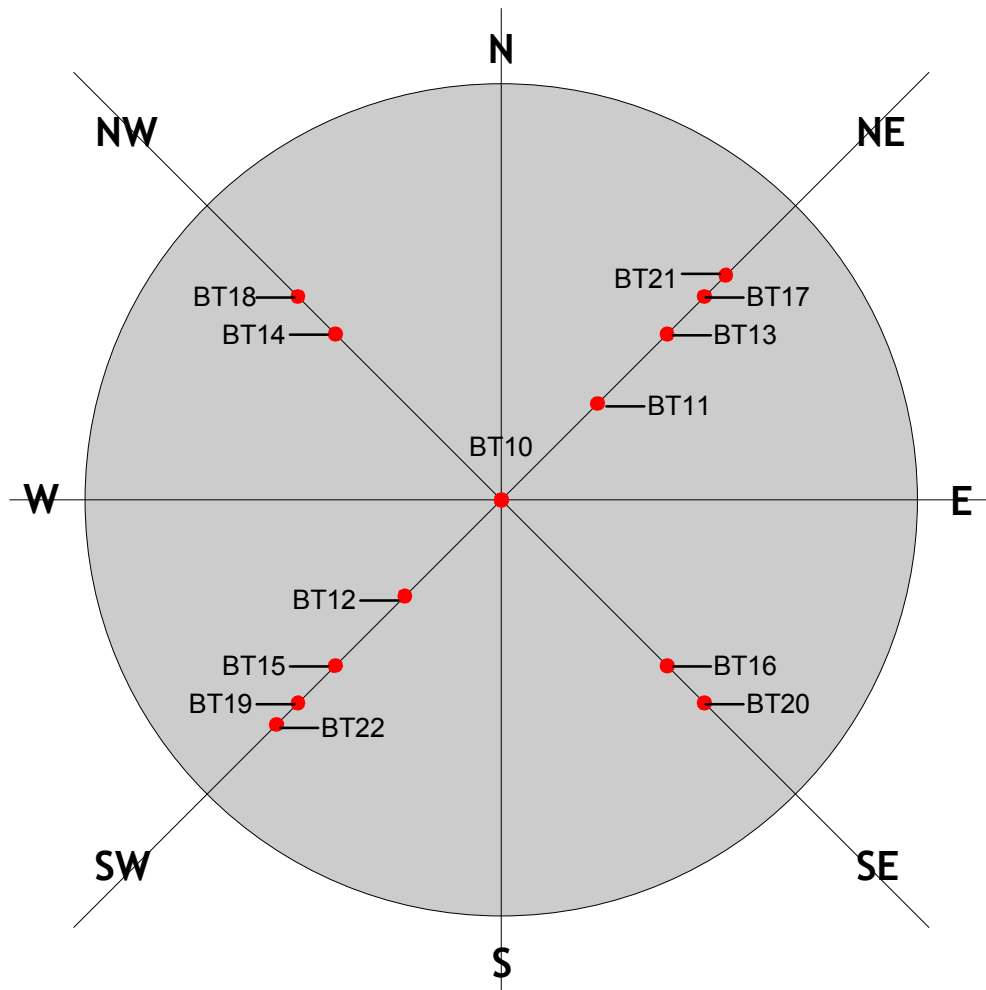<tr><th>Name</th><th>Radius</th><th>Winkel</th><th>Höhe</th></tr>
<tr><td>BT 52</td><td>310</td><td>135</td><td>-220</td></tr>
<tr><td>BT 54</td><td>310</td><td>315</td><td>-220</td></tr>
<tr><td>BT 58</td><td>460</td><td>135</td><td>-220</td></tr>
<tr><td>BT 60</td><td>460</td><td>315</td><td>-220</td></tr>
</table>
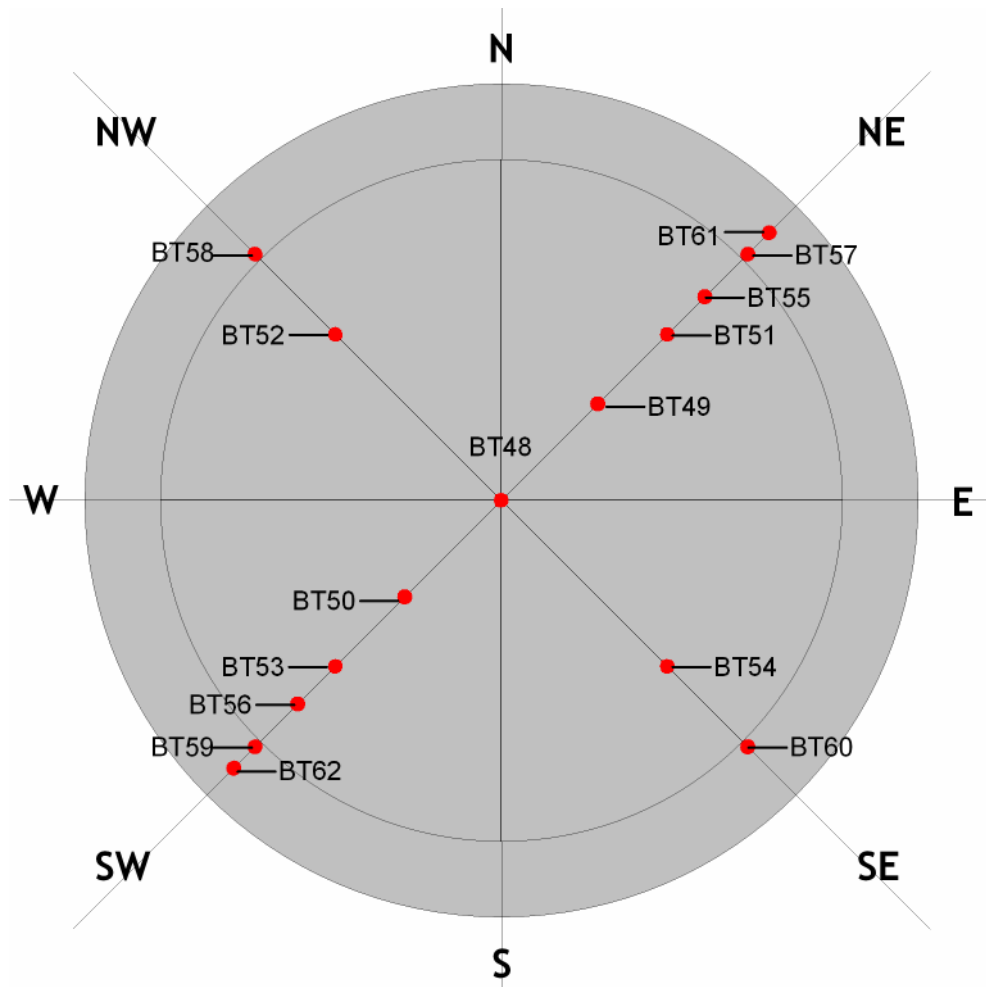
Abb. 14:   Instrumentierungsebene 10 (-220 mm)

A.3.11 Lichtleiter im Boden des Tiegels

Im Tiegelboden, 10 mm oberhalb der porösen Schicht, liegen 4 Lichtleiter, die bei Zerstörung durch Schmelze eine Induktorabschaltung auslösen. Sie sind entsprechend Abb. 15 angeordnet.

Für die Lichtleiter gelten die folgenden Zuordnungen:

CX 3 und CX 4   W - Hälfte, nach Norden herausgeführt

CX 9 und CX 10   O - Hälfte, nach Süden herausgeführt
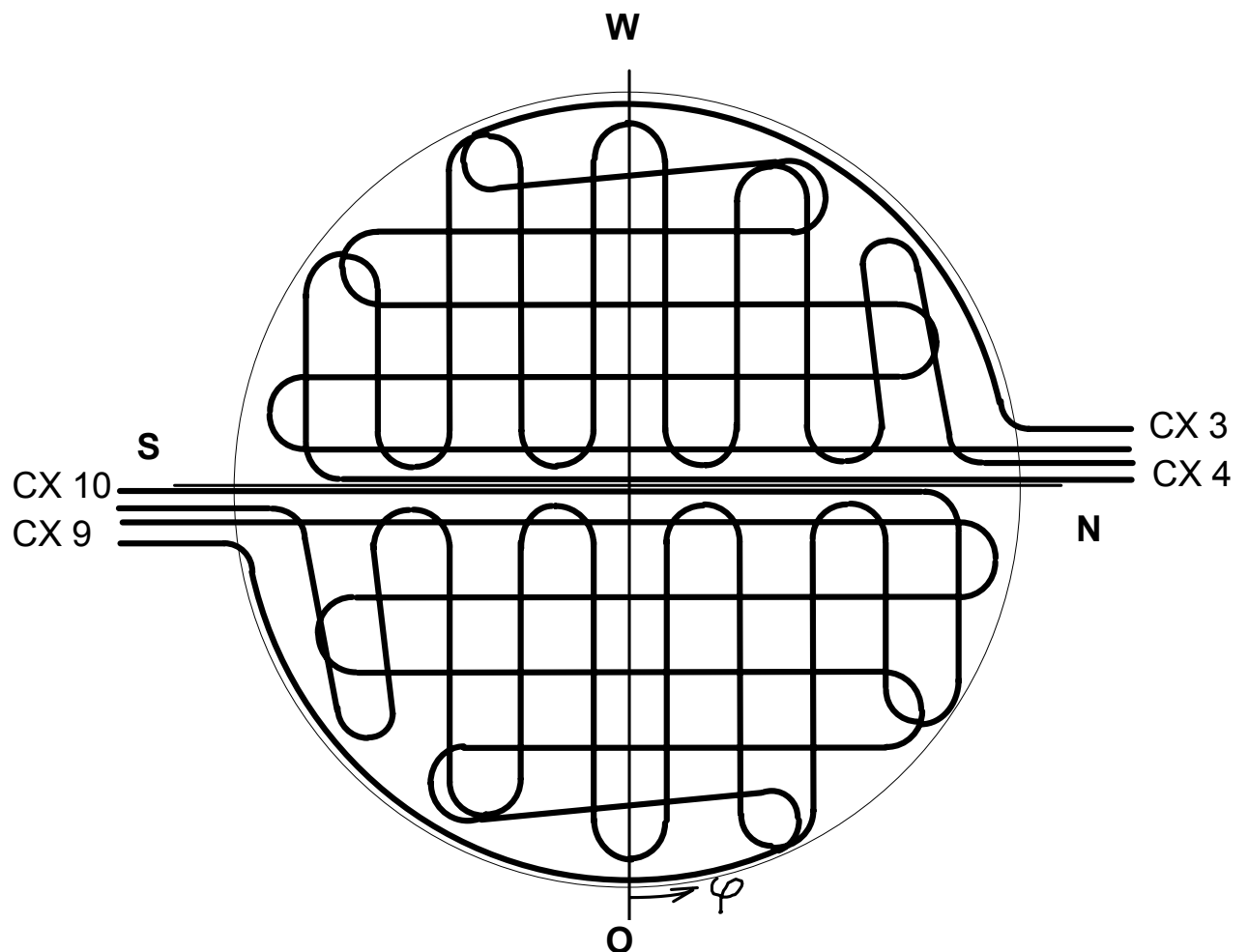
Lichtleiter CX 3, CX 4, CX 9, CX 10 mit Abschaltberechtigung

Abb. 15: Lichtleiter im Boden

A.3.12 Lichtleiter im Rand des Tiegels

In der unteren Ecke im Übergang vom Boden zum Rand befinden sich die beiden Lichtleiter CX 5 und CX 6. CX 5 besteht aus einer Windung und befindet sich bei r = 500 mm und z = -240 mm (siehe Abbildungen 3 und 4). CX 6 besteht aus den beiden unteren Windungen im Tiegelrand in Höhe z = -220 mm und z = -180 mm. Oberhalb von CX 6 im Tiegelrand befinden sich die beiden Lichtleiter CX 11 und CX 12 mit je 2 Windungen im Abstand von 40 mm bei den z-Positionen -140 mm, -100 mm, -60 mm und -20 mm.. Die Lichtleiter lösen bei Zerstörung eine Alarmmeldung aus.

CX 5 und CX 6 werden nach Norden, CX 11 und CX 12 nach Süden aus dem Tiegel herausgeführt.
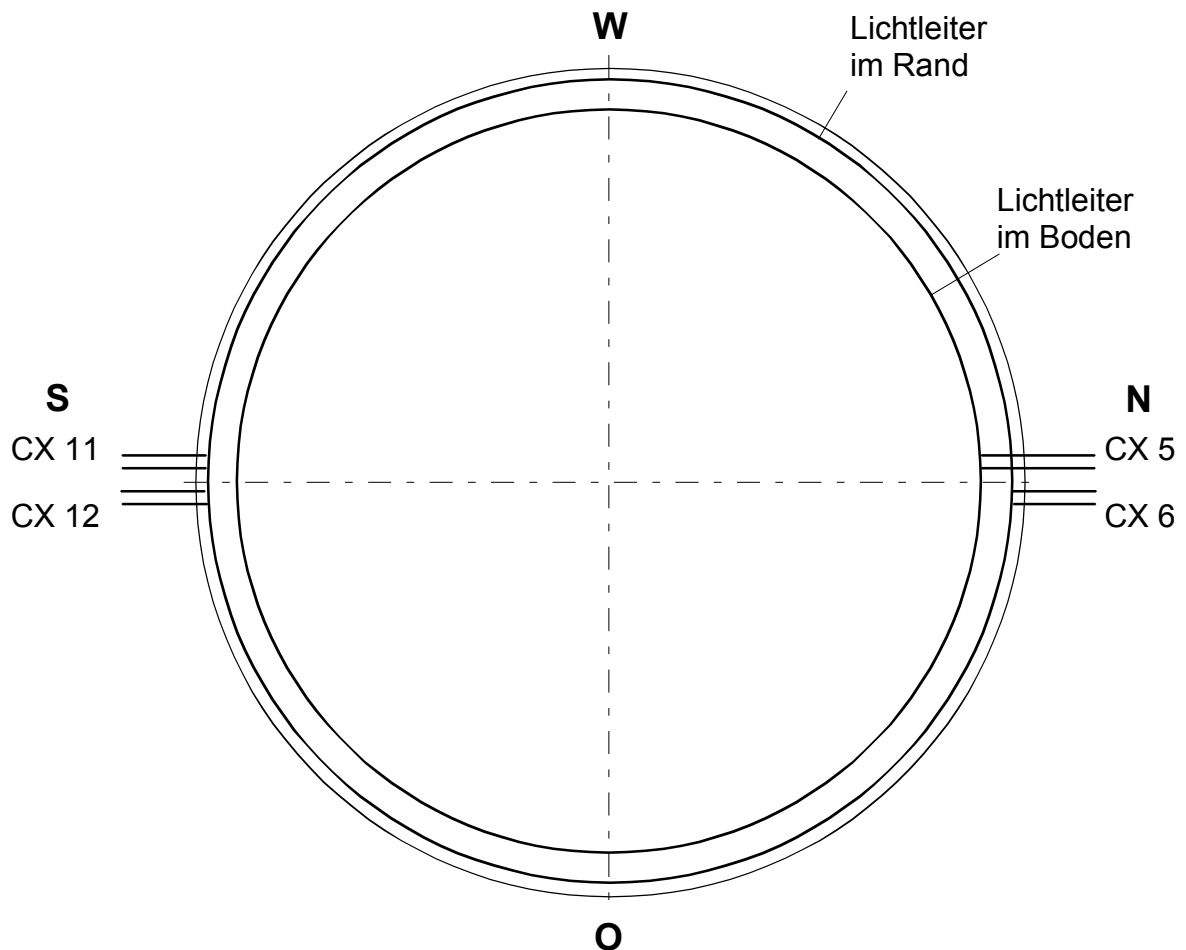
Lichtleiter CX 5, CX 6 und CX 11, CX 12 mit Alarmberechtigung

Abb. 16: Lichtleiter im Rand und im Randbereich des Bodens

(horizontaler Schnitt)

A.3.13 Instrumentierung an der Innenseite des GFK-Beton-Schutzrohres

Lichtleiter:

Die Lichtleiter CX 1, CX2, CX 7 und CX 8 befinden sich außerhalb des Betontiegels in 12 Nuten in der Innenwand des GFK-Beton-Schutzrohres (Abb. 17). Jeder Lichtleiter hat 3 vollständige Windungen. CX 1 und CX 2 decken den unteren Teil des Rohres ab mit einem Abstand der Windungen von 20 mm, wobei jeweils die Windungen von CX 1 und CX 2 abwechseln. In entsprechender Weise schließen die Lichtleiter CX 7 und CX 8 nach oben an. Die erste Lichtleiter - Windung beginnt bei 80 mm ab der Unterkante des Schutzrohres. Die letzte der 12 Windungen endet bei 300 mm. Damit werden 220 mm des Schutzrohres mit jeweils 20 mm Abstand abgedeckt.

Thermoelemente:

4 NiCr/Ni - Thermoelemente CT 1 - CT 4 befinden sich, jeweils unter 45°, auf der Innenseite des GFK-Beton-Schutzrohres ca. 50 mm über der Unterkante des Rohres.

Die Positionen sind:

Name	Radius	Winkel °
CT 1	571	135
CT 2	571	45

Name	Radius	Winkel °
CT 3	571	315
CT 4	571	225

Die Leitungen werden, entsprechend ihrer Lage im Tiegel, nach Süden bzw. Norden aus dem Tiegel herausgeführt.

A.3.14 Instrumentierung an der Außenseite des GFK-Beton-Schutzrohres

Etwa 100 mm oberhalb der Unterkante des GFK-Beton-Schutzrohres sind 4 NiCr/Ni - Thermoelemente CT 9 - CT 12 jeweils unter 45° außen auf dem Rohr angebracht, um dessen Temperaturanstieg zu kontrollieren. Diese Thermoelemente liegen in radialer Richtung gegenüber den Thermoelementen CT 1 - CT 4.

Die Meßpositionen sind:

Name	Radius	Winkel
CT 9	845	135
CT 10	845	45

Name	Radius	Winkel
CT 11	845	315
CT 12	845	225

Diese Instrumentierung wird im Versuch COMET-L1 aus Gründen der Kanalbelegung auf dem Datenerfassungssystem <u>nicht</u> aufgeschaltet.
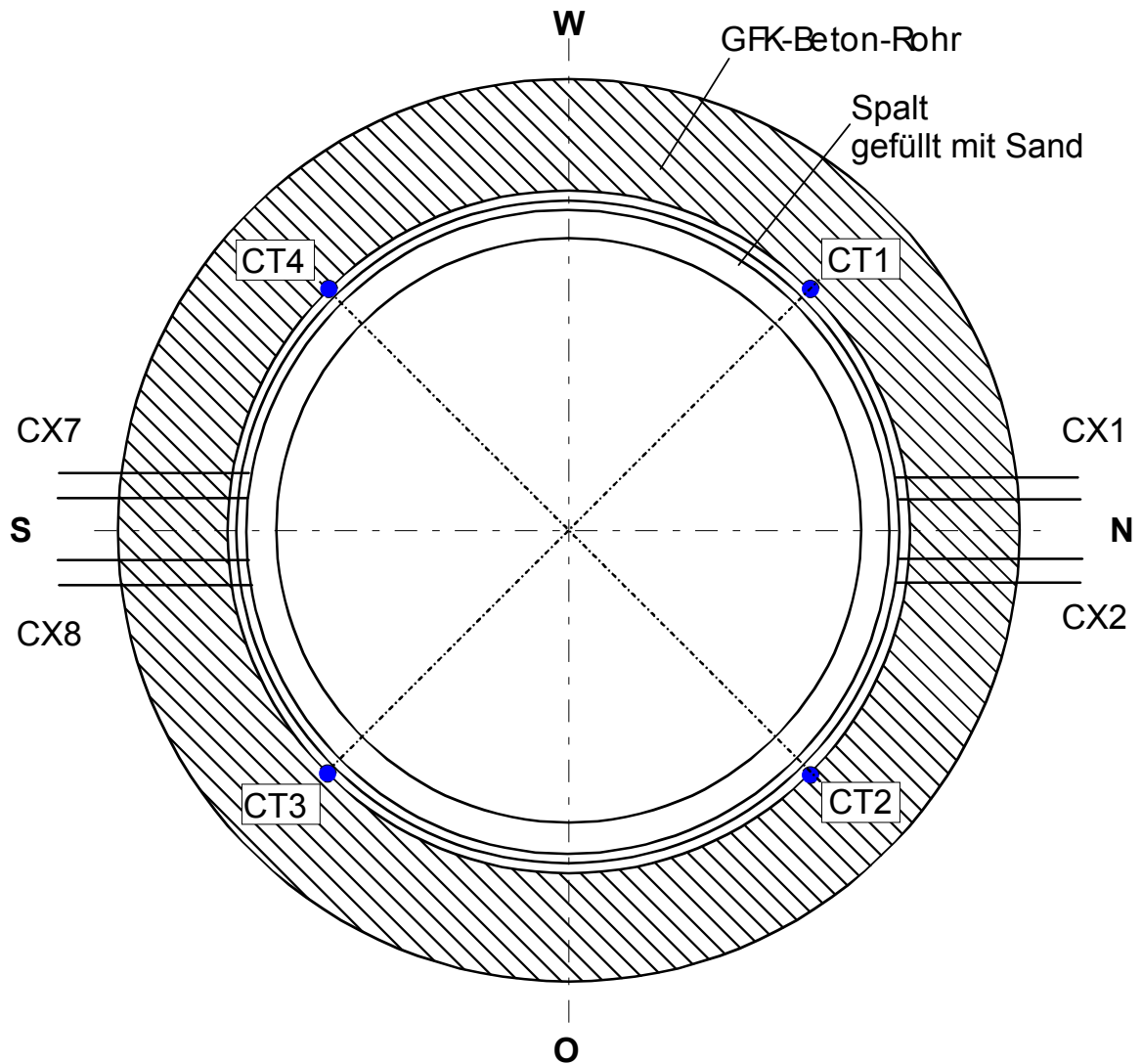
Lichtleiter CX 1, CX 2, CX 7, CX 8 mit Alarmberechtigung

Thermoelemente CT 1 bis CT 4

Abb. 17: Instrumentierung auf der Innenseite des Beton-Schutzrohres
(horizontaler Schnitt)

Appendix B: Data Acquisition and Channel Assignments

Table B1 lists all signals that are registered on the MICROLINK data acquisition system. The blocks 1, 2, 3, 5, 7, 9, and 11 of MICRLONK are equipped with high quality differential amplifiers, the blocks 4, 6, 8, 10,and 12 have "single ended" amplifier inputs with less noise reduction.

Table B1: COMET-L1 Meßstellenliste für Microlink-Datenerfassung

Log. Kan	HW Kan.	Block	Name	Meßgröße	Type	Position: r,Φ,h
1	0	01:00	BT 1	Betontemperatur	NiCr/Ni	0, 0, -20
2	1	01:01	BT 2	Betontemperatur	NiCr/Ni	180, 45, -20
3	2	01:02	BT 4	Betontemperatur	NiCr/Ni	310, 45, -20
4	3	01:03	BT 5	Betontemperatur	NiCr/Ni	310, 135, -20
5	4	01:04	BT 8	Betontemperatur	NiCr/Ni	350, 45, -20
6	5	01:05	BT 10	Betontemperatur	NiCr/Ni	0, 0, -60
7	6	01:06	BT 11	Betontemperatur	NiCr/Ni	180, 45, -60
8	7	01:07	BT 13	Betontemperatur	NiCr/Ni	310, 45, -60
9	8	01:08	BT 14	Betontemperatur	NiCr/Ni	310, 135, -60
10	9	01:09	BT 17	Betontemperatur	NiCr/Ni	380, 45, -60
11	10	01:10	BT 18	Betontemperatur	NiCr/Ni	380, 135, -60
12	11	01:11	BT 21	Betontemperatur	NiCr/Ni	420, 45, -60
13	12	01:12	BT 23	Betontemperatur	NiCr/Ni	0, 0, -100
14	13	01:13	BT 24	Betontemperatur	NiCr/Ni	310, 45, -100
15	14	01:14	BT 25	Betontemperatur	NiCr/Ni	310, 135, -100
16	15	01:15	BT 29	Betontemperatur	NiCr/Ni	180, 45, -140
17	32	02:16	TE-3	TE-Ref. Modul 3	Pt 100	Mainframe
18	33	03:00	BT 31	Betontemperatur	NiCr/Ni	310, 45, -140
19	34	03:01	BT 32	Betontemperatur	NiCr/Ni	310, 135, -140
20	35	03:02	BT 35	Betontemperatur	NiCr/Ni	380, 45, -140
21	36	03:03	BT 41	Betontemperatur	NiCr/Ni	310, 45, +200
22	37	03:04	BT 44	Betontemperatur	NiCr/Ni	310, 45, -180
23	38	03:05	BT 45	Betontemperatur	NiCr/Ni	310, 135, -180

24	39	03:06	BT 49	Betontemperatur	NiCr/Ni	180, 45, -220
25	40	03:07	BT 51	Betontemperatur	NiCr/Ni	310, 45, -220
26	41	03:08	BT 52	Betontemperatur	NiCr/Ni	310, 135, -220
27	42	03:09	BT 3	Betontemperatur	NiCr/Ni	180, 225, -20
28	43	03:10	BT 6	Betontemperatur	NiCr/Ni	310, 225, -20
29	44	03:11	BT 7	Betontemperatur	NiCr/Ni	310, 315, -20
30	45	03:12	BT 9	Betontemperatur	NiCr/Ni	350, 225, -20
31	46	03:13	BT 12	Betontemperatur	NiCr/Ni	180, 225, -60
32	47	03:14	BT 15	Betontemperatur	NiCr/Ni	310, 225, -60
33	48	03:15	BT 16	Betontemperatur	NiCr/Ni	310, 315, -60
34	65	04:16	TE-5	TE-Ref. Modul 5	Pt 100	Mainframe
35	66	05:00	BT 19	Betontemperatur	NiCr/Ni	380, 225, -60
36	67	05:01	BT 20	Betontemperatur	NiCr/Ni	380, 315, -60
37	68	05:02	BT 22	Betontemperatur	NiCr/Ni	420, 225, -60
38	69	05:03	BT 26	Betontemperatur	NiCr/Ni	310, 225, -100
39	70	05:04	BT 27	Betontemperatur	NiCr/Ni	310, 315, -100
40	71	05:05	BT 28	Betontemperatur	NiCr/Ni	0, 0, -140
41	72	05:06	BT 30	Betontemperatur	NiCr/Ni	180, 225, -140
42	73	05:07	BT 33	Betontemperatur	NiCr/Ni	310, 225, -140
43	74	05:08	BT 34	Betontemperatur	NiCr/Ni	310, 315, -140
44	75	05:09	BT 88	Betontemperatur	NiCr/Ni	380, 225, +200
45	76	05:10	BT 42	Betontemperatur	NiCr/NI	310, 225, +200
46	77	05:11	BT 43	Betontemperatur	NiCr/Ni	0, 0, -180
47	78	05:12	BT 46	Betontemperatur	NiCr/Ni	310, 225, -180
48	79	05:13	BT 47	Betontemperatur	NiCr/Ni	310, 315, -180
49	80	05:14	BT 48	Betontemperatur	NiCr/Ni	0, 0, -220
50	81	05:15	BT 50	Betontemperatur	NiCr/Ni	180, 225, -220
51	98	06:16	TE-7	TE-Ref. Modul 7	Pt 100	Mainframe
52	99	07:00	BT 53	Betontemperatur	NiCr/Ni	310, 225, -220
53	100	07:01	BT 54	Betontemperatur	NiCr/Ni	310, 315, -220
54	101	07:02	RT 1	Kühlwasser ein Joche	NiCr/Ni	Jochkühlung
55	102	07:03	RT 2	Kühlwasser aus Joche	NiCr/Ni	Jochkühlung
56	103	07:04	RT 10	Rückfl. Schm.KW Nord	NiCr/Ni	Rücklaufleitung N.

57	104	07:05	BT 55	Betontemperatur	NiCr/Ni	380, 45, -220
58	105	07:06	BT 57	Betontemperatur	NiCr/Ni	460, 45, -220
59	106	07:07	BT 58	Betontemperatur	NiCr/Ni	460, 135, -220
60	107	07:08	BT 61	Betontemperatur	NiCr/Ni	500, 45, -220
61	108	07:09	BT 63	Betontemperatur	NiCr/Ni	310, 45, +300
62	109	07:10	BT 56	Betontemperatur	NiCr/Ni	380, 225, -220
63	110	07:11	BT 59	Betontemperatur	NiCr/Ni	460, 225, -220
64	111	07:12	BT 60	Betontemperatur	NiCr/Ni	460, 315, -220
65	112	07:13	BT 62	Betontemperatur	NiCr/Ni	500, 225, -220
66	113	07:14	BT 65	Betontemperatur	NiCr/Ni	310, 225, +300
67	114	07:15	BT 66	Betontemperatur	NiCr/Ni	310, 315, +300
68	131	08:16	TE-9	TE-Ref. Modul 9	Pt 100	Mainframe
69	132	09:00	BT 64	Betontemperatur	NiCr/Ni	310, 135, +300
70	133	09:01	BT 67	Betontemperatur	NiCr/Ni	350, 45, +300
71	134	09:02	BT 68	Betontemperatur	NiCr/Ni	350, 225, +300
72	135	09:03	BT 70	Betontemperatur	NiCr/Ni	350, 225, +200
73	136	09:04	BT 69	Betontemperatur	NiCr/Ni	350, 45, +200
74	137	09:05	BT 71	Betontemperatur	NiCr/Ni	310, 45, +100
75	138	09:06	BT 72	Betontemperatur	NiCr/Ni	310, 135, +100
76	139	09:07	BT 75	Betontemperatur	NiCr/Ni	350, 45, +100
77	140	09:08	BT 73	Betontemperatur	NiCr/Ni	310, 225, +100
78	141	09:09	BT 74	Betontemperatur	NiCr/Ni	310, 315, +100
79	142	09:10	RT 11	Rückfl. Schm.KW Süd	NiCr/Ni	Rücklaufleitung S.
80	143	09:11	BT 76	Betontemperatur	NiCr/Ni	350, 225, +100
81	144	09:12	BT 77	Betontemperatur	NiCr/Ni	310, 45, +25
82	145	09:13		defekt !		
83	146	09:14	BT 81	Betontemperatur	NiCr/Ni	350, 45, +25
84	147	09:15	BT 82	Betontemperatur	NiCr/Ni	350, 135, +25
85	164	10:16	TE-11	TE-Ref. Modul 11	Pt 100	Mainframe
86	165	11:00	BT 91	Schmelzetemp. Metall	W3Re/25	260, 45, +180
87	166	11:01	BT 92	Schmelzetemp. Oxid	W3Re/25	250, 45, +350
88	167	11:02	BT 93	Schmelzetemp. Metall	W3Re/25	260, 225, +180
89	168	11:03	BT 94	Schmelzetemp. Oxid	W3Re/25	250, 225, +350

90	169	11:04		nicht belegt	Pt10Rh/Pt	
91	170	11:05	CT 1	GFK-Rohr-Temp. Innen	NiCr/Ni	571, 135
92	171	11:06	CT 2	GFK-Rohr-Temp. Innen	NiCr/Ni	571, 45
93	172	11:07	CT 3	GFK-Rohr-Temp. Innen	NiCr/Ni	571, 315
94	173	11:08	CT 4	GFK-Rohr-Temp. Innen	NiCr/Ni	571, 225
95	174	11:09	BT 38	Betontemperatur	NiCr/Ni	460, 135, -140
96	175	11:10	BT 37	Betontemperatur	NiCr/Ni	460, 45, -140
97	176	11:11	BT 40	Betontemperatur	NiCr/Ni	460, 315, -140
98	177	11:12	BT 39	Betontemperatur	NiCr/Ni	460, 225, -140
99	178	11:13	BT 79	Betontemperatur	NiCr/Ni	310, 225, +25
100	179	11:14	BT 80	Betontemperatur	NiCr/Ni	310, 315, +25
101	180	11:15	BT 83	Betontemperatur	NiCr/Ni	350, 225, +25
102	197	12:16	TE-13	TE-Ref. Modul 13	Pt 100	Mainframe
103	16	02:00	WP 1	Wasserdruck	DMS	Tiegel-NW
104	17	02:01	BT 84	Betontemperatur	NiCr/Ni	350, 315, +25
105	18	02:02	WP 3	Wasserdruck	DMS	Tiegel-NO
106	19	02:03	BT 86	Betontemperatur	NiCr/Ni	380, 225, +25
107	20	02:04	WP 8	Wasserdruck	DMS	Tiegel-SO
108	21	02:05	BT 85	Betontemperatur	NiCr/Ni	380, 45, +25
109	22	02:06	WP 10	Wasserdruck	DMS	Tiegel-SW
110	23	02:07	BT 87	Betontemperatur	NiCr/Ni	380, 45, +200
111	24	02:08	WP 15	Wasserdruck	DMS	W-Zulauf
112	25	02:09	HP 1	Hauben-Druck	DMS	0 - 2 bar absolut
113	26	02:10	HP 2	Hauben Druck	DMS	0 - 10 bar diff.
114	27	02:11	BT 78	Betontemperatur	NiCr/Ni	310, 135, +25
115	28	02:12	AR 1	Frequenz	AEG 13	1,2,W+X
116	29	02:13	AN 3	Leistung Umrichter 3	AEG 5	1,2,C+D
117	30	02:14	AN 4	Leistung Umrichter 4	AEG 7	1,2,H+I
118	31	02:15	AU 2	Anl. Spannung 3000 V	AEG 10	1,2,P+R
119	49	04:00				
120	50	04:01				
121	51	04:02				
122	52	04:03				

123	53	04:04	GC 11	Gas-M., INR 1	Q 100-1	
124	54	04:05	GC 12	Gas-M., INR 2	Q 100-1	
125	55	04:06	GC 13	Gas-M., INR 3	Q 100-1	
126	56	04:07	GC 14	Gas-M., INR 4	Q 100-1	
127	57	04:08	GC 15	Gas-M., INR 5	Q 100-1	
128	58	04:09	GC 16	Gas-M., INR 6	Q 100-1	
129	59	04:10	GC 17	Gas-M., INR 7	Q 100-1	
130	60	04:11	GC 18	Gas-M., INR 8	Q 100-1	
131	61	04:12	GX 1	Empf., INR 9	Q 100-1	
132	62	04:13	GC 10	Gas-Scan, INR 10	Q 100-1	
133	63	04:14	GC 21	Gas-M., INR 11	Q 100-2	
134	64	04:15				
135	82	06:00	GC 22	Gas-M., INR 12	Q 100-2	
136	83	06:01	GC 23	Gas-M., INR 13	Q 100-2	
137	84	06:02	GC 24	Gas-M., INR 14	Q 100-2	
138	85	06:03	GC 25	Gas-M., INR 15	Q 100-2	
139	86	06:04	GC 26	Gas-M., INR 16	Q 100-2	
140	87	06:05	GC 27	Gas-M., INR 17	Q 100-2	
141	88	06:06	GC 28	Gas-M., INR 18	Q 100-2	
142	89	06:07	GX 2	Empfindl., INR 19	Q 100-2	
143	90	06:08		Ind. -Bruttoleistung		Berechnet
144	91	06:09	SN 1	Ind. -Nettoleistung		Berechnet
145	92	06:10	AU 2	Ind. -Spannung		Berechnet
146	93	06:11	AR 1	Ind. -Frequenz		Berechnet
147	94	06:12				
148	95	06:13				
149	96	06:14				
150	97	06:15				
151	115	08:00	AA 4	Strom Umrichter 4	AEG 8	1,2,K+L
152	116	08:01	AU 1	Umr. Spannung 1000 V	AEG 9	1,2,M+N
153	117	08:02				
154	118	08:03	AA 5	Kond. Teilstrom A	AEG 11	1,2,S+T
155	119	08:04	AA 6	Kond. Teilstrom B	AEG 12	1,2,U+V

156	120	08:05				
157	121	08:06	RF 1	Rückkühlanlage	Wirbelm.	Durchfluß
158	122	08:07				
159	123	08:08				
160	124	08:09		GQ 22	Hygrom. 2	
161	125	08:10		GT 22	Hygrom. 2	
162	126	08:11	GF 1	Gasvolumen	Flügelrad	
163	127	08:12	GP 1	Gasdruck	DMS	bei Meßdüse
164	128	08:13	RQ 1	Leistung Rückkühl-Anl.	RF1,Pt100	Rückkühlanlage
165	129	08:14	SN 3	Pultanzeige Nettoleistg.		Nettoleistung
166	130	08:15				
167	148	10:00	AP 1	Ar-Druck	DMS	Haube ein
168	149	10:01	AP 2	Ar-Druck	DMS	Ar-Batterie
169	150	10:02	AP 3	Ar-Druck	DMS	Periskop Kühlg.
170	151	10:03	AF 1	Ar-Strom	RotaM ?	Haube ein
171	152	10:04	AF 2	Ar-Strom	Meßblende	Periskop Freibl.
172	153	10:05		GQ 21	Hygrom. 1	
173	154	10:06		GT 21	Hygrom. 1	
174	155	10:07				
175	156	10:08				
176	157	10:09	HP 3	Hauben-Druck	DMS	0 - 100 bar diff.
177	158	10:10	AF 4	Ar-Strom	Meßblende	Aerosol-Spülung
178	159	10:11	AF 3	Ar-Strom	Meßblende	Periskop Kühlg.
179	160	10:12	AE 1	Ereignis	Logik	Zündg., Abstich
180	161	10:13				
181	162	10:14	CK 1	Zeitmarke	Clock	Synchronisation
182	163	10:15				
183	181	12:00	HT 1	Hauben Temp.	NiCr/Ni	Haubenflansch
184	182	12:01	GT 1	Gastmp. n. Abscheider	NiCr/Ni	n. Abscheider
185	183	12:02	GT 2	Gastemp. b. Meßdüse	NiCr/Ni	bei Meßdüse
186	184	12:03	KT 1	Wandtemp. Absch.	NiCr/Ni	Abscheider
187	185	12:04	KT 2	Wandtemp. b. Meßd.	NiCr/Ni	bei Meßdüse
188	186	12:05	KT 3	Zuluft-Temp.	NiCr/Ni	Lüftg. Mitte

189	187	12:06	KT 4	Hallentemp.	Pt 100	
190	188	12:07	KT 10	Temp. Gießrinne	W3Re/25	
191	189	12:08	KM 1	Einguß-Masse	Waage	Reakt. Tiegel
192	190	12:09	GP 2	Staurohrmessung	Diff. Druck	bei Meßdüse
193	191	12:10	CL 1	Wasserstand Tiegel	Druck	Tiegel-N
194	192	12:11	WF 16	Wasserdurchfluß	magn.-ind.	W-Zulauf
195	193	12:12	WF 17	Wasserd.fl. Notkühlung	magn.-ind.	Tiegelhaube
196	194	12:13	KU 1	Kontr.Spannung	0 mV	
197	195	12:14	KU 2	Kontr.Spannung	40 mV	
198	196	12:15	LV 115	Steuerung WF 15	Ventil 115	W-Zulauf

* Verstärker berücksichtigt bereits Kartentemperatur

BT 36, NiCr/Ni (380, 225, -140) nicht aufgelegt, da vor Versuch defekt

BT 60, NiCr/Ni (460, 315, -220) Log Kanal 64, vor Versuch defekt

BT 92, W3Re/25, Temp Oxid (250, 55°, +350) Log Kanal 87, vor Versuch nicht plausibel

Appendix C: Test Data

This appendix provides plots showing the temperature rise in the concrete and the failure of the thermocouples. The thermocouples are grouped according to the lines shown in Figure 20 and Figure 21.

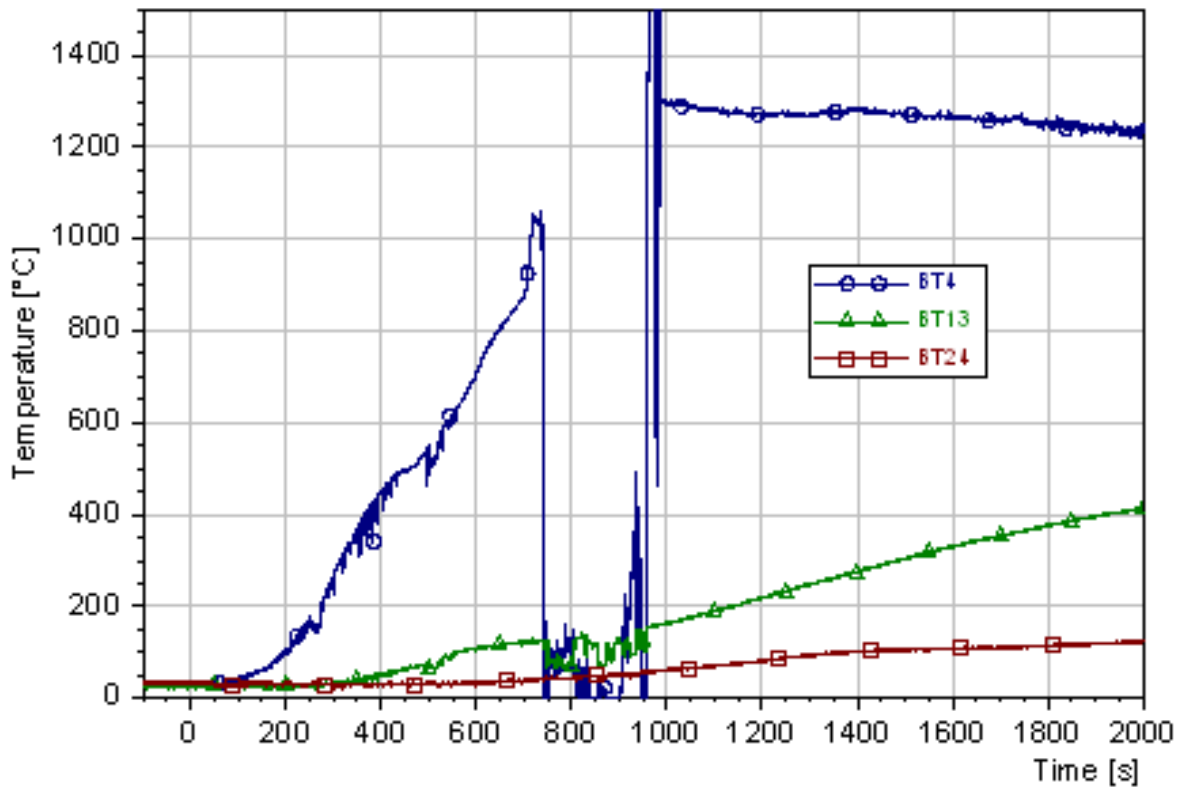In addition, the plot of the constant argon cover gas flow is also added.
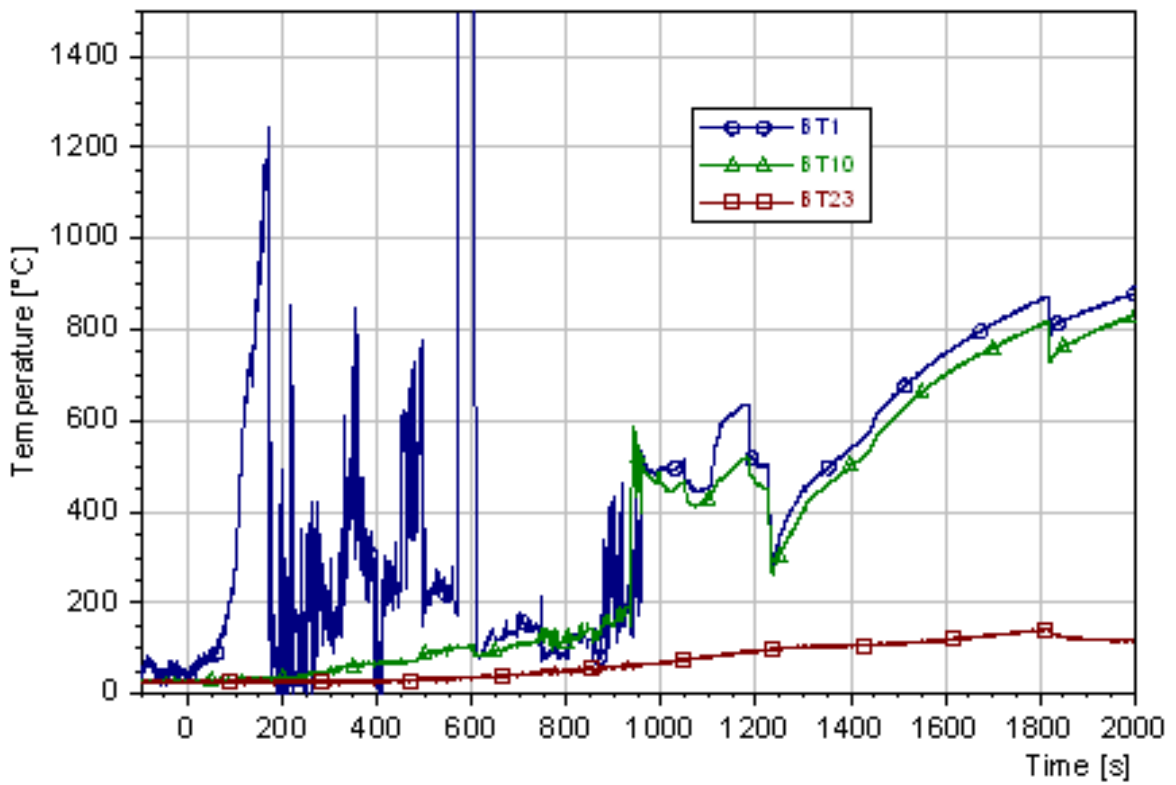
Figure C1: Thermocouples on the centre line (BT 1, BT 10, and BT 23)
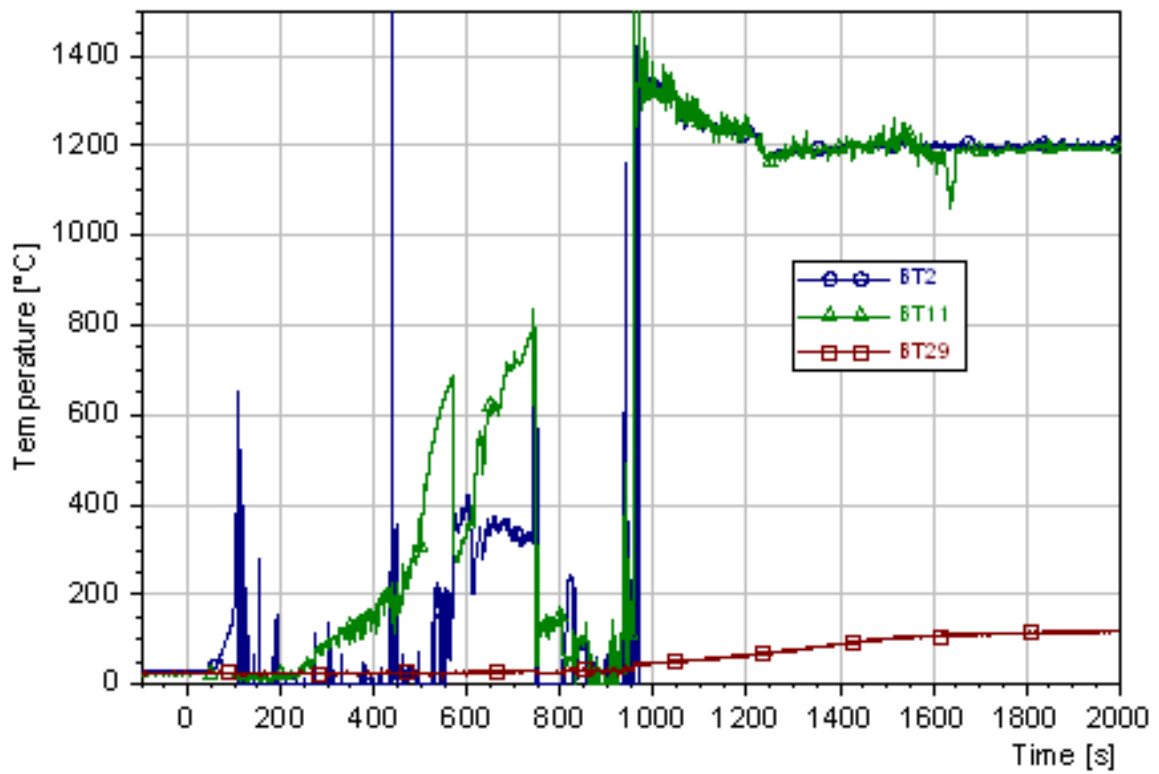
Figure C2: Thermocouples on t 2 line (BT 2, BT 11, and BT 29)
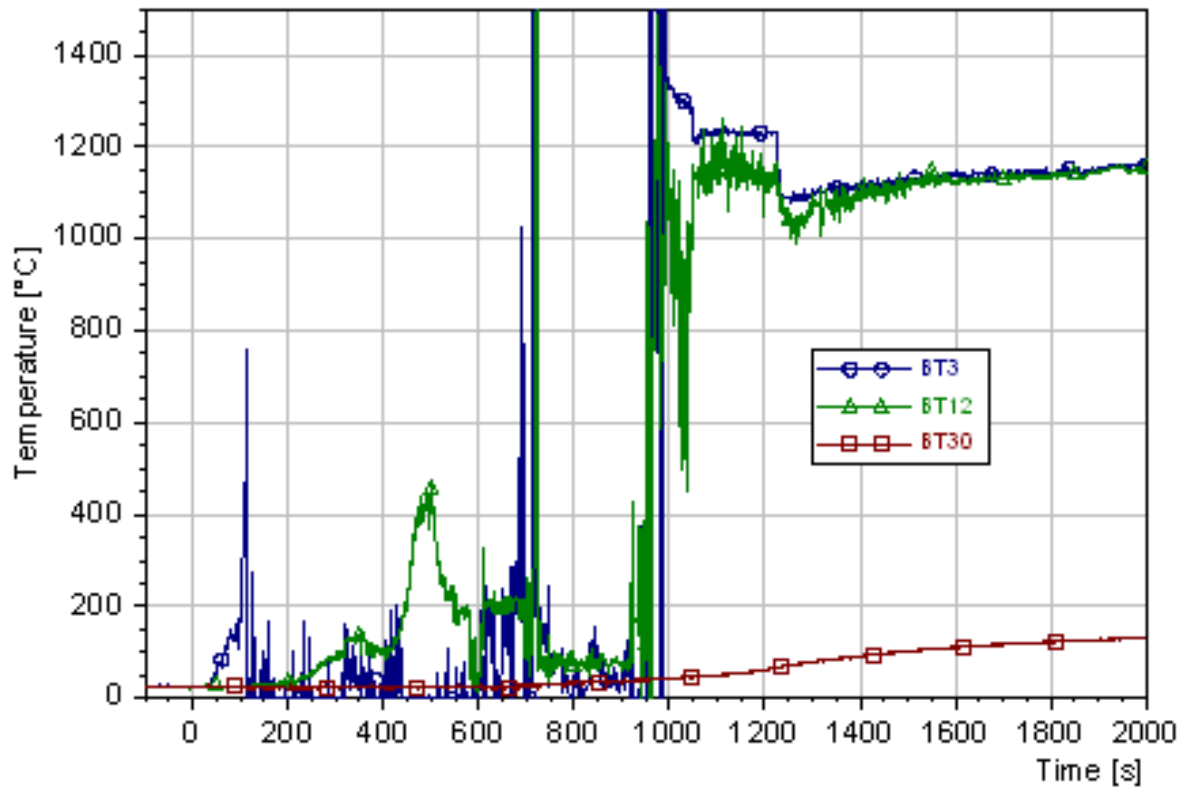
Figure C3: Thermocouples on "-"t 2 line (BT 3, BT 12, and BT 30)



Figure C4: Thermocouples on t 3 line (BT 4, BT 13, and BT 24)
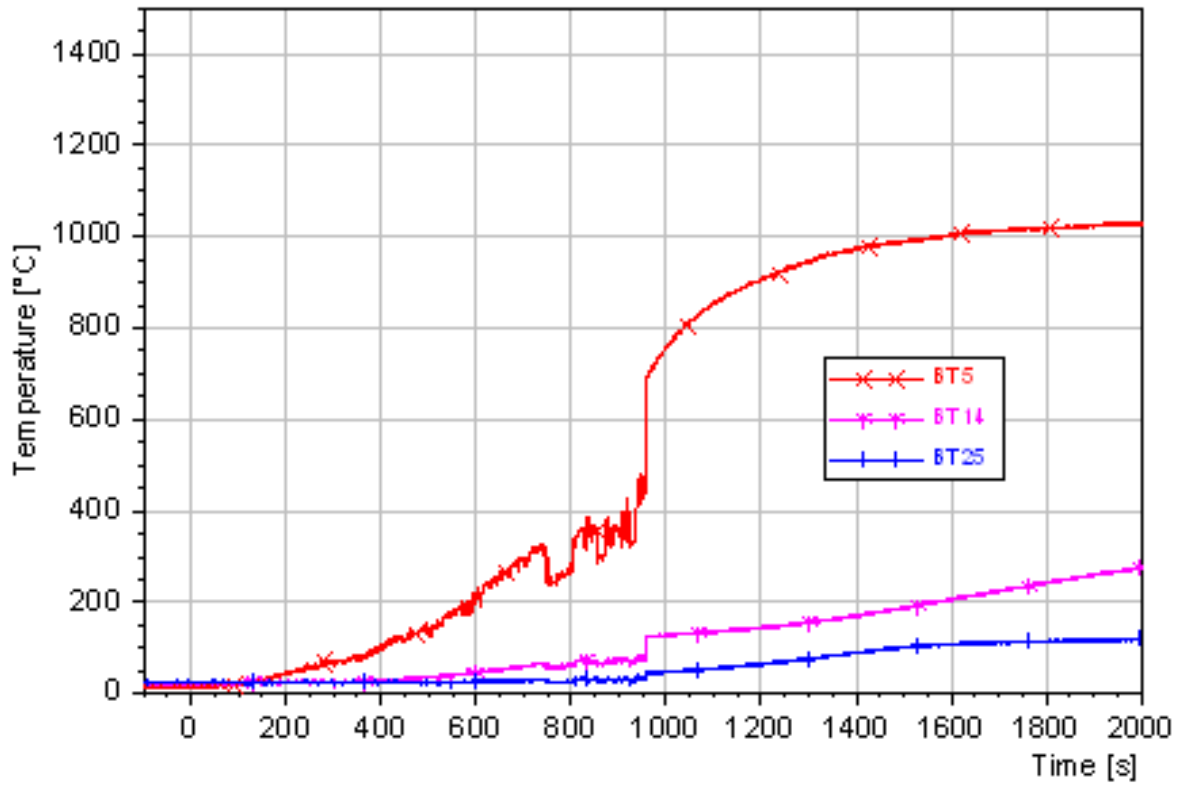
Figure C5: Thermocouples on "-"t 3 line (BT 5, BT 14, and BT 25)
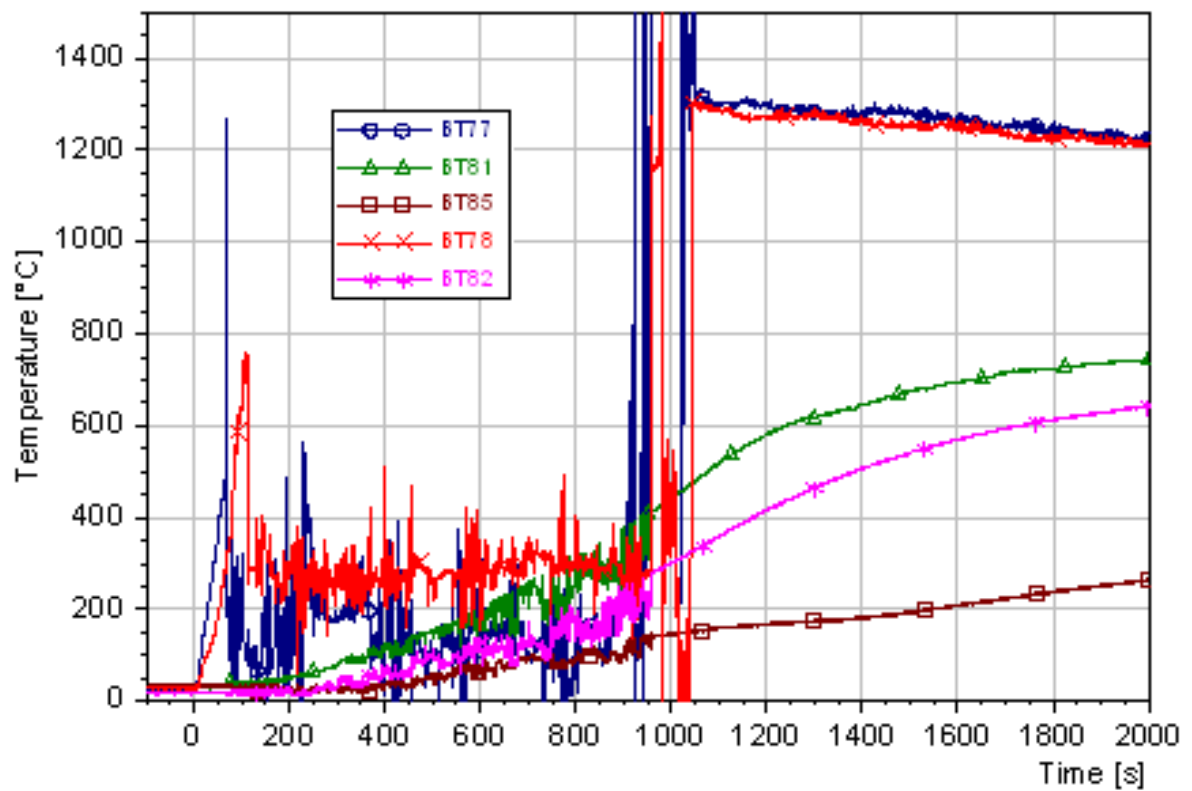
Figure C6: Thermocouples on t 4 line from SW – NE and SE – NW planes (BT 77, BT 81, BT 85, BT 78, and BT 82)
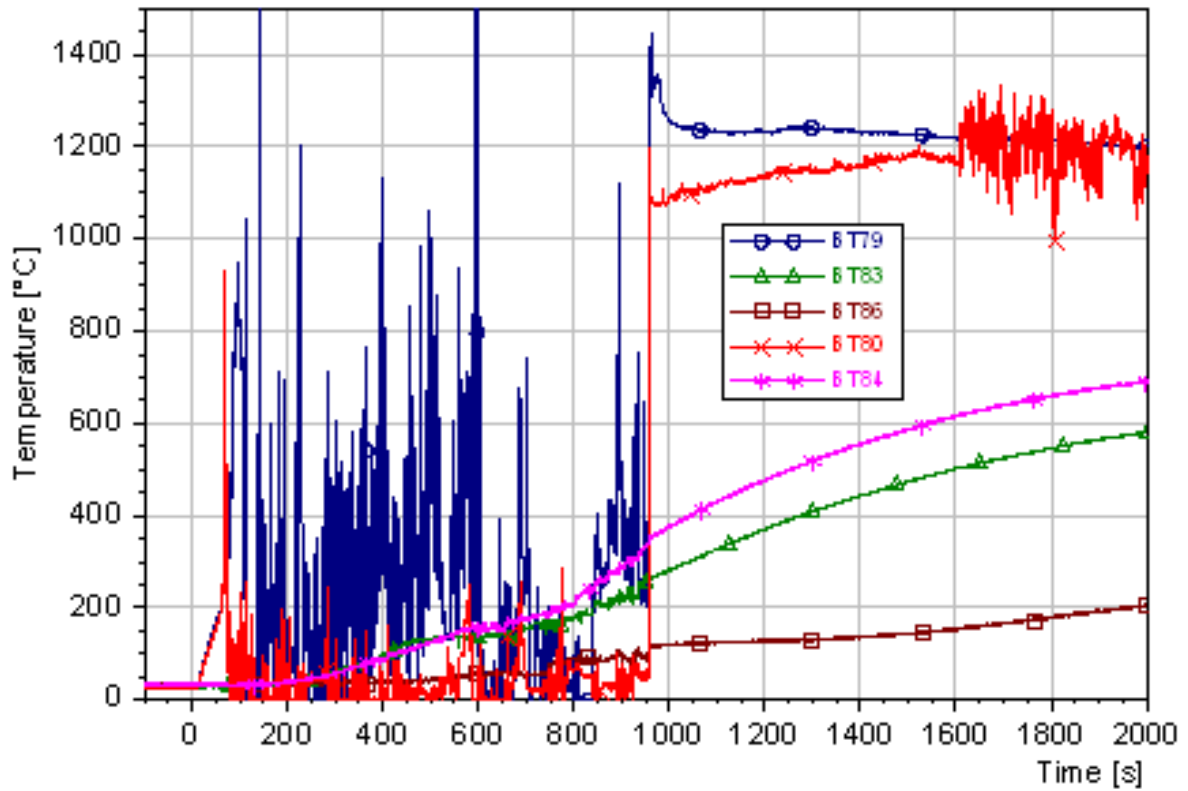
Figure C7: Thermocouples on "-"t 4 line from SW – NE and SE – NW planes (BT 79, BT 83, BT 86, BT 80, and BT 84)
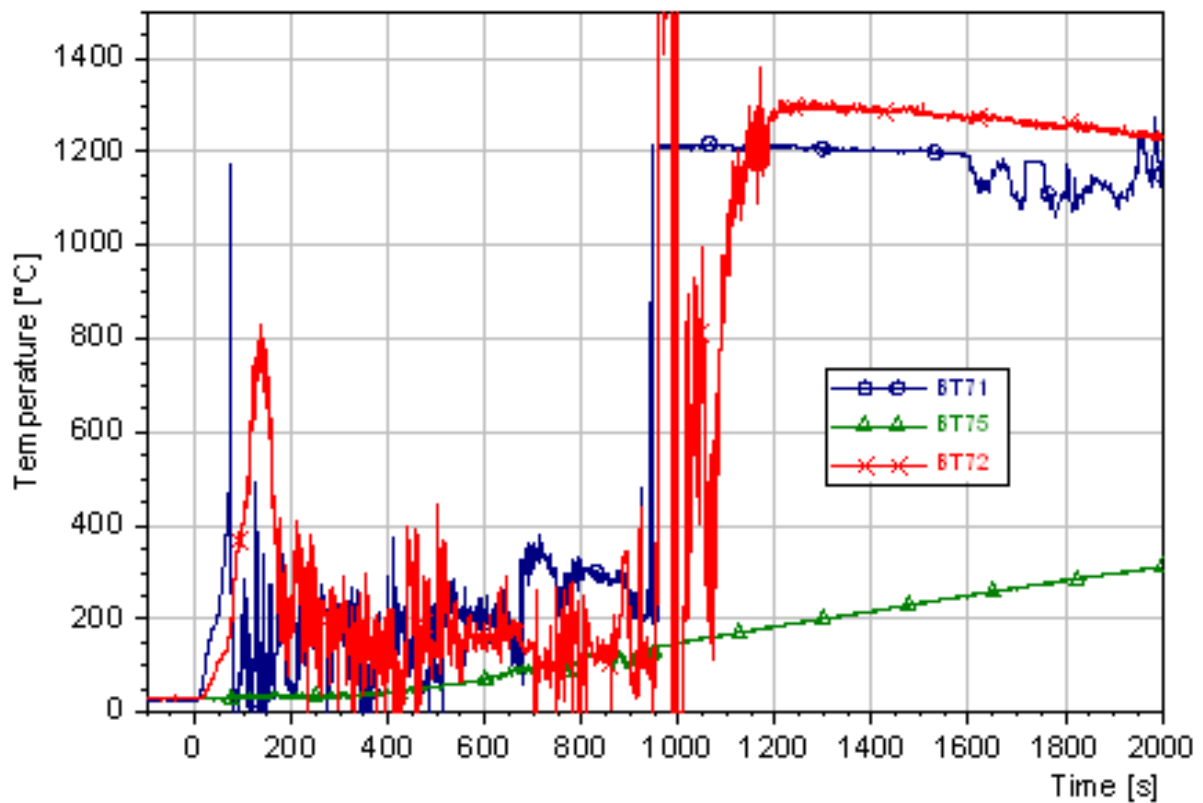
Figure C8: Thermocouples on t 5 line (BT 71, BT 75, and BT 72)
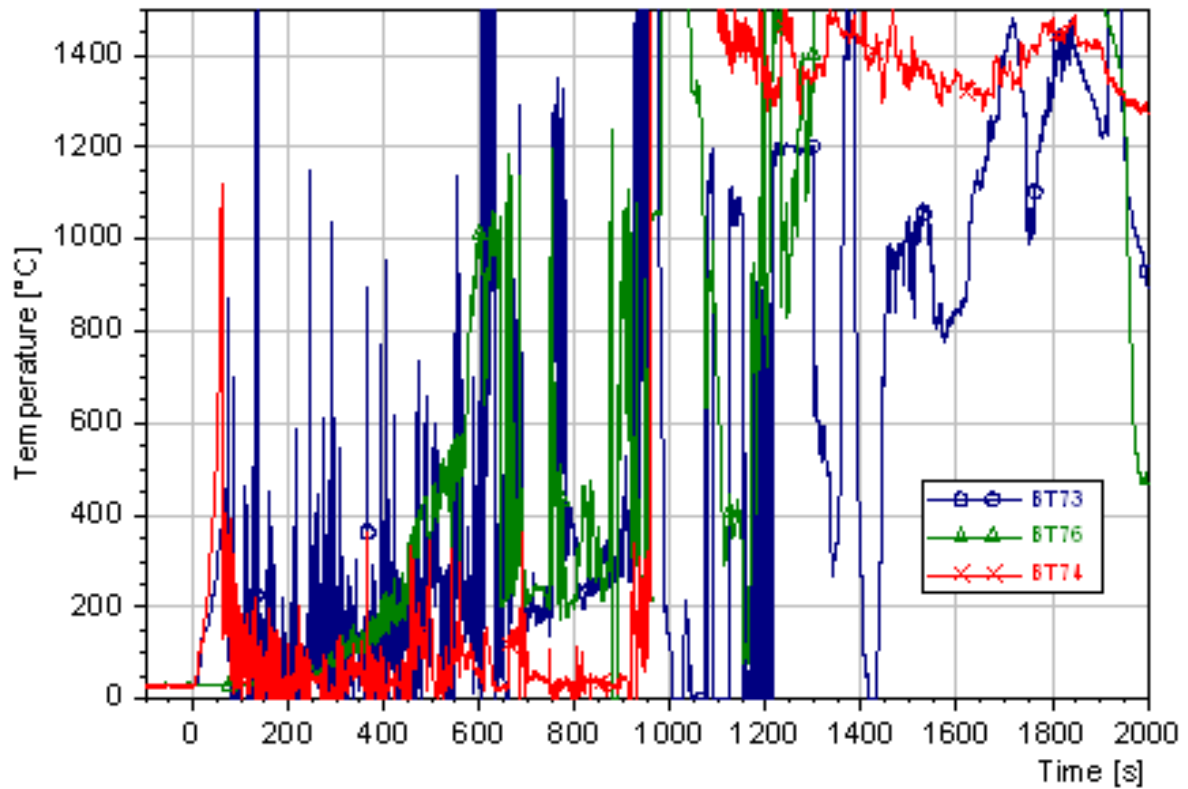
Figure C9: Thermocouples on "-"t 5 line (BT 73, BT 76, and BT 7
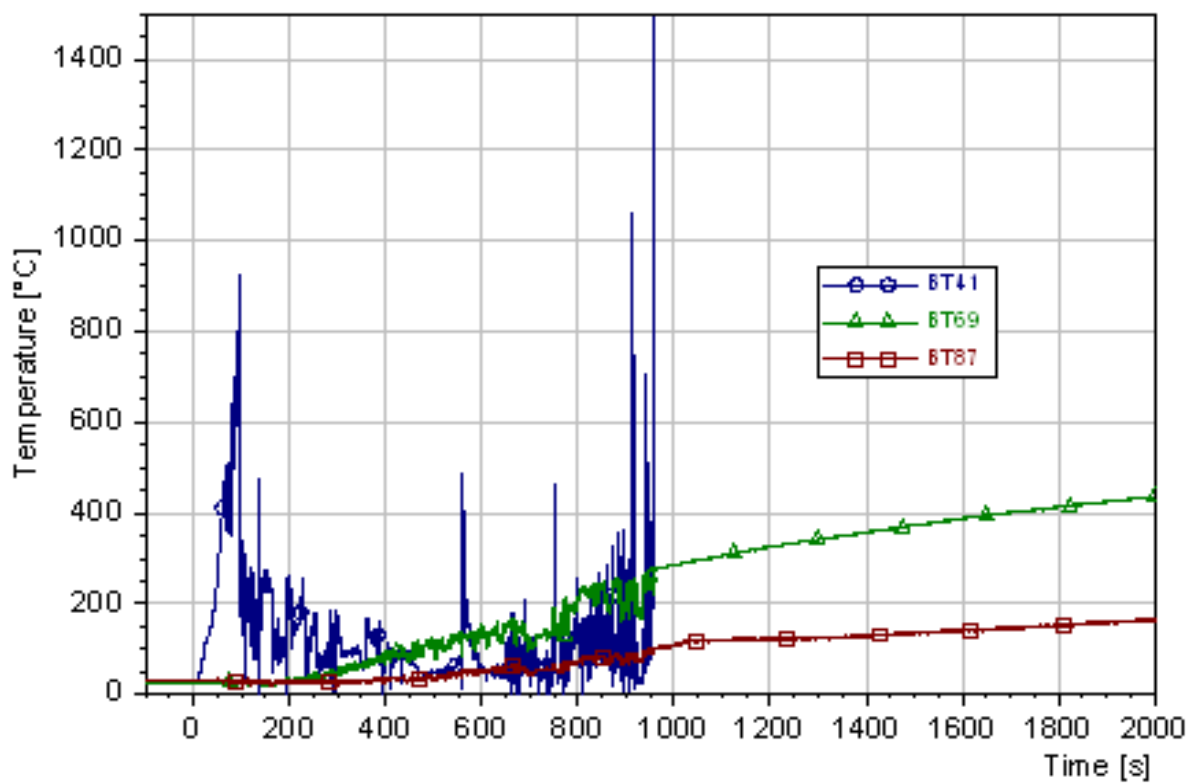
Figure C10: Thermocouples on t 6 line (BT 41, BT 69, and BT 87)
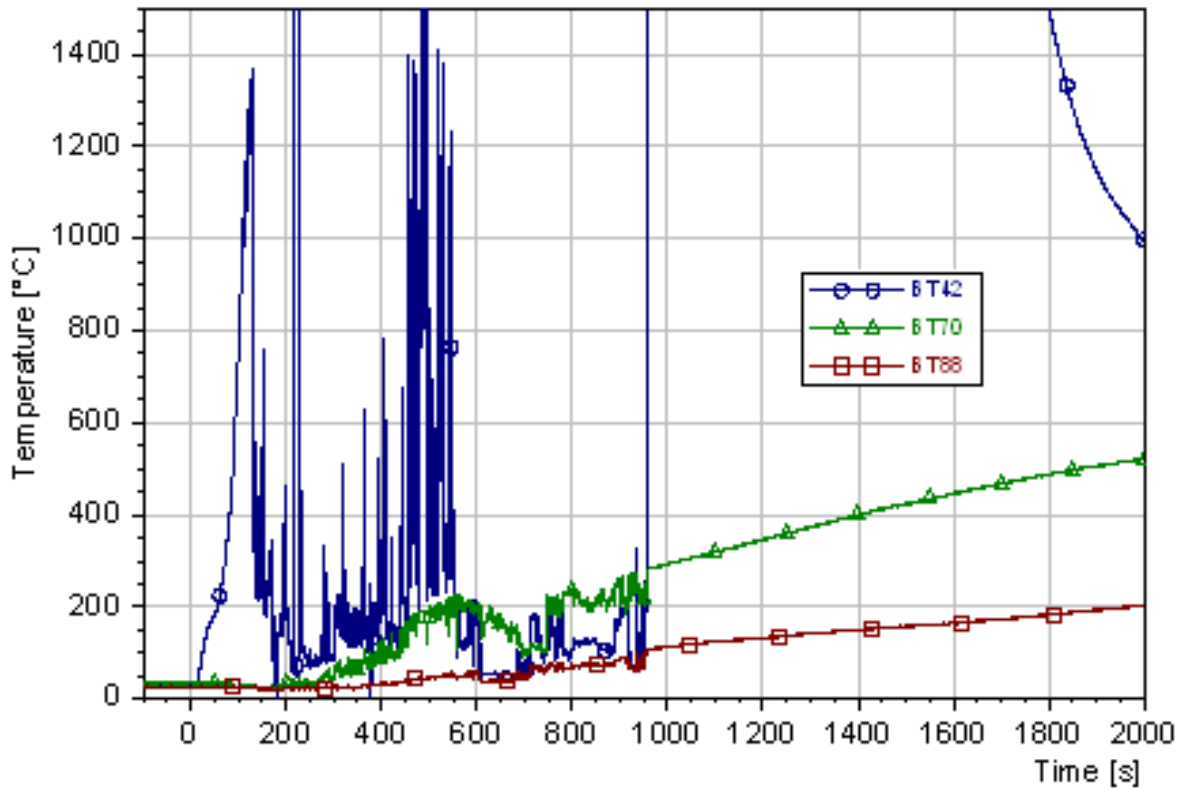
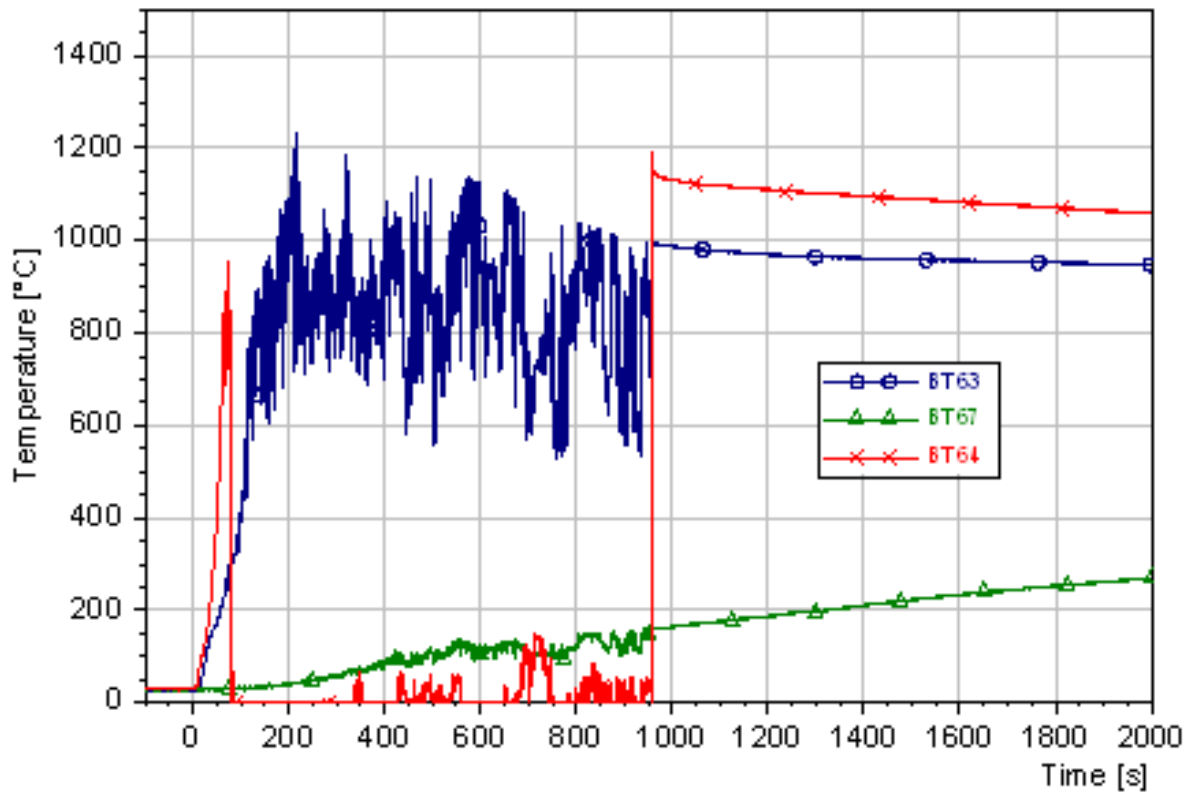Figure C11: Thermocouples on "-"t 6 line (BT 42, BT 70, and BT 88)

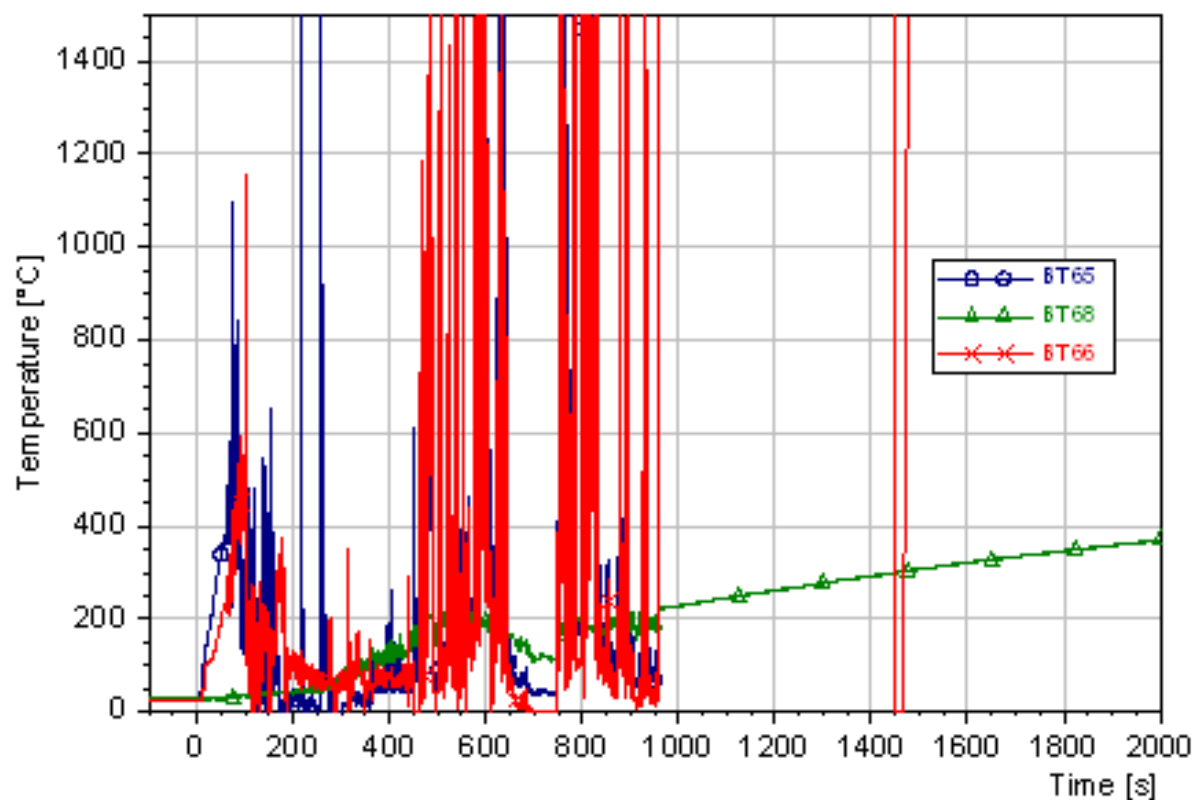Figure C12: Thermocouples on t 7 line (BT 63, BT 67, and BT 64)
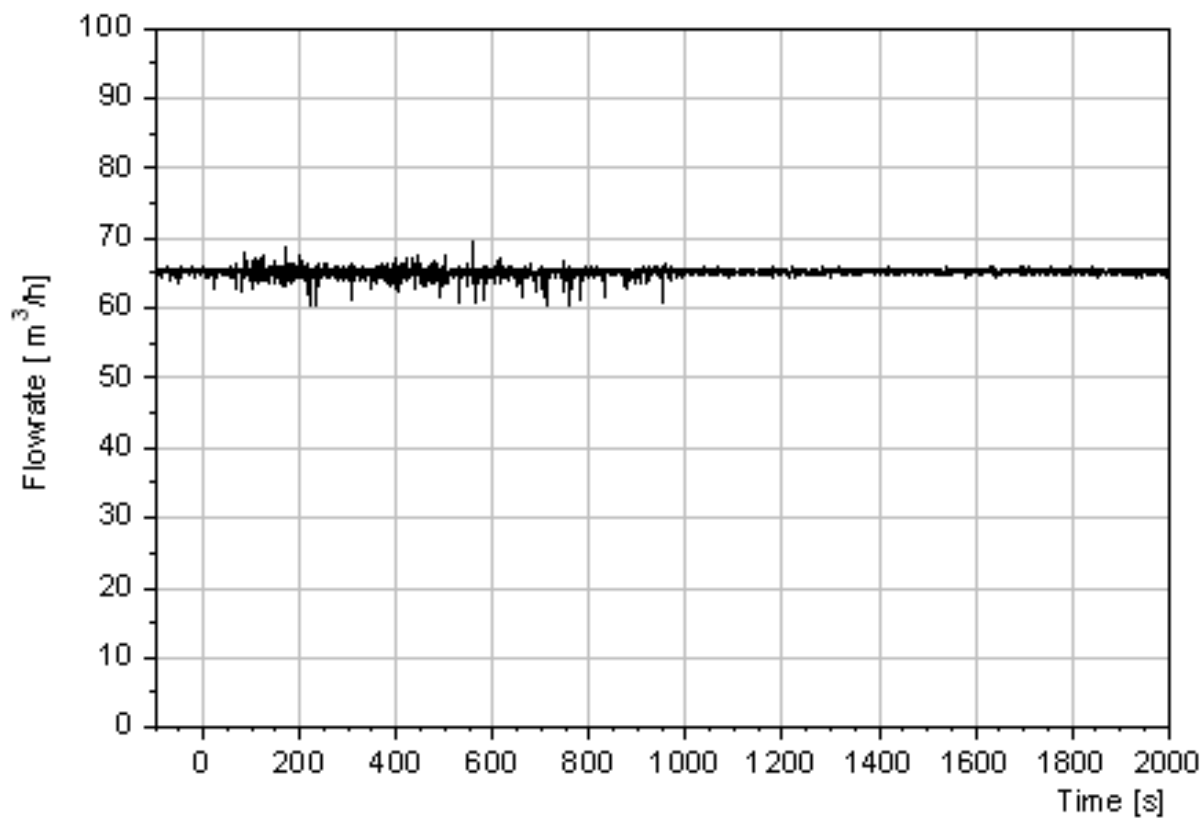
Figure C13: Thermocouples on "-"t 7 line (BT 65, BT 68, and BT 66)

Figure C14: Argon flow in the off-gas tube